TAMPERE UNIVERSITY OF TECHNOLOGY

Aku Antikainen

HIGHER-ORDER CORRELATIONS OF SUPERCONTINUUM LIGHT

Master of Science Thesis

Examiners: Prof. Goëry Genty and Prof. Matti Vilkko
Examiners and topic approved in the Engineering Sciences Faculty Council meeting on 3.4.2013

TIIVISTELMÄ

TAMPEREEN TEKNILLINEN YLIOPISTO
Automaatiotekniikan koulutusohjelma
Aku Antikainen: Superkontinuumivalon korkeamman asteen korrelaatiot
Diplomityö, 77 sivua
Elokuu 2013
Pääaine: Systeemiteoria
Tarkastajat: Prof. Goëry Genty ja Prof. Matti Vilkko
Avainsanat: superkontinuumi, korrelaatio, koherenssi

Työssä tutkitaan superkontinuumivalon intensiteettikorrelaatioita ja koherenssiominaisuuksia aika- ja taajuustasoissa simuloimalla laserpulssien etenemistä ratkaisemalla yleistettyä epälineaarista Schrödinger-yhtälöä numeerisesti eri alkuehdoilla. Pulsseille käytetään eri huipputehoja ja kestoja korrelaatioiden ja koherenssin kartoittamiseksi erilaisilla superkontinuumin dynaamisilla alueilla. Jokaiselle parametrijoukolle luodaan tuhat simulaatiota vaihtelevalla satunnaisella alkukohinalla, jotta tulokset ja johtopäätökset ovat luotettavia. Painopiste on korrelaatioiden ja koherenssin tulkitsemisessa tunnettujen epälineaaristen optisten ilmiöiden ja superkontinuumin sähkökenttäkoherenssia käsittelevien aikaisempien tutkimusten avulla.

Intensiteettikorrelaatioita tutkitaan laskemalla ja analysoimalla korrelaatiokertoimia. Työssä määriteltävän ristitasokorrelaatiofunktion avulla tutkitaan korrelaatioita spektrin ja aikatason ominaisuuksien välillä. Sekä sähkökenttien että intensiteettien koherenssiominaisuuksiin perehdytään käyttäen aika- ja taajuuskoherenssifunktioita. Funktioiden rakenteet ja säännönmukaisuudet selitetään yksityiskohtaisesti epälineaaristen optisten prosessien avulla. Koherenssi- ja korrelaatio-ominaisuuksiin vaikuttavat optiset ilmiöt tunnistetaan ja osoitetaan erilaisiksi riippuen pulssin kestosta. Lyhyiden pulssien spektrin levenemiseen vaikuttavien mekanismien osoitetaan tuottavan koherentimpia superkontinuumeja kuin pitkien pulssien tapauksessa dominoivien ilmiöiden. Koherenttien ja epäkoherenttien superkontinuumien sovelluskohteet mainitaan lyhyesti oleellisten lähdeviitteiden kera. Tässä työssä esitetyt tulokset luovat pohjan myöhemmille tutkimuksille koskien superkontinuumivalon intensiteettikorrelaatio- ja korkeamman asteen koherenssiominaisuuksia. Viimeisessä luvussa esitetään mahdollisia jatkotutkimuskohteita, joihin syventymällä päästään yhä lähemmäksi lopullista tavoitetta, joka on superkontinuumien ominaisuuksien täydellinen räätälöiminen.

ABSTRACT

TAMPERE UNIVERSITY OF TECHNOLOGY
Master's Degree Programme in Automation Technology
Aku Antikainen: Higher-Order Correlations of Supercontinuum Light
Master of Science Thesis, 77 pages
August 2013
Major: Systems theory
Examiners: Prof. Goëry Genty and Prof. Matti Vilkko
Keywords: supercontinuum, correlation, coherence

Intensity correlations and coherence properties of supercontinuum light are studied in spectral and temporal domains by simulating laser pulse propagation in optical fibers by numerically solving the generalized nonlinear Schrödinger equation for various initial conditions. Different input peak powers and pulse durations are used in order to explore correlations and coherence in various regimes of supercontinuum dynamics. An ensemble of a thousand simulations with varying random input noise is generated for each set of input parameters to ensure reliability of the results and conclusions. An emphasis is laid on the interpretation of the correlations and coherence properties in terms of well known nonlinear optical effects and previous research regarding electric field coherence of supercontinua.

The intensity correlations are studied by calculating and analyzing the correlation coefficients. A cross-domain correlation function is introduced to examine correlations between temporal and spectral features. Coherence properties are explored and discussed with the help of mutual coherence functions and cross-spectral densities for both electric fields and intensities. Detailed explanations for the structure and patterns of the correlation and coherence functions are given in terms of nonlinear optical processes. The optical phenomena responsible for the observed correlations and coherence properties are identified and shown to be different depending on input pulse duration. Certain mechanisms responsible for the spectral broadening of short pulses are shown to lead to more coherent supercontinua than other phenomena that characterize supercontinuum generation in the long-pulse regime. Applications of both coherent and incoherent supercontinua are briefly mentioned with relevant citations. The results presented here lay the cornerstone for future work in intensity correlations and higher-order coherence of supercontinua. With the ultimate goal of complete control over supercontinuum properties in mind, possibilities for future research are presented in the concluding chapter.

PREFACE

This thesis was done in Tampere University of Technology for the Department of Automation Science and Engineering in the Optics Laboratory of the Department of Physics during 2013 with simulation data from 2012 and 2013. Many thanks to Professor Goëry Genty for his priceless help in analyzing the results, for the vast amount of comments and corrections regarding the contents of this thesis and for being an awesome group leader, teacher, and a role model both inside and outside the laboratory. I would like to thank Professor Matti Vilkko for his comments on the structure of the thesis and for being a great teacher.

The Matlab code, a modified version of which was used for the simulations, can be traced to Professor John M. Dudley, and I thank him for that. I would also like to thank Professor Martti Kauranen, PhD Mikko Huttunen, and MSc Mariusz Zdanowicz for teaching me basic optics. MSc Antti Aalto, MSc Johan Sand, BSc Mikko Närhi and BSc Jussi Rossi deserve thanks for helpful discussions and for being great company. I would also like to thank Leena Litma and my family members Hannele, Seppo, and Atte for helping me arrange time to write this thesis.

Aku Antikainen,
Tampere, 30.7.2013

CONTENTS

LANGUAGE, ABBREVIATIONS, AND SYMBOLS

The language of the thesis is American English, which means that the short scale naming convention is used for numbers: a billion has nine zeros and a trillion has twelve. The decimal mark used in this thesis is the dot or full stop, which is common in science and engineering: $3/2 = 1.5$.

Abbreviations

au	Arbitrary units
CSD	Cross-spectral density
CW	Continuous-wave
DC	Direct Current
DFWM	Degenerate four-wave mixing
DPSSFD	Diode pumped solid state frequency doubled
DW	Dispersive wave
FFT	Fast Fourier transform
FWM	Four-wave mixing
GNLSE	Generalized nonlinear Schrödinger equation
GVD	group-velocity dispersion
MCF	Mutual coherence function
MI	Modulation instability
NLSE	Nonlinear Schrödinger equation
PCF	Photonic crystal fiber
RMS	Root mean square
SC	Supercontinuum
SSFM	Split-step Fourier method
SSFS	Soliton self-frequency shift
SPM	Self-phase modulation
SRS	Stimulated Raman-scattering
THG	Third-harmonic generation
TOD	Third-order dispersion
WDM	Wavelength-division multiplexing
XPM	Cross-phase modulation
ZDW	Zero-dispersion wavelength

Symbols

$\mathbb{R}$	The set of real numbers
$\mathbf{B}$	Magnetic flux density
$\mathbf{D}$	Electric displacement
$\mathbf{E}$	Electric field strength
$\mathbf{H}$	Magnetic field strength
$\mathbf{J}_{\mathrm{f}}$	Free current density
$\mathbf{M}$	Magnetization
$\mathbf{P}$	Polarization
$\mathbf{P}_{\mathrm{L}}$	Linear polarization
$\mathbf{P}_{\mathrm{NL}}$	Nonlinear polarization
A	Amplitude
A_{eff}	Effective mode area
F	Transverse modal distribution
L_{c}	Coherence length
N	Soliton order
P_0	Peak power
R	Response function
T	Retarded time coordinate
V	Normalized frequency (also called the V-parameter)
$W_{\mathrm{E}}(f_1, f_2)$	Cross-spectral density for electric fields
$W_{\mathrm{I}}(f_1, f_2)$	Cross-spectral density for intensities
c	Vacuum speed of light
f	Frequency
g	Gain
h	step size in the SSFM
h_{P}	Planck's constant
h_{R}	Raman response function
$\hbar$	Reduced Planck's constant, $\hbar = h/(2\pi)$
k	Wave number
k_0	Vacuum wave number
l_{c}	Correlation length
n	Refractive index
n_1	Fiber core refractive index, linear refractive index
n_2	Fiber cladding refractive index, nonlinear refractive index
n_{eff}	Effective refractive index
$\bar{n}$	Modal index
v_{g}	Group velocity

Symbols (continued)

$\Gamma_{\mathrm{E}}(t_1, t_2)$	Mutual coherence function for electric fields
$\Gamma_{\mathrm{I}}(t_1, t_2)$	Mutual coherence function for intensities
Γ_{R}	Raman noise term
Ω	Angular frequency separation
α	Loss parameter
β	Propagation constant
β_n	Dispersion coefficient of order n
γ	Nonlinear coefficient
$\gamma_{\mathrm{E}}(t_1, t_2)$	normalized mutual coherence function for electric fields
$\gamma_{\mathrm{I}}(t_1, t_2)$	normalized mutual coherence function for intensities
ε	Permittivity
ε_0	Vacuum permittivity
θ	Propagation angle
λ	Wavelength
λ_0	Vacuum wavelength
μ	Permeability
μ_0	Vacuum permeability
$\mu_{\mathrm{E}}(f_1, f_2)$	Normalized cross-spectral density for electric fields
$\mu_{\mathrm{I}}(f_1, f_2)$	Normalized cross-spectral density for intensities
ρ	Radial distance in cylindrical coordinates
$\rho_{\mathrm{c}}(t, f)$	Cross-domain correlation function
$\rho_{\mathrm{t}}(t_1, t_2)$	Temporal correlation function
$\rho_{\mathrm{f}}(f_1, f_2)$	Spectral correlation function
ρ_{free}	Free charge density
τ_{shock}	Shock time scale
χ	Electric susceptibility
$\chi^{(1)}$	Linear susceptibility
$\chi^{(n)}$	Susceptibility of order n
χ_{m}	Magnetic susceptibility
ω	Angular frequency (also referred to as "frequency")
ω_0	Central (angular) frequency

The meaning of other symbols used is indicated in the context or has become standard notation. Vector quantities are bolded. When vector quantities are treated as scalars, a similar unbolded symbol is used. Components of vectors are denoted by using subscripts.

Transforms and Operators

$\tilde{\mathbf{E}}$	The Fourier-transform of $\mathbf{E}$. Note that in optics the Fourier transform is defined as $\tilde{f}(\omega) = \int_{-\infty}^{\infty} f(t) \exp(i\omega t) dt$.
$\hat{D}$	Dispersion operator
$\hat{N}$	Nonlinear operator
∇	Gradient
$\nabla\cdot$	Divergence
$\nabla\times$	Curl
∇^2	Vector Laplacian
$\Re(z)$	The real part of z
$\Im(z)$	The imaginary part of z
$\lvert z\rvert$	The absolute value of z
$\arg(z)$	The argument or phase angle of z
$\sum_j$	Sum over possible values of j

Special Functions

J_n	The Bessel function of order n
K_n	The modified Bessel function of order n
δ	The Dirac delta function

Derivatives and Integrals

$\dfrac{df}{dx}$	The derivative of f with respect to x.
$\dfrac{\partial f}{\partial x}$	The partial derivative of f with respect to x
$\int_a^b f(x)dx$	The definite integral of the function $f(x)$ from a to b. Similarly indefinite and improper integrals.

Derivatives of functions of one variable can also be denoted by the prime symbol ($'$).

1. INTRODUCTION

Linear optical systems are analogous to linear systems in control theory in the sense that only the phase and amplitude of a sinusoidal input can be affected by the system [1, 2]. The color of the light entering a linear system remains the same. In nonlinear systems the frequency of the output is in general different from the frequency of the input, which in optics means generation of light at new frequencies. The system dynamics are no longer independent of the amplitude of the input.

Even though linear systems are neat because of their mathematical simplicity, they are very restrictive. Nonlinear phenomena pave the way for richer system dynamics and in optics open the door for numerous applications ranging from green laser pointers to transoceanic soliton communication systems [3, 4]. One of the extreme manifestations of many nonlinear optical processes acting together is the *supercontinuum* (SC), a light source like no other.

Supercontinuum is the name given to the process of significant spectral broadening in a nonlinear optical system. The discovery of supercontinuum is credited to Alfano and Shapiro, who observed remarkable spectral broadening in bulk glass and explained their findings in terms of nonlinear optical processes in 1970 [5, 6]. It is noteworthy that Alfano and Shapiro neither focused on the spectral broadening in their studies nor coined the term supercontinuum. Similar extreme spectral broadening was also observed in rare atomic gases by the same group [7] and later in silica fibers by Lin and Stolen [8]. Since then, supercontinuum generation in optical fibers attracted the most attention in the field.

Although the emergence of a broad SC spectrum is scientifically astonishing, it is not uncommon for light sources to emit electromagnetic radiation at a vast frequency range. Even the star at the heart of our Solar System provides broadband radiation, so the broad SC spectrum is literally nothing new under the Sun. However, no other broadband light source besides SC is capable of such beams of high brightness, spectral stability, and most importantly spatial and temporal coherence.

Supercontinuum is a fascinating phenomenon from the point of view of fundamental

research, but because of its unique characteristics it also has a tremendous amount of applications. One of the first applications of supercontinuum was absorption and excitation spectroscopy, which was in turn used to study picosecond and femtosecond processes in biology, chemistry, and solid-state physics [9]. Notable examples of the processes that were studied are given by photosynthesis, dynamical steps of chemical reactions, and optical phonons, respectively. Supercontinuum can also be used in optical communications in pulse compression and *wavelength-division multiplexing* (WDM) [10, 11].

1996 saw the advent of *photonic crystal fiber* (PCF) that revolutionized supercontinuum generation because they offered the possibility to tune important fiber parameters [12]. The first report on SC generation in PCF was given by Ranka et. al [13] and since then SC generation in PCF has been studied extensively. The introduction of the PCF allowed for even more applications, and supercontinuum has subsequently found applications in high-precision frequency metrology [14] and ultrahigh-resolution optical coherence tomography [15], for example.

The effects of *self-phase modulation* (SPM), *four-wave mixing* (FWM) and *Stimulated Raman scattering* (SRS) were well understood at the end of the 1970's [16, 17, 18, 19, 20, 21, 22] and it was realized that the broad and flat continuum could not be explained by these phenomena alone [23]. Although solitons had been predicted in 1973 [24] and observed experimentally in 1980 [25], no satisfactory explanation for the spectral broadening was offered until the experimental observation of the *soliton self-frequency shift* (SSFS) in 1985 [26]. By 1992 the dynamics of supercontinuum generation were understood to such an extent that an accurate mathematical model could be developed and numerical simulations be used to study supercontinuum generation [27].

By 2006, a very accurate numerical model known as the Generalized Nonlinear Schrödinger Equation or GNLSE had been developed and tested thoroughly [28]. The model is highly nonlinear and the solutions can depend heavily on input noise. This noise-dependence affects the coherence properties of the resulting supercontinuum, and coherence is one of the most important characteristic that makes SC different from other white-light sources. Characterization of the coherence properties is therefore of utmost importance, and many studies on supercontinuum coherence have been conducted both experimentally and numerically [29, 30, 31, 32]. In a recent stduy [33] Genty et al. characterized the coherence properties of supercontinua by explaining the form of the correlation function in terms of a quasi-stationary part and a quasi-coherent part. Furthermore, Korhonen et al. derived an elementary field

representation for the second-order coherence functions of supercontinuum in 2012 [34].

The recent ongoing research regarding the coherence properties of supercontinuum indicates that there is a continuing need for thorough characterization of them and that our current understanding, although increasingly vast, is still incomplete. Moreover, the studies conducted so far have almost entirely focused on electric field correlations, and a logical next step is to move towards exploring higher-order correlation properties of supercontinua. In other words, there is a thesis-wide gap in our knowledge.

The aim of this study is two-fold. First, to study the intensity correlations and coherence properties of supercontinua, and second, to explain what features of the correlation and coherence patterns are due to which nonlinear phenomena. The vast existing knowledge on the phenomena can then be deployed for the benefit of generation of customizable supercontinua for different applications such as optical coherence tomography or white-light interferometry. The intensity correlations and coherence properties are studied by varying the input parameters such as pulse duration and peak power and generating ensembles of supercontinua with different initial noise conditions for each set of input parameters. The ensembles are generated by numerically solving the nonlinear propagation equation.

2. THE NATURE OF LIGHT

Based on an idea that dates back to at least the ancient Greeks, Sir Isaac Newton eventually considered light to consist of small discrete particles he called *corpuscles* [35]. According to Newton, corpuscles traveled in straight lines with a finite velocity and corpuscles representing different colors of light had different sizes. Newton was, however, aware of the diffraction phenomenon, which had been studied and named by the Italian priest Francesco Maria Grimaldi in 1665, and in his earlier days he avoided speculations and stayed ambivalent about the nature of light. Since light passing through an aperture forms a cone, the propagation of light could not be satisfactorily explained with the corpuscular theory alone, which led Newton to incorporate elements from the wave treatment of light by concluding that light corpuscles excited vibrations in an imaginary matter, *aether* [2]. Being unable to explain the observed rectilinear propagation of light using wave theory only, Newton became a supporter of the corpuscular theory in his later days.

Because of Newton's prestige, the corpuscular theory superseded the previous idea put forward by René Descartes [36], Robert Hooke [37], and Christiaan Huygens [38], all of whom explained light via pressure or vibrations in aether without resorting to speculations about corpuscles. Although Huygens had succeeded in, for example, describing the birefringence property of an Icelandic calcite crystal using the wave treatment of light, it wasn't until the beginning 19th century that the mechanical corpuscle treatment of light was fully abandoned.

The experiment that seemed to settle the matter about the wave nature of light was Young's double slit experiment in 1801 [39]. The interference pattern observed in Young's experiment can only be explained if light is understood to be wavelike. The simplicity of the experiment and the impact of the results makes one wonder why the experiment was not conducted earlier in order to find out whether light had wavelike properties. One of the reasons why the physics community had to wait until the 19th century is that the experiment requires coherent light. Incoherent sunlight can easily be made spatially coherent by letting it pass through a small aperture, as was the case in the original experiment [2], but without knowing the requirement of coherence a priori, the necessity of the pinhole is far from obvious.

Around 1814 Augustin Jean Fresnel began a revival of the wave theory in France, unaware of Young's work and experiments. Fresnel incorporated Huygens' wave despcription and the interference principle to calculate various diffraction patterns arising from obstacles and apertures. Fresnel was also able to explain, using wave formalism, the rectilinear propagation of light - an easily observed phenomenon that had been one of the main reasons Newton had become an adherent of the corpuscular theory. [2]

Huygens had discovered polarization during his research on optical properties of calcite crystals. At first polarization was thought to be inherent to crystalline media, but more than a century later Étienne Louis Malus discovered that polarization was also present upon reflection of light. This led Fresnel and Dominique François Arago to conduct experiments to study the effects of polarization on interference, but they were unable to explain their results. This was because at that time light waves were thought to be longitudal like sound waves[1]. The interference observed in Young's experiment bore, after all, remarkable similarity to beats that are heard when two sound waves of slightly different frequencies interfere. Several years later Young was able to explain the results by suggesting that the aethereal vibrations might be transverse with polarization being a manifestation of the direction of the vibrations. [2]

Although the first known terrestrial measurements regarding the speed of light were performed by Armand Hippolyte Louis Fizeau in 1849 [2], the question about the finiteness of the speed of light had been answered almost two centuries earlier. In the 17th century the Dane Ole Christensen Römer observed the motion of Jupiter's nearest moon, Io, and in 1676 correctly concluded that in order to explain his observations, the speed of light must be finite. Based on Römer's observations, Huygens and Newton individually estimated the diameter of Earth's orbit and calculated the speed of light to be $2.3 \cdot 10^8$ m/s and $2.4 \cdot 10^8$ m/s, respectively [40]. Fizeau's measurements yielded the value $3.153 \cdot 10^8$ m/s for the speed of light. Although the results differed a bit, the order of magnitude was the same astronomical 10^8 m/s in all of them. The speed of light could just as well have been infinite, and the finiteness of it was not necessarily important until the discoveries and predictions of the Scottish physicist James Clerk Maxwell.

One of the first scientists to bring optics, circuit analysis and studies of electricity

[1]Sound waves were known to be longitudal. This becomes quite obvious when one considers, for instance, a vibrating drum membrane and the air displacement the vibration causes.

and magnetism together was Michael Faraday. Faraday noticed that the polarization of a light beam could be altered by a strong magnetic field applied to the medium in which the beam propagated [2]. By collecting the known results on electricity and magnetism and deriving some of his own, James Clerk Maxwell arrived in a set of four equations that today bear his name. Using these relations he derived two equations: one for the electric field strength and one for the magnetic flux density. Both of the equations had the exact same structure of a wave equation. Maxwell proceeded to predict the existence of electromagnetic waves, the velocity of which agreed with the velocity of light measured by Fizeau. The agreement between the velocities encouraged Maxwell to conclude that *light is electromagnetic radiation.*

2.1 Maxwell's Equations

In the nineteenth century Maxwell collected and published a set of universal[2] equations based on electromagnetic theory and circuit analysis. These equations can be expressed using four vector equations:

$$\nabla \cdot \mathbf{D} = \rho_{\text{free}}, \tag{2.1}$$

$$\nabla \cdot \mathbf{B} = 0, \tag{2.2}$$

$$\nabla \times \mathbf{E} = -\frac{\partial \mathbf{B}}{\partial t}, \tag{2.3}$$

$$\nabla \times \mathbf{H} = \mathbf{J}_{\text{f}} + \frac{\partial \mathbf{D}}{\partial t}, \tag{2.4}$$

where $\mathbf{E}$ and $\mathbf{H}$ are the electric and magnetic field strengths, respectively, and $\mathbf{D}$ and $\mathbf{B}$ are the corresponding electric and magnetic flux densities, ρ_{free} is the free charge density and $\mathbf{J}_{\text{f}}$ the free current density. Furthermore, the flux densities $\mathbf{D}$ and $\mathbf{B}$ are related to the field strengths $\mathbf{E}$ and $\mathbf{H}$ through material equations

$$\mathbf{D} = \varepsilon \mathbf{E}, \tag{2.5}$$

$$\mathbf{B} = \mu \mathbf{H}, \tag{2.6}$$

where ε is the permittivity and μ is the permeability of the medium. These equations are also sometimes written as

$$\mathbf{D} = \varepsilon_0 \mathbf{E} + \mathbf{P}, \tag{2.7}$$

$$\mathbf{B} = \mu_0 \mathbf{H} + \mathbf{M}, \tag{2.8}$$

[2]Maxwell's equations fail to hold for some quantum mechanical situations such as vacuum polarization with extremely strong fields [41].

where ε_0 is the vacuum permittivity, μ_0 is the vacuum permeability, $\mathbf{P}$ is the induced polarization and $\mathbf{M}$ the induced magnetization. These forms of the material equations are more general in the sense that the material responses are not necessarily assumed to be instantaneous or linear. The general form of the polarization $\mathbf{P}$ is

$$\mathbf{P} = \mathbf{P}_{\mathrm{L}} + \mathbf{P}_{\mathrm{NL}} = \varepsilon_0 \chi^{(1)} * \mathbf{E} + \varepsilon_0 \sum_{n=2}^{\infty} \chi^{(n)} * \mathbf{E}^n, \tag{2.9}$$

where $\mathbf{P}_{\mathrm{L}}$ is the linear polarization, $\mathbf{P}_{\mathrm{NL}}$ is the nonlinear polarization, $\chi^{(n)}$ is the n^{th} order susceptibility, an $(n+1)^{\mathrm{th}}$ order tensor, and $*$ denotes convolution [3]. Note that with the exception of the constant ε_0, all the variables in equation 2.9 are functions of t and $\mathbf{r}$ but the temporal and spatial dependencies have been dropped to shorten the notation. The n^{th} order convolution $\chi^{(n)} * \mathbf{E}^n$ is a nested integral over n dummy variables such that for example the third-order polarization is

$$\varepsilon_0 \chi^{(3)} * \mathbf{E}^3 = \varepsilon_0 \iiint_{\mathbb{R}^3} \chi^{(3)}(t-t_1, t-t_2, t-t_3) \vdots \mathbf{E}(\mathbf{r}, t_1)\mathbf{E}(\mathbf{r}, t_2)\mathbf{E}(\mathbf{r}, t_3) dt_1 dt_2 dt_3. \tag{2.10}$$

Maxwell's equations are sometimes expressed in their integral form depending on the application [42]. The four Maxwell's equations can be reduced to two by using the concepts of differential form and exterior derivative and treating the electric field as a 1-form and the magnetic field as a 2-form [43, 44]. Quaternion formalism, which was, to some degree, also used by Maxwell himself, allows one express all of the four equations with a single equation without loss of information or generality [45].

Equation 2.1, is called Gauss's law for electric fields. Since the divergence operator measures the magnitude of a vector field's sources (or sinks), equation 2.1 describes how free electric charges act as the sources of an electric field. Equation 2.2 is Gauss's law for magnetic fields and it tells that for every magnetic north pole there is a compensating south pole, which makes the divergence of the magnetic flux density vanish. No magnetic monopoles exist. Equation 2.3 is Faraday's induction law, which Faraday derived by observing that a time-varying magnetic flux passing through a closed conducting loop induces an electric current in the loop. However, since the creation of an electric field does not require a conducting loop, Faraday's law does not make any reference to one, and a changing magnetic flux density always has an associated electric field. Equation 2.4 is the Ampère-Maxwell law that describes how time-varying electric fields and electric currents give rise to magnetic fields. Maxwell's contribution to this was the derivative term known as the displacement current, which accounts for the special cases where Ampère's law

fails to hold. [2, 42]

2.2 Quantum Theory of Light

Around year 1900 Jules Henri Poincaré and Albert Einstein were among the prominent physicists who rejected aether. Poincaré had noticed that one could only observe relative displacements and no experiment was able to determine motion with respect to aether. Einstein did not believe that an "absolutely stationary space" was even necessary for anything and he postulated that light always propagates in empty space with a definite velocity c, which can be derived from the assumption that Maxwell's equations hold in every inertial coordination. This led Einstein to develop the theory of special relativity and showed that a deeper understanding of optics and the behavior of light can profoundly affect the way we look at everything. Assuming that Maxwell's equations are valid in every inertial coordination and concluding that mass is a form of energy is not a milestone, it is a paradigm shift. [2, 42]

In October 1900 Max Planck introduced the foundations of what is nowadays known as quantum mechanics, quantum physics or quantum theory [2]. Planck had developed the theory in order to avoid the so called *ultraviolet catastrophe* by making a thoroughly radical assumption that electromagnetic radiation was always emitted and absorbed in small packets, or *quanta*, of energy [46]. At that time there was little reason to make such an assumption, but accepting the quantum hypothesis allowed one to correctly predict the observed spectra of black body radiation. Einstein further proposed that not only was light emitted and absorbed in quanta, but radiation itself consisted of quanta [46]. Quantum theory became an integral part of optics, as it allowed Einstein to explain the photoelectric effect that Hertz had discovered in 1887. Further developments and reformulations in quantum theory were made in the 1920's by Sommerfeld [47], Heisenberg [48], Bohr [49], De Broglie [50], Born [51], Dirac [52], Schrödinger [53], Pauli [54], and others. By the end of the decade, quantum mechanics had become a well-verified theory [2].

Quanta of electromagnetic radiation are called *photons*, and one of the key features of quantum theory of light is that each photon has an associated energy equal to

$$E_{\text{photon}} = h_{\text{P}} f, \tag{2.11}$$

where f is the frequency of the photon and $h_{\text{P}} \approx 6.626 \cdot 10^{-34}$ m^{2}kg/s is the famous proportionality constant known as *Planck's constant*. Equation 2.11 is also one of the manifestations of *wave-particle duality* since the left hand side is the energy of a photon, which is thought of as a particle, but the right hand side tells that the

energy of the particle depends on frequency, which in turn is clearly a property of vibration, oscillation, or a wave.

Because Planck's constant is so tiny, the number of photons in most practical situations is huge. Even an ordinary 1 mW red laser pointer produces quadrillions of photons every second. Therefore, the classical electromagnetic formulation can be used to model light propagation accurately, and quantum effects, such as shot noise, can also be incorporated into the classical model.

3. PROPAGATION OF LIGHT

Every beam of electromagnetic radiation consists of a discrete number of photons and each photon has a specific frequency. According to equation 2.11, photons with different frequencies have different energies and interact differently with the atoms of the medium in which they propagate. The variations in the microscopic dynamics of interactions lead to macroscopic effects such as *chromatic dispersion* or simply dispersion, which means that the velocity of light in a medium depends on its frequency. In order to study how an arbitrary electromagnetic pulse propagates through a medium, it is necessary to know the frequency content of the pulse. It is therefore beneficial to rewrite Maxwell's equations in the frequency domain.

Consider a sourceless dielectric ($\rho_{\text{free}} = 0$) and assume that there are no free currents ($\mathbf{J}_{\text{f}} = \mathbf{0}$). Also assume, for simplicity, that the susceptibilities[1] χ and χ_{m} can be treated as scalars either because of isotropy or because the state of polarization is maintained, which are very good approximations for a plethora of materials and purposes [2, 55]. The dielectric is also assumed to be nonmagnetic ($\chi_{\text{m}} = 0$ and $\mathbf{M} = \mathbf{0}$). Nonlinear optical effects typically require intensities so high that only a powerful laser is capable of producing them [3], but in order to keep the derivation more general, it will not be assumed that the material is linear. Instead, χ is allowed to depend on field strength.

Polarization $\mathbf{P}$ is now given by $\mathbf{P} = \varepsilon_0 \chi^{(1)} * \mathbf{E} + \mathbf{P}_{\text{NL}}$, where $\mathbf{P}_{\text{NL}}$ is the nonlinear part of the polarization. The material equations 2.7 and 2.8 can now be written as

$$\mathbf{D} = \varepsilon_0 \mathbf{E} + \varepsilon_0 \chi^{(1)} * \mathbf{E} + \mathbf{P}_{\text{NL}}, \tag{3.1}$$

$$\mathbf{B} = \mu_0 \mathbf{H}, \tag{3.2}$$

for the medium in question. Now taking the curl of equation 2.3, justifiably interchanging the curl and the time derivative on the right hand side and furthermore

[1] Susceptibilities are related to the permittivity and permeability by $\varepsilon = (1 + \chi)\varepsilon_0$ and $\mu = (1 + \chi_{\text{m}})\mu_0$.

plugging in equation 3.2 yields

$$\nabla \times \nabla \times \mathbf{E} = -\mu_0 \frac{\partial}{\partial t} \left(\nabla \times \mathbf{H} \right). \tag{3.3}$$

Now using equations 2.4 and 3.1 while keeping in mind that $\mathbf{J}_\mathrm{f} = \mathbf{0}$ gives

$$\nabla \times \nabla \times \mathbf{E} = -\mu_0 \varepsilon_0 \frac{\partial^2}{\partial t^2} \left(\mathbf{E} + \chi^{(1)} * \mathbf{E} \right) - \mu_0 \frac{\partial^2}{\partial t^2} \mathbf{P}_\mathrm{NL} \tag{3.4}$$

$$= -\frac{1}{c^2} \frac{\partial^2}{\partial t^2} \left(\mathbf{E} + \chi^{(1)} * \mathbf{E} \right) - \mu_0 \frac{\partial^2}{\partial t^2} \mathbf{P}_\mathrm{NL}. \tag{3.5}$$

By making use of the vector calculus identity $\nabla \times \nabla \times \tilde{\mathbf{E}} = \nabla \left(\nabla \cdot \tilde{\mathbf{E}} \right) - \nabla^2 \tilde{\mathbf{E}}$ equation 3.5 can be written as

$$\nabla \left(\nabla \cdot \mathbf{E} \right) - \nabla^2 \mathbf{E} = -\frac{1}{c^2} \frac{\partial^2}{\partial t^2} \left(\mathbf{E} + \chi^{(1)} * \mathbf{E} \right) - \mu_0 \frac{\partial^2}{\partial t^2} \mathbf{P}_\mathrm{NL}. \tag{3.6}$$

The first term of the left hand side of equation 3.6 can be shown to be zero for some cases, such as step-index fibers, and negligible in a myriad of other cases of interest, such as when $\chi^{(1)}$ is approximately constant over one wavelength [3, 4]. By making use of this approximation that $\nabla \left(\nabla \cdot \mathbf{E} \right) \approx \mathbf{0}$, equation 3.6 can be written as

$$-\nabla^2 \mathbf{E} = -\frac{1}{c^2} \frac{\partial^2}{\partial t^2} \left(\mathbf{E} + \chi^{(1)} * \mathbf{E} \right) - \mu_0 \frac{\partial^2}{\partial t^2} \mathbf{P}_\mathrm{NL}. \tag{3.7}$$

Taking the Fourier transform of equation 3.7 gives

$$-\nabla^2 \tilde{\mathbf{E}} = \frac{\omega^2}{c^2} \left(1 + \tilde{\chi}^{(1)} \right) \tilde{\mathbf{E}} + \mu_0 \omega^2 \tilde{\mathbf{P}}_\mathrm{NL} \tag{3.8}$$

$$= \frac{\omega^2}{c^2} \left(1 + \tilde{\chi}^{(1)} \right) \tilde{\mathbf{E}} + \frac{1}{\varepsilon_0} \frac{\omega^2}{c^2} \tilde{\mathbf{P}}_\mathrm{NL}. \tag{3.9}$$

ω^2/c^2 is simply the vacuum wave number k_0, and $1 + \tilde{\chi}^{(1)}$ is the square of the frequency-dependent *refractive index*: $1 + \tilde{\chi}^{(1)} = n^2(\omega)$. The wave number in the medium is $k(\omega) = n(\omega) k_0$. Thus,

$$-\nabla^2 \tilde{\mathbf{E}} = k^2(\omega) \tilde{\mathbf{E}} + \frac{k_0^2}{\varepsilon_0} \tilde{\mathbf{P}}_\mathrm{NL}. \tag{3.10}$$

Regardless of the assumptions and the simplifications, equation 3.10 is very general. Losses are included in the index of refraction, and the nonlinear polarization term can account for many different effects, such as Kerr and Pockels effects and Raman scattering. Assuming that $n(\omega)$ is spatially independent and that no nonlinear effects

are present, the equation simplifies to the ordinary *Helmholtz equation*:

$$\nabla^2\tilde{\mathbf{E}} + k^2(\omega)\tilde{\mathbf{E}} = 0. \tag{3.11}$$

3.1 Optical Fibers

By careful adjustment of the spatial dependence of the refractive index $n(\omega)$, one can hope to tailor the solutions of equation 3.10, and optical fibers do just this. From a mathematical point of view, it is convenient to describe a fiber simply as a medium, the refractive index of which has a certain spatial dependence on x, y (and ω). Usually fibers have cylindrical symmetry such that $n(\omega)$ is a function of $\rho = \sqrt{x^2 + y^2}$ only. The (x, y)-dependence of the refractive index is physically achieved by using different materials for different layers of the fiber. The most typical cylindrically symmetric fiber is a thin rod of material with a refrative index n_1 surrounded by material with a lower refractive index n_2. The surrounding material could be air, which would result in a very simple fiber consisting of nothing but a rod of glass, for example. Nothing restricts us to solid materials, and the fundamental phenomena behind optical fibers can be (and have been) demonstrated using a stream of water. However, it will be shown that for many applications it is beneficial to make n_2 only slightly lower than n_1, which in practice means surrounding the fiber *core* with a *cladding* layer. Usually the core and cladding are made of the same material, but the core has been doped with an additional substance in order to make its index of refraction higher [4].

3.2 Wave Propagation in Step-Index Fiber

The step-index fiber is probably the simplest case, but understanding how electromagnetic waves propagate in such fibers gives practical insight into propagation in other types of fibers, too. Consider a step-index fiber concentric with the z-axis. The fiber is described by a refractive index profile

$$n(\rho) = \begin{cases} n_1, & \rho \leq a \\ n_2, & \rho > a \end{cases}, \tag{3.12}$$

where $\rho = \sqrt{x^2 + y^2}$ and a is the fiber core radius. Note that we are assuming an infinite cladding layer, but we will see that this is of no concern. Because of the cylindrical symmetry, we will express equation 3.11 in cylindrical coordinates ρ, ϕ and z such that $x = \rho\cos\phi$ and $y = \rho\sin\phi$. The Helmholtz equation 3.11 then reads

$$\frac{\partial^2\tilde{\mathbf{E}}}{\partial\rho^2} + \frac{1}{\rho}\frac{\partial\tilde{\mathbf{E}}}{\partial\rho} + \frac{1}{\rho^2}\frac{\partial^2\tilde{\mathbf{E}}}{\partial\phi^2} + \frac{\partial^2\tilde{\mathbf{E}}}{\partial z^2} + k^2(\omega)\tilde{\mathbf{E}} = 0. \tag{3.13}$$

Now $k^2(\omega) = k_0^2 n_1^2$ inside the the fiber core and $k^2(\omega) = k_0^2 n_2^2$ outside the core, where the ω-dependence of n_1 and n_2 has been left out to shorten the notation. A similar equation can be derived for the magnetic field strength $\tilde{\mathbf{H}}$, and as $\tilde{\mathbf{E}}$ and $\tilde{\mathbf{H}}$ must also satisfy Maxwell's equations, only two components of the six $\tilde{E}_\rho$, $\tilde{E}_\phi$, $\tilde{E}_z$, $\tilde{H}_\rho$, $\tilde{H}_\phi$, $\tilde{H}_z$ are independent [56]. Typically $\tilde{E}_z$ and $\tilde{H}_z$ are chosen and they can be seen to satisfy equation 3.13.

The Helmholtz equation can be shown to be separable in cylindrical coordinates for a constant k using Stäckel determinants [57]. We can thus solve the equation in the core and in the cladding by separation of variables and then require the tangential component of the electric and magnetic fields be continuous at the core-cladding interface. The general form of such a separable solution can be shown to be

$$\tilde{E}_z(\omega, \rho, \phi, z) = A(\omega) F(\omega, \rho) \exp(\pm i m \phi) \exp(i \beta z), \tag{3.14}$$

where $A(\omega)$ is the amplitude of the frequency component oscillating at ω, β is the propagation constant that takes the role of the wave number k, m is an integer and $F(\omega, \rho)$ is a solution of

$$\frac{d^2 F}{d\rho^2} + \frac{1}{\rho}\frac{dF}{d\rho} + \left(k^2 - \beta^2 - \frac{m^2}{\rho^2}\right) F = 0, \tag{3.15}$$

where $k = k_0 n_1$ for $\rho \leq a$ and $k = k_0 n_2$ for $\rho > a$. Note that k and β depend on ω. Equation 3.15 is Bessel's differential equation, and the physically feasible (i.e. no singularities, finite energy, differentiable) solutions are given by

$$F(\omega, \rho) = \begin{cases} J_m(\kappa\rho), & \rho \leq a \\ K_m(\gamma\rho), & \rho > a \end{cases}, \tag{3.16}$$

where $\kappa = \sqrt{n_1^2 k_0^2 - \beta^2}$ and $\gamma = \sqrt{\beta^2 - n_2^2 k_0^2}$, and J_m and K_m are the Bessel function and the modified Bessel function of order m, respectively. Because K_m is an exponentially decaying function, the cladding does not have to be infinite in practice but thick enough so that $K_m(\gamma\rho)$ becomes negligible at the fiber boundary. $\tilde{H}_z$ can be obtained in a similar manner [56]. The boundary condition that the tangential components of $\tilde{\mathbf{E}}$ and $\tilde{\mathbf{H}}$ are continuous means that $\tilde{E}_z$, $\tilde{H}_z$, $\tilde{E}_\phi$, and $\tilde{H}_\phi$ are to be continuous at $\rho = a$, which transfers to the following eigenvalue equation [56]:

$$\left[\frac{J_m'(\kappa a)}{\kappa J_m(\kappa a)} + \frac{K_m'(\gamma a)}{\gamma K_m(\gamma a)}\right]\left[\frac{J_m'(\kappa a)}{\kappa J_m(\kappa a)} + \frac{n_2^2}{n_1^2}\frac{K_m'(\gamma a)}{\gamma K_m(\gamma a)}\right] = \left(\frac{m\beta k_0 (n_1^2 - n_2^2)}{a n_1 \kappa^2 \gamma^2}\right)^2. \tag{3.17}$$

In general, equation 3.17 has multiple solutions for β for each integer value of m. The solutions are usually denoted by β_{mn}, and each β_{mn} corresponds to a specific *mode* supported by the fiber, and the corresponding modal field distribution can be obtained from equation 3.14 [56]. Note, however, that imaginary electric fields are physically infeasible, and one has to take the real part of the complex distribution to get the physical electric field distribution. Figure 3.1 shows the intensity distribution for eight different modes.

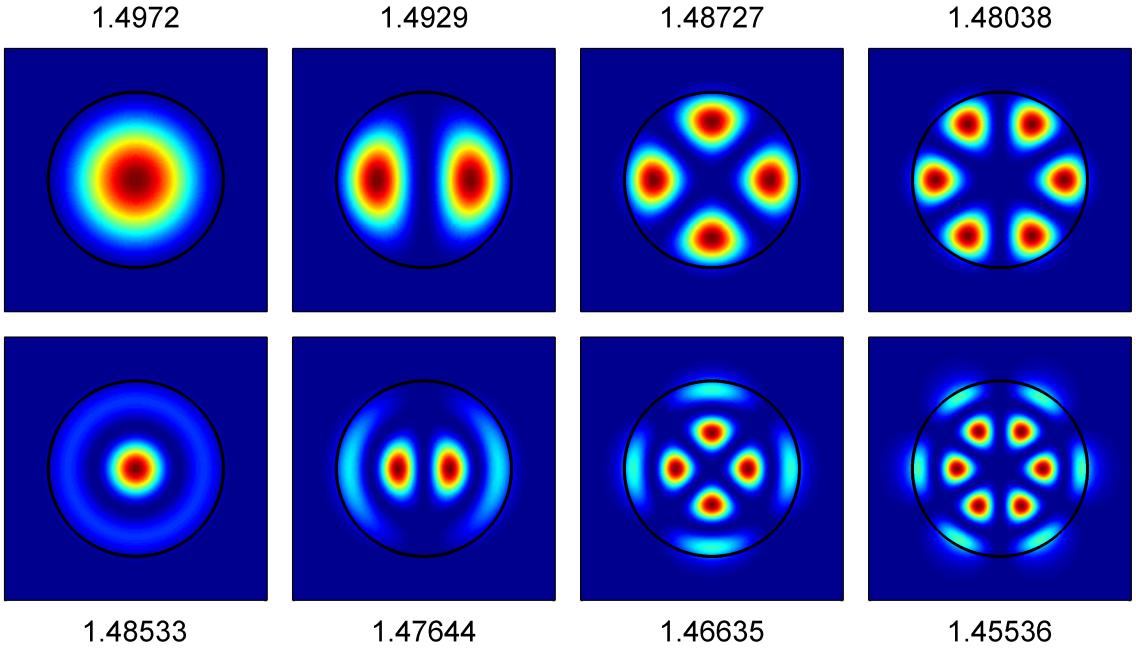

Figure 3.1: *Transverse intensity profiles of some of the supported modes of a fiber. The core radius of the fiber is $a = 2\ \mu m$, the refractive index of the core $n_1 = 1.5$, and the refractive index of the cladding $n_2 = 1.45$. The wavelength is 532 nm, which corresponds to a typical green DPSSFD laser pointer. The mode corresponding to β_{mn} is on the $(m+1)^{th}$ row and $(n+1)^{th}$ column, and the respective modal indices $\bar{n} = \beta_{mn}/k_0$ are shown next to the plots. This fiber supports altogether 13 modes at the wavelength in question: 7 for $m = 0$, 4 for $m = 1$, and 2 for $m = 2$.*

There are two different types of modes, denoted by HE_{mn} and EH_{mn}, corresponding to the polarization of the field [56]. In practical situations all but the transverse components of the electric field and the magnetic field are negligible, which simplifies the mathematical treatment considerably, as it allows for scalar equations. However, the existence of these two kinds of modes is important nevertheless because of possible birefringence: HE_{mn} and EH_{mn} might propagate at different speeds. This is called *polarization mode dispersion* (PMD) and will be discussed in more detail later. [56]

The usefulness of modes lies behind the fact that the modes were obtained from an eigenvalue equation and the modes are thus eigenfunctions. The propagating

electric field inside the fiber is therefore always a linear combination of fiber modes. Some linear combinations have their own names, such as the doughnut mode, which is a linear combination of two HE_{mn} or two EH_{mn} modes with $m = 0$, $n > 0$, and a certain relation between the polarizations and phases of the two modes such that the combined transverse intensity distribution is shaped like a ring.

The z-dependence of the electric field of the mode corresponding to β_{mn} can be seen from equation 3.14. The dependence is simply $\exp(i\beta_{mn}z)$, which describes a wave propagating in the z-direction. The time-dependence of a frequency component at ω is $\exp(-i\omega t)$, so the speed of this component is ω/β_{nm}. Recalling that the index of refraction is c divided by the speed of light in the medium, one is tempted to define a *modal index* or *effective refractive index* $\bar{n}_{mn} = \beta_{mn}c/\omega = \beta_{mn}/k_0$, where k_0 is the vacuum wave number. The modal index is smaller for larger m and n and remains between the core and cladding indices n_1 and n_2, which can be seen in figure 3.1. The physical explanation is that for large m and n, a larger portion of the intensity is confined in the cladding where light propagates faster. This is especially visible in figure 3.1 for the rightmost mode in the lower row.

Because the modal index is different for each mode, different modes propagate at different velocities. This is called *intermodal dispersion*. Needless to say, like all kinds of dispersion, also intermodal dispersion limits the performance of optical communication systems in the general case. Consider for example the two leftmost modes in figure 3.1, the modal indices of which are approximately 1.497200 and 1.485327. Assume we have a narrow initial pulse, the energy of which is more or less equally divided between the two modes. After 10 km of propagation in the fiber, the pulse has been split in two pulses that are separated by approximately 390 nanoseconds, which means a bit rate limitation of 2.6 Mbps due to intermodal dispersion alone. While 2.6 Mbps might be better than a semaphore line, it is nowhere near what can be achieved using a single mode fiber, and it is thus usually beneficial to have the fiber support the HE_{00} and EH_{00} modes only. HE_{00} is referred to as the *fundamental mode* (HE_{11} in some notations).

3.3 Single-Mode Operation and Properties of the Fundamental Mode

The number of supported modes is determined by the number of solutions to the eigenvalue equation 3.17, so if the equation can be set to have only one solution, the fiber will only support one mode. It is useful to define a normalized frequency or

the V-parameter as

$$V = \frac{2\pi}{\lambda_0} a \sqrt{n_1^2 - n_2^2}, \tag{3.18}$$

where λ_0 is the wavelength in vacuum. The magnitude of V determines the supported modes, and the cutoff condition in terms of V can be derived for every mode [55]. Since we are only interested in single-mode operation, it suffices to state the *single-mode condition*: $V = V_c$, where $V_c \approx 2.405$ is the first zero of the Bessel function J_0 (i.e. the smallest positive solution of $J_0(V_c) = 0$). Even though single-mode operation could be guaranteed by making V small by tuning the refractive indices or making the core diameter small, the V-parameters of single-mode fibers are usually in the range 2.0-2.4 [4]. This is because fibers with a small V-parameter have higher bending losses, which is also intuitevely clear: it is harder for the light to stay in the core if the core diameter is small or the refractive index of the cladding is close to that of the core.

The transverse intensity profile of the fundamental mode was derived in section 3.2 and is given by

$$F(\rho) = \begin{cases} J_0(\kappa\rho), & \rho \leq a \\ K_0(\gamma\rho), & \rho > a \end{cases}, \tag{3.19}$$

where $\kappa = \sqrt{n_1^2 k_0^2 - \beta^2}$, $\gamma = \sqrt{\beta^2 - n_2^2 k_0^2}$, and $\rho = \sqrt{x^2 + y^2}$ is the radial distance from the fiber center. Although the intensity distribution could be solved analytically, piecewise defined functions involving Bessel functions are difficult to deal with, and it is customary to use a Gaussian approximation:

$$F(\rho) \approx \exp\left(-\frac{\rho^2}{w^2}\right), \tag{3.20}$$

where the width parameter w is determined by fitting the Gaussian function to the exact solution. For V-parameter values between 2 and 3, the width parameter is approximately equal to the core radius a and the ratio w/a increases with decreasing V [56]. Thus, for smaller values of V, a significant portion of the light travels in the cladding.

3.4 Dispersion

The frequency-dependence of the refractive index, which leads to chromatic dispersion, is not the only source of dispersion. Other properties of light or the medium can affect the speed of light as well. Light intensity is one property that affects the speed of light, and in the context of water waves this would be called *amplitude dispersion*. In optics, however, the frequency-dependence of the refractive index is typically treated in the context of nonlinearities, and this thesis also has a section

devoted to nonlinear optical effects. This section briefly discusses different types of dispersion.

3.4.1 Chromatic Dispersion

The physical meaning of the refractive index $n(\omega)$ is that the velocity of the frequency component at ω is $v = c/n(\omega)$. In other words, the refractive index is the ratio of the vacuum speed of light and the speed of light in the medium. The frequency-dependence of the refractive index is thus responsible for the aforementioned chromatic dispersion in bulk media.

The situation is somewhat different in optical fibers because the propagation speed of a certain frequency component depends not only on the corresponding bulk refractive index but also on waveguide geometry. The bulk effect is then referred to as *material dispersion* and the dependence on waveguide geometry is known as *waveguide dispersion*. Waveguide dispersion arises because the transverse modal distribution given by equation 3.16 depends on the wavelength and some frequencies are more concentrated in the fiber core that has a higher refractive index. Frequency components that penetrate more deeply into the cladding layer experience an overall lower refractive index and thus propagate faster.

Both material and waveguide dispersion contribute to the chromatic dispersion in fibers, and both of them are incorporated into the mathematical model via the frequency-dependence of the propagation constant $\beta(\omega)$. The exact functional form of $\beta(\omega)$ is practically never known, and a Taylor approximation in the vicinity of a frequency of interest ω_0 (usually the central frequency of an input pulse) has to be used:

$$\beta(\omega) \approx \sum_{n=0}^{N} \frac{\beta_n}{n!}(\omega - \omega_0)^n \tag{3.21}$$

As is known from basic Fourier analysis, a short pulse must have a broad spectrum, and a narrow spectrum means a long pulse. A long pulse might also have a broad spectrum if the pulse is chirped, and the amount of terms needed in the Taylor approximation depends on how broad the spectrum is. Because of chromatic dispersion, the velocities of different spectral components of a pulse can differ significantly. This can cause pulses to broaden and become chirped, and chromatic dispersion is of utmost importance in nearly every fiber optical system simply because of its effect on light pulses.

Some of the Taylor series coefficients in expansion 3.21 have a clear physical meaning. The first derivative is the inverse of the *group velocity*: $v_\mathrm{g} = \beta_1^{-1} = (\partial\beta/\partial\omega)^{-1}$,

and the physical meaning of the group velocity is that the envelope of a wave packet propagates at the group velocity. The second derivative β_2 is responsible for *group-velocity dispersion* (GVD), which leads to pulse broadening, and β_2 is called the GVD parameter. The temporal broadening of a pulse is governed by $\Delta T = L\beta_2\Delta\omega$, where L is the length of the fiber and $\Delta\omega$ is the spectral width of the pulse [4]. Second-order dispersion also causes pulses to become chirped. The sign of β_2 has a tremendous impact on pulse propagation, and the case $\beta_2 < 0$, which is known as *anomalous dispersion*, is usually the most interesting one in fiber optics because it allows for more versatile phenomena [4, 28, 56, 58]. The situation $\beta_2 > 0$ is referred to as *normal dispersion*, and it would cause the high-frequency components lag behind the low-frequency ones causing positive chirp on the pulse, as shown in figure 3.2 that shows the analytically solved propagation of a Gaussian pulse. Figure 3.2 also shows how the pulse envelope remains Gaussian in the absence of higher-order dispersion, although the pulse broadens, flattens, and develops the already mentioned positive chirp. Note that higher-order dispersion would both make the exact solution mathematically very difficult and distort the Gaussian envelope shape (see figure 3.3) [4].

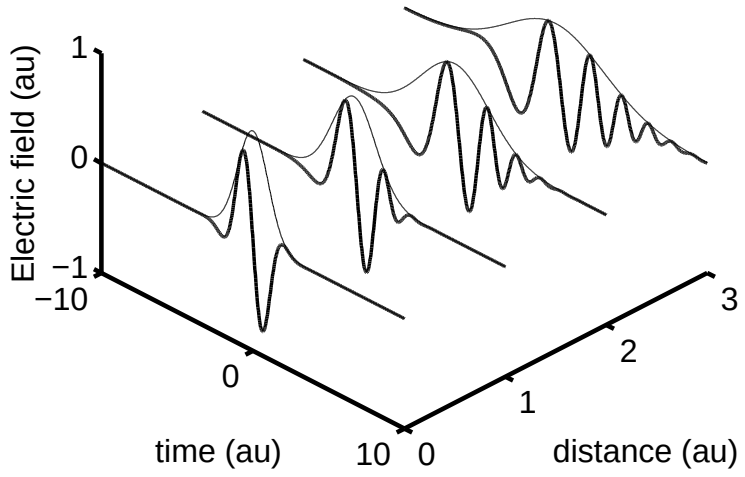

Figure 3.2: *Evolution of the electric field (thick line) and the envelope (thin line) of a Gaussian pulse experiencing dispersion up to second order. The pulse envelope remains Gaussian upon propagation, but second-order dispersion causes the pulse to broaden, flatten, and develop a chirp.*

Between the regions of normal and anomalous dispersion lies the condition $\beta_2 = 0$. The wavelength, for which this happens, is termed the *zero-dispersion wavelength* (ZDW), and there might be more than one such wavelengths [59]. Because the magnitude of pulse broadening is governed by β_2 via a linear relation, pulses with a central wavelength near the ZDW experience the least broadening. Pure silica has a ZDW of 1.276 μm, and the ZDW of silica fibers usually varies in the range $1.28 - 1.31$ μm due to doping and the effect of waveguide dispersion. Thus, pulses

with a central wavelength around 1.3 μm usually experience the least broadening in silica fibers, and it would therefore be beneficial to operate optical communication systems in the vicinity of 1.3 μm. However, losses are quite high at that wavelength, and high losses would necessitate the use of higher pulse energies, which is, of course, undesirable from a practical point of view. The losses can be made smaller by for example reducing the amount of H_2O molecules caught inside the fiber during the manufacturing process [4]. Even the purest of silica fibers are not completely lossless simply because the silica molecules can absorb photons, and instead of trying to reduce the losses around 1.3 μm physicists have come up with a more cunning technique of *dispersion shifting* [60, 61, 62]. Dispersion shifting means changing waveguide and material dispersion through modifying waveguide geometry and/or the refractive index profile by doping the core and the cladding in such a way that the ZDW falls in a desired location. The ZDW can be made to coincide with the wavelength that experiences the lowest losses (1.55 μm). These kind of fibers are very suitable for optical communication applications because of low losses and low GVD. β_2 can also be made small over a wide range of wavelengths, and fibers like this are known as *dispersion flattened fibers* [4]. Because of this property, dispersion flattened fibers are suitable for multichannel optical communication applications, where pulses of different central frequencies copropagate.

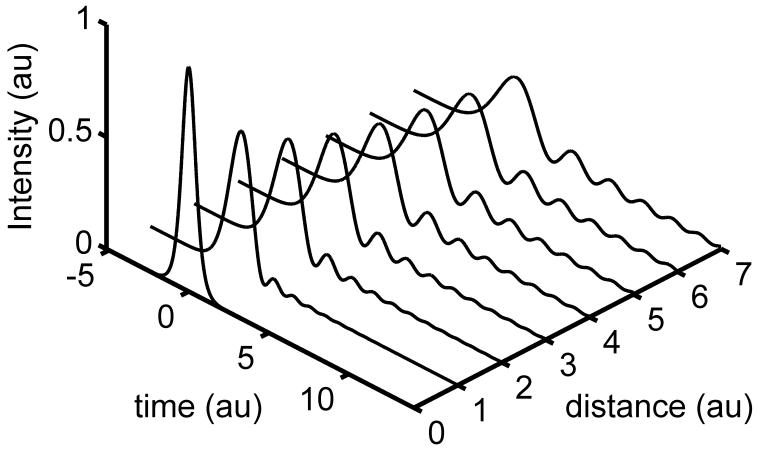

Figure 3.3: *The evolution of the temporal intensity profile of an initially unchirped Gaussian pulse under the influence of third-order dispersion. The intensity profile becomes asymmetric and developes an oscillatory tail upon propagation.*

When the central wavelength of the pulse in question is close to the ZDW, it becomes necessary to include third-order dispersion (TOD) β_3 in the Taylor series 3.21. Similarly, the second-order Taylor approximation around ω_0 is only valid in a certain range near ω_0, and if the pulse spectrum is wider than this range, more terms have to be included in the Taylor series. The effect of third-order dispersion on pulses is to make the pulse envelope asymmetric and cause oscillatory behavior in

one or both of the edges depending on pulse shape. Usually the oscillatory behavior occurs in the trailing edge for unchirped symmetric pulses as shown in figure 3.3. The broadening (RMS-width) of a Gaussian pulse can still be solved analytically when third-order dispersion is included in the model. [56]

The effects of dispersion of orders higher than three are far less intuitive, but the higher-order terms have to be included in the model because the spectrum becomes, by definition, very broad during supercontinuum generation. While the inclusion of dispersion only up to the second or third order simplifies analytical treatments and is sufficient for studies regarding the propagation of spectrally narrow single pulses, the lack of higher-order dispersion terms will yield unphysical results when the pulse spectrum becomes broad.

3.4.2 Intermodal Dispersion

The solutions β_{mn} of the eigenvalue equation 3.17 depend on the values of m and n, which means that the propagation constant is different for different modes of the fiber and different modes thus propagate at different speeds. Although the situation in planar waveguides is a bit different than in fibers, the geometric perspective of wave propagation in planar waveguides offers an insightful explanation of intermodal dispersion. The simplest planar waveguide consists of two paraller mirrors, and light bounces back and forth between the mirros. The reflection upon the mirrors corresponds to the total internal reflection present in step-index fibers. Solving Maxwell's equation for the planar waveguide yields the modes of the waveguide. One can then show that in the geometric interpretation, where light travels as rays in straight lines, the modes correspond to rays that fulfill the so-called *self-consistency condition* which means that the wavefront must reproduce itself after two reflections as shown in figure 3.4 [63].

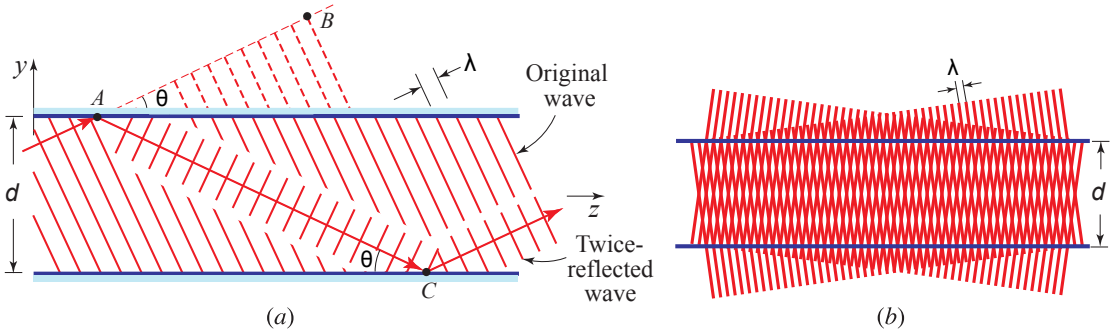

Figure 3.4: *(a) A planar waveguide and a self-consistent ray of light. (b) The copropagation of self-consistent rays leads to an intensity distribution that is constant over the length of the waveguide. (After reference [63].)*

There are multiple values of the propagation angle θ that lead to the fulfillment of the self-consistency condition, and it is evident that the larger the propagation angle, the slower the ray propagates in the z-direction. Thus, in the geometrical picture, some modes travel longer distances than others and therefore appear to travel slower. The situation is a bit different in optical fibers, but the principle is similar.

3.4.3 Polarization Mode Dispersion

All fibers support two degenerate modes polarized in orthogonal directions [56]. The propagation constants for these two modes are in general different because of birefringence, which means that the polarization components propagate at different speeds. The axis along which light has to be polarized in order to experience the lowest refractive index is called the *fast axis* because light polarized along that axis travels the fastest. The axis of the highest refractive index is called the *slow axis*. Unless the light is polarized along the fast or the slow axis, the state of polarization will change with propagation distance from linear to elliptical and back to linear in a periodic manner assuming the principal axes do not change their orientation [64]. This behavior is similar to the operational principle of wave plates [2]. However, because of the manufacturing process, the birefringence and the axes actually change randomly along the fiber [4]. This is due to random variations in the core shape, size, stress, and possible doping.

Even for fibers with randomly varying birefringenge, two principal axes exist, and light polarized along one of these axes will exit the fiber with its state of polarization maintained [56]. Usually, however, one does not know or care about the state of polarization, and the effect of PMD is simply to broaden the pulses. In order to measure this PMD-induced pulse broadening, a model for the random variations has to be developed. A very simple model could divide the fiber into small segments of constant birefringence such that the orientation of the fast axis and the magnitude of birefringence in each segment are randomly selected. Thus, in each segment one polarization component lags behind the other component by a certain time delay. This situation can easily be seen to be equivalent to the one-dimensional random walk, and the RMS-distance of such a random walk is known to obey the square-root law: when enough steps are taken, the expected positive distance from the initial location after N steps is proportional to $\sqrt{N}$. One might thus expect the PMD-induced pulse broadening in a fiber of length L to be proportional to $\sqrt{L}$, if the fiber is long enough. This turns out to be the case, as shown by the more detailed treatment by Foschini and Poole [65]. The fiber length L has to satisfy $L > l_c$, where l_c is the correlation length over which two polarization components remain

correlated (typically of the order of 100 meters) [56]. The typical fiber lengths used in SC generation tend to be much smaller than 100 meters, and it is customary to neglect the effects of birefringence and use the scalar propagation equation because it has been shown to agree with experiments [28], but some authors [66, 67] insist on using coupled equations to describe pulse propagation. PMD is more important in other optical applications, such as communication systems, as PMD-induced pulse broadening becomes a limiting factor for long-haul high-speed optical communication systems operating near the ZDW [68]. Interstingly enough, it has been shown [69] that accurate long-range measurements of PMD in fibers can be performed by using supercontinuum.

Some applications are sensitive to the polarization of the light, and it is sometimes desirable that the fiber does not alter the state of polarization of the light [56]. *Polarization-maintaining fibers* can be made by intentionally inducing a large amount of birefringence by either making the fiber core noncircular on purpose or by inserting stress-inducing elements (typically two borosilicate rods) on the opposite sides of the fiber core [70, 71]. The large magnitude of the intentionally induced birefringence masks smaller random variations, and light polarized along the fast or the slow axis will maintain its state of polarization. For highly birefringent fibers the polarization effects become important also in terms of SC generation, and this has been studied in microstructured fibers [72, 73]. In one of these studies Lehtonen et. al [72] pointed out that the different dispersion characteristics of the two eigenpolarizations make it possible to generate two orthogonally polarized supercontinua with different properties, and all the possible combinations of these allow for more supercontinuum tunability.

4. NONLINEAR EFFECTS IN FIBERS

In general, the response of a material to an external electric field is nonlinear and the nonlinear polarization

$$\mathbf{P}_{\mathrm{NL}}(\mathbf{r},t) = \varepsilon_0 \sum_{n=2}^{\infty} \chi^{(n)}(\mathbf{r},t) * \mathbf{E}^n(\mathbf{r},t) \tag{4.1}$$

cannot be neglected. In the general case, all higher-order effects have to be taken into account, but for centrosymmetric materials, such as silica, all even order susceptibilities can be shown to be zero. Although fifth-order susceptibilities as high as $1.9 \cdot 10^{-12}$ $(\mathrm{m/V})^4$ have been reported for gases of cold atoms [74], the fifth-order effects usually require intensities high enough to ionize the material, in which case the model obviously does not even work anymore. For reasonably low optical intensities in silica fibers all but the third-order contributions can be neglected. Alternatively, a possible way to take higher-order nonlinearities into account is to make the third-order susceptibility intensity-dependent appropriately [56]. In this thesis, susceptibilities of order higher than three will not be considered. The nonlinear polarization then reduces to

$$\mathbf{P}_{\mathrm{NL}}(\mathbf{r},t) = \varepsilon_0 \iiint_{\mathbb{R}^3} \chi^{(3)}(t-t_1, t-t_2, t-t_3) \vdots \mathbf{E}(\mathbf{r},t_1)\mathbf{E}(\mathbf{r},t_2)\mathbf{E}(\mathbf{r},t_3) dt_1 dt_2 dt_3. \tag{4.2}$$

The tensorial nature of the third-order susceptibility allows for phenomena such as nonlinear birefringence, but we can justifiably treat $\chi^{(3)}$ as a scalar for most purposes.

The third-order response in optical fibers is mostly due to the instantaneous[1] electronic response and partially due to the delayed molecular response. The molecular response, the Raman effect, happens on a timescale from 60 to 70 femtoseconds [56].

Taking the Fourier transform of equation 4.2 yields

$$\tilde{\mathbf{P}}_{\mathrm{NL}}(\mathbf{r},\omega) = \varepsilon_0 \chi^{(3)}(\omega_1,\omega_2,\omega_3)\tilde{\mathbf{E}}(\mathbf{r},\omega_1)\tilde{\mathbf{E}}(\mathbf{r},\omega_2)\tilde{\mathbf{E}}(\mathbf{r},\omega_3), \tag{4.3}$$

[1] electronic response times are of the order 0.1 fs, a time scale similar to the period of revolution for an electron in a Bohr orbit.

and this frequency domain treatment is usually simpler because the convolutions turn into multiplications.

Although the third-order susceptibility is the only higher-order susceptibility of interest in the case of silica fibers, not all third-order phenomena are of interest when considering nonlinear propagation of light in silica fibers. This section discusses different third-order phenomena in fibers.

4.1 Third-Harmonic Generation

Third-harmonic generation (THG) or frequency tripling is a process where part of the energy of light at frequency ω is converted into light at 3ω. Here, THG refers solely to the $\chi^{(3)}$-process, although the third-harmonic can also be generated through a cascaded second-order process (namely, frequency doubling followed by sum-frequency generation). THG was first observed experimentally in 1962 using calcite crystals [75].

Chromatic dispersion causes the third-harmonic field at 3ω and the fundamental field at ω to propagate at different speeds in the medium. Because the third-harmonic is generated throughout the medium, it is intuitively easy to understand that the third-harmonic electric fields generated in different parts of the medium are out-of-phase and cancel out due to this *phase-mismatch*. A rigorous treatment of this phenomenon requires a more thorough quantum-electrodynamical approach [3], but it suffices to state that because of the phase-mismatch, THG is not an efficient process unless specific care is taken to ensure that the fundamental field and the third-harmonic propagate at the same speed.

Phase-mathcing can be achieved because other types of dispersion can, in some circumstances, cancel chromatic dispersion. The most typical scheme exploits PMD, but the use of modal dispersion in harmonic generation has also been reported for example in microstructured fibers [76]. PMD-based phase-matching relies on birefringence and the tensorial nature of the nonlinear susceptibility. In other words, light polarized along the ordinary or the extraordinary axis can create higher-order harmonics that are polarized along the other axis, and birefringence and careful adjustment of the polarization angle make it possible to achieve such a situation that the higher-order field and the fundamental field propagate at the same speed.

4.2 Kerr-Effect

Kerr-effect is the name given to the phenomenon in which the refractive index of light depends on the square of the electric field. Although the observation of the Kerr-effect in optical fibers requires the use of intense laser fields, the Kerr-effect was discovered as early as 1875 by the Scottish physicist John Kerr. This is due to the fact that the electric field used in the early experiments was a static one: a DC field changes the refractive index of a crystal in which light propagates. In nonlinear fiber optics, the change in the refractive index is caused by the electric field of the light itself, but the DC Kerr-effect is still exploited in numerous optical applications, such as Kerr shutters [4].

The mathematical derivation of the phenomenon stems from the fact that the cube of a sinusoidal function of angular frequency ω includes a term oscillating at the same frequency ω. Raman scattering and the Kerr-effect will lead to the following simpler form of equation 4.2 [77]:

$$\mathbf{P}_{\mathrm{NL}} = \varepsilon_0 \chi^{(3)} \mathbf{E}(\mathbf{r}, t) \int_0^\infty R(t_1) \left|\mathbf{E}(\mathbf{r}, t - t_1)\right|^2 dt_1, \tag{4.4}$$

where $R(t)$ is the normalized nonlinear response function and it has been assumed that $\mathbf{P}_{\mathrm{NL}}$ and $\mathbf{E}$ point at the same directions. The lower limit of the convolution can be set to 0 instead of $-\infty$ because of the requirement of causality ($R(t) = 0$ for $t < 0$). The response function $R(t)$ includes both the instantaneous electronic response and the delayed molecular response. The delayed molecular response leads to Raman scattering, and the instantaneous part of the response function models the Kerr-effect. Instantaneous responses are modeled using the Dirac delta function $\delta(t)$, and the Kerr-effect part of the nonlinear polarization is then proportional to

$$\mathbf{E}(\mathbf{r}, t) \int_0^\infty \delta(t_1) \left|\mathbf{E}(\mathbf{r}, t - t_1)\right|^2 dt_1 = \mathbf{E}(\mathbf{r}, t) \left|\mathbf{E}(\mathbf{r}, t)\right|^2. \tag{4.5}$$

The total polarization is then given by the sum of the linear and third-order contributions, and is of the form

$$\mathbf{P} = \varepsilon_0 \mathbf{E} \left(\chi^{(1)} + C\chi^{(3)} |\mathbf{E}|^2\right) = \varepsilon_0 \chi_{\mathrm{eff}} \mathbf{E}, \tag{4.6}$$

where C is a proportionality constant, the polarization and electric fields are functions of time and space, and $\chi_{\mathrm{eff}} = \chi^{(1)} + C\chi^{(3)}|\mathbf{E}|^2$ is the *effective susceptibility*. As

the refractive index is given by $n = \sqrt{1+\chi}$, the effective refractive index is now

$$n_{\text{eff}} = \sqrt{1+\chi_{\text{eff}}} = \sqrt{1+\chi^{(1)}+C\chi^{(3)}|\mathbf{E}|^2} = \sqrt{1+\chi^{(1)}}\sqrt{1+\frac{C\chi^{(3)}|\mathbf{E}|^2}{1+\chi^{(1)}}}. \tag{4.7}$$

The nonlinear contribution to the refractive index is small compared to the linear contribution such that $C\chi^{(3)}|\mathbf{E}|^2 \ll 1+\chi^{(1)}$ [56]. Thus,

$$\frac{C\chi^{(3)}|\mathbf{E}|^2}{1+\chi^{(1)}} \ll 1, \tag{4.8}$$

and the effective refractive index is

$$n_{\text{eff}} = \sqrt{1+\chi^{(1)}}\sqrt{1+\frac{C\chi^{(3)}|\mathbf{E}|^2}{1+\chi^{(1)}}} \approx \sqrt{1+\chi^{(1)}}\left(1+\frac{C\chi^{(3)}|\mathbf{E}|^2}{2(1+\chi^{(1)})}\right). \tag{4.9}$$

Because $I \propto |\mathbf{E}|^2$, equation 4.9 can be written as

$$n_{\text{eff}} = n_1 + n_2 I, \tag{4.10}$$

where $n_1 = \sqrt{1+\chi^{(1)}}$ is the linear refractive index and n_2 is the *nonlinear refractive index*. This form for the effective refractive index clearly shows the intensity-dependence. $n_2 > 0$ for silica, so intense light experiences a larger effective refractive index [78].

4.3 Self-Phase Modulation and Cross-Phase Modulation

The dependence of monochromatic light on propagation distance z and time t can be mathematically written as $\exp(i[kz-\omega t]) = \exp(i[nk_0 z-\omega t])$. The complex phase is thus $\phi = nk_0 z - \omega t$. When n depends on the intensity, the phase of the light will consequently be affected by the light itself. This is referred to as self-phase modulation (SPM). The instantaneous (angular) frequency is $-d\phi/dt$, and in the case of linear optics this would naturally give ω. When n depends on the intensity as $n = n_1 + n_2 I$, the instantaneous frequency is

$$-\frac{d\phi}{dt} = \omega - k_0 z\frac{d(n_1+n_2 I)}{dt} = \omega - k_0 n_2 z\frac{dI}{dt}. \tag{4.11}$$

Because $n_2 > 0$, the instantaneous frequency is lower at the leading edge of a pulse (where $dI/dt > 0$) and higher at the trailing edge, as shown by figure 4.1. SPM therefore causes chirp in pulses. Note that the chirp is qualitatively similar to that caused by normal dispersion and the exact opposite of that caused by anomalous dispersion. Indeed, it turns out that the chirp caused by the Kerr-effect can precisely

cancel the anomalous dispersion induced chirp for some cases [24, 25].

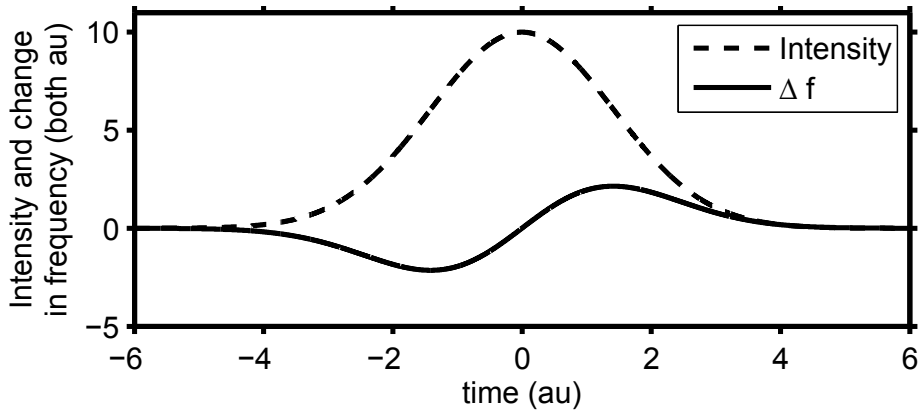

Figure 4.1: *The change in frequency due to SPM for a Gaussian pulse at a certain propagation distance. The frequency change is shown by the solid line and the intensity profile by the dashed line.*

The nature of the Kerr-effect makes no distinction whether the intensity-dependence of the refractive index experienced by light at ω_1 is caused by light at the same frequency, and it is possible for light at another frequency ω_2 to affect the phase of light at ω_1. This phenomenon is known as *cross-phase modulation* (XPM), as is also the situation where light polarized along a certain axis affects the phase of light polarized along another axis [56]. The distinction between SPM and XPM is not necessarily straightforward. A light pulse consist of multiple frequency components, and the effect of the pulse on its own phase is simply referred to as SPM. When neglecting polarization effects and deriving the nonlinear propagation equation, the difference between SPM and XPM is more evident in the frequency domain. In the time domain, SPM and XPM cause the propagation constant to become intensity-dependent.

Dispersion-induced chirp is simply due to the different propagation velocities of the frequency components, and the spectrum remains unchanged because no energy is transferred from one frequency to another. SPM and XPM, however, are accompanied by the generation of new frequency components. This is referred to as SPM- or XPM-induced spectral broadening, and it is a dominating spectral broadening mechanism in the case of short-pulse SC generation [30]. The SPM-broadened spectrum of an initially Gaussian or sech-shaped pulse develops a multipeak structure with the number of peaks depending on the initial peak power and the propagation distance [56]. Under ideal conditions an initially symmetric spectrum would remain symmetric throughout the fiber, but in reality other nonlinear phenomena, such as Raman scattering, together with dispersion and pulse asymmetry will cause one side of the spectrum to grow more intense than the other.

Although SPM induces spectral broadening on unchirped pulses, it can make the spectrum of a chirped pulse narrower. A negatively chirped pulse has higher frequencies in the leading edge and lower frequencies in the trailing edge. SPM can then counteract the initial chirp and shift the frequencies of the edges closer to the central frequency, which then results in a narrower spectrum and the pulse becoming closer to a transform-limited one. A similar scheme can be used to compress unchirped pulses in time. A transform-limited pulse cannot be compressed without broadening its spectrum, and the SPM- or XPM-induced spectral broadening offers a way compress pulses in the anomalous dispersion regime. In that regime, the blue-shifted components generated in the trailing edge and the red-shifted components at the leading edge will both move towards the pulse center because of anomalous dispersion, and the pulse will thus become shorter. Anomalous dispersion is not necessary if the dispersive effects can be compensated for at a later stage by using a prism compressor or a grating pair, for example. This technique was used as early as 1982 to generate 30 fs pulses [79], and subsequent experiments showed remarkable improvements in the following years [80].

4.4 Four-Wave Mixing

FWM (alternatively four-photon mixing) is another phenomenon related to the Kerr-effect. It describes the interaction of four photons at frequencies ω_1, ω_2, ω_3, and ω_4. Here FWM is understood to refer solely to processes where the photons at frequencies ω_1 and ω_2 are annihilated and photons at ω_3 and ω_4 are created, although some authors [56] categorize for example THG as a FWM process in which the three photons at $\omega_1 = \omega_2 = \omega_3$ are annihilated and a photon at $\omega_4 = 3\omega_1$ is created.

The energy of a photon is $\hbar\omega$, where $\hbar = h_\mathrm{P}/(2\pi)$, and conservation of energy requires that the combined energy of the annihilated photons equals the energy of the photons created, so $\omega_1 + \omega_2 = \omega_3 + \omega_4$. On the other hand, the requirement of momentum conservation transfers to an equation for the propagation constants: $\beta(\omega_1)+\beta(\omega_2) = \beta(\omega_3)+\beta(\omega_4)$, where $\beta(\omega_i)$ is the propagation constant at frequency ω_i. The momentum conservation condition $\Delta k = \beta(\omega_3)+\beta(\omega_4)-\beta(\omega_1)-\beta(\omega_2) = 0$ is the phase-matching condition for the FWM process, and it is not exactly similar to the conservation of momentum in classical mechanics since FWM also occurs when $\Delta k \neq 0$ assuming the fiber length L satisfies $L < L_\mathrm{c} = 2\pi/\Delta k$, where L_c is the so-called the coherence length. FWM is ineffective for longer fibers if the phase-mismatch is not compensated for.

The phase-matching condition is indeed very restrictive if there are four different fre-

quencies involved because the frequency-dependence of the propagation constant is usually nontrivial, and this is the reason FWM involving four different frequencies is, for the most part, ineffective in optical fibers. The process becomes less complicated for *degenerate four-wave mixing* (DFWM), which refers to the situation $\omega_1 = \omega_2$. The phase-matching condition for DFWM is then $\Delta k = \beta(\omega_3) + \beta(\omega_4) - 2\beta(\omega_1)$, which can be easily satisfied either through SPM or by virtue of λ_1, the wavelength corresponding to ω_1, being close to the ZDW [4]. Assume (without loss of generality) that $\omega_4 > \omega_3$ and denote $\Omega = \omega_4 - \omega_1 = \omega_1 - \omega_3$. When the effects of SPM and XPM are taken into account and single-mode operation is assumed, the phase-mismatch is given by [28, 56]

$$\Delta k = 2\gamma P_0 + 2\sum_{m=1}^{\infty} \frac{\beta_{2m}}{(2m)!}\Omega^{2m}, \tag{4.12}$$

where γ is the nonlinear coefficient, P_0 is the pump peak power, Ω is the angular frequency separation from the pump, and β_{2m} are the even order dispersion coefficients evaluated at the pump frequency. The phase-matching condition will be at least approximately satisfied for two frequency sidebands, and FWM provides the sidebands with an amplitude gain of $g = \sqrt{(\gamma P_0)^2 - (\Delta k/2)^2}$. Every frequency component in the sidebands will initially grow exponentially so that the initial sideband amplitude A_0^s will have grown to $A_0^s \exp(gz)$ after a propagation distance of z. Note that this is the case only in the undepleted pump approximation, because as the pump loses some of its energy to the sidebands, its power decreases affecting the gain and the location of the sidebands. Also note that the gain exist only for $g \in \mathbb{R}$. The sideband of the lower frequency is called the *Stokes wave* and that of the higher frequency is called the *anti-Stokes wave*. [28, 56]

The phase-mismatch in equation 4.12 is power-dependent because of SPM, and hence FWM can be phase-matched because of the effect of SPM. When a CW at frequency ω_0 is amplitude-modulated with a sinusoidal signal at a modulation frequency ω_m, the spectrum has, in addition to the CW peak at ω_0, two smaller peaks at $\omega_0 - \omega_m$ and $\omega_0 + \omega_m$ (just take the Fourier-transform of $[A + a\sin(\omega_m t)]\exp(-i\omega_0 t)$ to see this). The smaller peaks in the spectrum are thus symmetrically located around ω_0 with frequency separations of $\pm\omega_m$. If the phase-mismatch of equation 4.12 is approximately zero for $\Omega = \pm\omega_m$, the gain g will be real and positive at $\Omega = \pm\omega_m$, and the frequency components at $\omega_0 - \omega_m$ and $\omega_0 + \omega_m$ will be amplified upon propagation. In the temporal domain this means that the modulation contrast increases. A sinusoidal modulation of a suitable frequency will therefore initially be exponentially amplified, which is the reason why such SPM-phase-matched FWM is called *modulation instability* (MI). [56]

Equation 4.12 together with the gain profile provides the mathematical explanation why MI amplifies narrow sidebands far away from the pump frequency in the normal GVD regime and broad sidebands close to the pump frequency in the anomalous GVD regime, as shown by figure 4.2. [56]

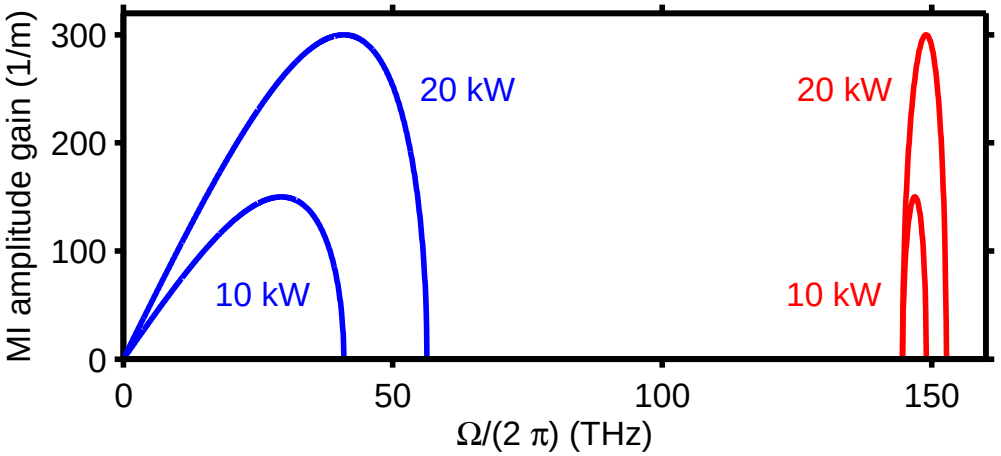

Figure 4.2: *The MI gain as a function of frequency separation from the pump frequency of 283 THz for two different peak powers. The blue curve has $|\beta_2| = 8.56$ ps^2/km while $|\beta_2| = 8.56$ ps^2/km for the red curve. The nonlinear coefficient is $\gamma = 0.015$ $(m \cdot W)^{-1}$ and the higher-order dispersion terms are $|\beta_4| = 9.29 \cdot 10^{-5}$ ps^4/km and $|\beta_6| = 9.79 \cdot 10^{-10}$ ps^6/km for both curves. The blue curve corresponds to the fiber used in this study.*

In the normal dispersion regime $\beta_2 > 0$, and both $2\gamma P_0$ and $\beta_2\Omega^2$ are positive, so the phase-matching condition cannot be satisfied for small frequency detunings. Ω has to be large enough so that the higher-order terms, such as Ω^4 and Ω^6 start to dominate the sum and can cancel the positive terms of equation 4.12. Thus, the gain sidebands will be further away from the pump frequency. When Ω is large and terms like Ω^4 dominate the sum, small variations in a large Ω lead to large changes in those dominating high-order terms, and the phase-matched frequency band will thus be narrow. The normal GVD case is shown in figure 4.2 by the red curves, and both the narrowness and the large frequency separation can be seen. Although spectrally flat supercontinua can be generated through cascaded Raman scattering by using long pump pulses in the normal dispersion regime [81, 82], anomalous pumping is more often preferred because of the (usually) desirable effect of broadband MI [83].

For small frequency detunings the dominating contribution to the sum in equation 4.12 comes from the second-order term involving β_2. The GVD parameter $\beta_2 < 0$ for anomalous dispersion, and in that case the sum can cancel the positive $2\gamma P_0$ term leading to phase-matching for small detunings Ω. When the dominating contribution to the sum comes from the second-order term, the value of the sum

depends mostly on Ω^2, so slight changes in the small Ω will not change the sum considerably, which is why the gain sidebands are broad. The anomalous GVD case is shown by the blue curves of figure 4.2. When Ω is small, the higher-order terms can be neglected, and one can readily see that the gain peaks at $\Omega = \sqrt{2\gamma P_0/|\beta_2|}$ and has a peak value of $g_{\max} = 2\gamma P_0$, as shown by figure 4.2.

The preceeding treatment assumed that the pump beam and the modulating signals are polarized along the same axis. When this is not the case, coupled equations have to be used in the mathematical treatment. Although the case of different polarizations is not considered here, it is worth mentioning that MI similar to the anomalous GVD regime can be observed for a pump frequency at the normal GVD regime, if the modulating beam is orthogonally polarized with respect to the pump beam. Such MI is referred to as *vector modulation instability*. [4]

When no initial perturbation is present, noise takes the role of the perturbation. In this case of spontaneous MI, the entire MI gain band of frequencies will be amplified. The ability of FWM to amplify noise is sometimes beneficial and sometimes undesirable. FWM can also amplify existing signals instead of noise, which is why FWM is obviously harmful in WDM systems because it might deplete signals at some channels and disturb other channels. However, the power of FWM can also be harnessed for multiple applications such as parametric oscillators, channel demultiplexing, wavelength conversion, optical sampling, and high-speed optical switching [84]. The unwanted effect of FWM on WDM systems can be drastically reduced by the clever technique of dispersion management, where the fiber consists of different segments such that each segment has a high GVD to cause high phase-mismatch, but the GVD over the whole fiber averages to zero so that the detrimental effects of GVD become minimal [4]. Usually the GVD parameter is made to flip its sign from one segment to another. Another way to reduce the effects of FWM is to use unequal channel spacings so that the energy conservation condition $\omega_1+\omega_2 = \omega_3+\omega_4$ is not easily satisfied [85].

The role of FWM and MI in SC generation become very clear in the long-pulse regime. MI causes the long pump pulse to break into a train of narrower pulses because of the amplified modulation. The forming pulses can then collide with each other, exchange energy, broaden the spectrum further, and, most evidently, significantly affect the temporal characteristics of the signal. Some of the pulses adjust themselves to become solitons, which are nonlinear pulses of certain shape. Solitons will be discussed in section 4.6.1.

4.5 Stimulated Raman Scattering

The delayed nature of molecular and atomic response to external electric fields gives rise to the already mentioned effect known as Raman scattering after its discoverer [86]. The quantum mechanical description of the phenomenon is that it describes the interaction between a photon and an optical phonon, a quantum of lattice vibration. Note that photons can just as well interact with acoustic phonons, a phenomenon known as *Brilloun scattering*, but this will not be considered here because of its negligible effect and because Brilloun scattered light actually travels backwards in fibers [56].

In Raman scattering, a photon scatters inelastically from a molecule and transfers some of its energy to it causing the molecule to rise to a higher vibrational state. The photon thus loses some of its energy and its frequency must therefore decrease by an amount corresponding to the energy transferred to the molecule. The resulting electromagnetic wave of lower frequency is called the Stokes wave like in FWM. Raman scattering is where that name originates from, and it is adopted from this context to FWM. It is also possible for the molecule to release some of its vibrational energy to a photon, which would result in an increase in the frequency of the photon. The resulting wave is the anti-Stokes wave. This kind of Raman scattering, however, is seldom observed because it requires the simultaneous presence of a photon and a phonon of suitable energies.

Figure 4.3 shows the energy states in the quantum mechanical treatment of Raman scattering. The Raman scattering process is treated quantum mechanically

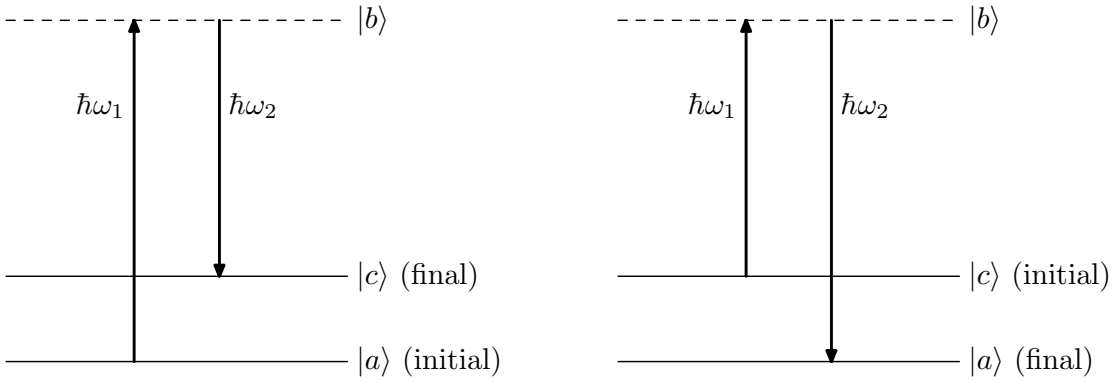

The Stokes Raman transition. The Anti-Stokes Raman transition.

Figure 4.3: *Quantum mechanical description of Raman transitions. (After ref. [87].)*

by assuming that the initial photon is absorbed, the molecule rises to a state of

higher energy and then immediately transfers back to another lower energy state by emitting a photon. The anti-Stokes wave is generated similarly with the exception that the final energy state of the molecule is actually lower than the initial one, as shown in figure 4.3.

Raman scattering can occur sponteneously, but the case of most interest in fiber optics is the so called *stimulated Raman scattering* (SRS) in which the presence of a Stokes wave seeds Raman scattering and the pump wave keeps amplifying the Stokes wave [88]. The frequencies which are amplified in the presence of a pump wave of a certain wavelength depend on the vibrational modes of the material in which the light propagates. The normalized Raman gain profile for fused silica is shown in figure 4.4, but there can be slight deviations from this in fibers due to doping and impurities. The actual unnormalized magnitude of Raman gain depends inversely on the wavelength of the pump beam.

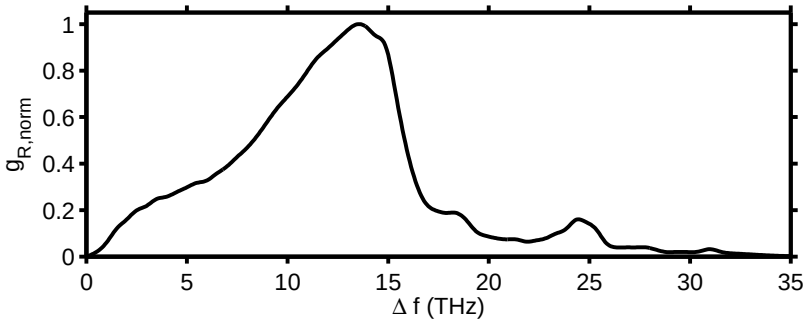

Figure 4.4: *The normalized Raman gain profile of fused silica. The maximum gain occurs for a frequency shift of approximately 13.2 THz.*

The effect of SRS is included in the mathematical model by the Raman response function $h_{\mathrm{R}}(t)$, which is the delayed part of the response function $R(t)$ mentioned in section 4.2. The function describes the time domain behavior of molecular vibrations, and the Raman gain is directly proportional to the imaginary part of the Fourier transform of $h_{\mathrm{R}}(t)$, the real part being related to the so called parametric gain, which is then related to FWM [83].

The effect of Raman gain in SC generation is clear: it transfers energy from higher frequencies to lower frequencies. This can happen for example if two pulses with a suitable wavelength separation overlap in time and the pulse with the smaller wavelength transfers some of its energy to the other pulse. Short pulses may have a spectrum broader than the Raman gain bandwidth, and in that case the pulse transfers some of its own energy to lower frequencies upon propagation. This leads to red-shift of the pulse, and in the case of solitons this kind of intrapulse Raman scattering is known as soliton self-frequency shift (SSFS) [26]. The frequency shift

per unit distance is inversely proportional to the fourth power of the duration of the soliton, which means that the red-shift can become very large for short solitons [56].

4.6 Nonlinear Propagation Equation

The derivation of the propagation equation is mathematically somewhat cumbersome, and a good presentation of this is given in Agrawal's book [56], but it is helpful to state the main assumptions and simplifications made during the derivation of the propagation equation. First, polarization effects are neglected and the electric field and the induced polarization are assumed to be parallel. Second, Brilloun scattering is neglected. Third, single-mode propagation is assumed. Note that this is not a numerical approximation since the fibers can be made to support one mode only. Fourth, only relevant third-order nonlinear effects are taken into account. THG is neglected because of phase-mismatch, second-order effects are neglected because of centrosymmetry, and higher-order effects are neglected because of their minuscle contribution. Fifth, the nonlinearity is taken into account by using first-order perturbation theory, which means that the nonlinearity only affects the propagation constant β and not for example the modal distribution $F(x, y)$. The effect of the nonlinearity on the effective refractive index is thus justifiably assumed small. Sixth, the weak frequency-dependence of the nonlinearity is taken into account through a linear approximation. Seventh, the electric field in the frequency domain centered around the frequency ω_0 is of the form $\tilde{E}(\mathbf{r}, \omega-\omega_0) = \tilde{A}(z, \omega-\omega_0)F(x, y)\exp(i\beta_0 z)$, where $\tilde{A}$ is a slowly-varying function of z such that we can approximate

$$\frac{\partial^2 \tilde{E}}{\partial z^2} = F(x,y)\exp(i\beta_0 z)\left(\frac{\partial^2 \tilde{A}}{\partial z^2} + 2i\beta_0\frac{\partial \tilde{A}}{\partial z} - \beta_0^2\tilde{A}\right) \tag{4.13}$$

$$\approx F(x,y)\exp(i\beta_0 z)\left(2i\beta_0\frac{\partial \tilde{A}}{\partial z} - \beta_0^2\tilde{A}\right). \tag{4.14}$$

This approximation is called the *slowly-varying envelope approximation* and is valid for pulses as short as tens of femtoseconds [56].

Under the aforementioned assumptions and using the reatarded time coordinate $T = t - \beta_1 z$, equation 3.10 can be shown to lead to the following equation for the

amplitude $A(z,T)$:

$$\frac{\partial A}{\partial z} + \frac{\alpha}{2}A - \sum_{k\geq 2} \frac{i^{k+1}}{k!}\beta_k \frac{\partial^k A}{\partial T^k}$$
$$= i\gamma \left(1 + i\tau_{\text{shock}} \frac{\partial}{\partial T}\right) \left(A \int_{-\infty}^{\infty} R(T')|A(z, T-T')|^2 dT' + i\Gamma_{\text{R}}(z,T)\right). \quad (4.15)$$

The left hand side models the dispersive effects (β_k) and possible losses (α) and the right hand side contains the effects of optical nonlinearities. γ is the nonlinear parameter and $R(T)$ is the response function that includes both the instantaneous electronic contribution and the delayed molecular response. It is customary to use the experimentally determined Raman profile [89], which is essentially the Fourier trasform of the Raman response function, a transfer function. The frequency-dependence of the nonlinearity is taken into account with τ_{shock}. Γ_{R} models the spontaneous quantum noise associated with the Raman effect and could as well be neglected. The nonlinear parameter is

$$\gamma = \frac{3\omega_0 \Re(\chi^{(3)}(\omega_0))}{8cn(\omega_0)A_{\text{eff}}(\omega_0)}, \quad (4.16)$$

where A_{eff} is the effective mode area defined as

$$A_{\text{eff}} = \frac{\left(\int\int_{-\infty}^{\infty} |F(x,y)|^2 \, dxdy\right)^2}{\int\int_{-\infty}^{\infty} |F(x,y)|^4 \, dxdy}. \quad (4.17)$$

If the modal distribution is approximated by a Gaussian function as in equation 3.20, the effective mode area is simply $A_{\text{eff}} = \pi w^2$.

Equation 4.15 is called *the Generalized nonlinear Schrödinger equation* (GNLSE) and it has been shown to accurately model nonlinear broadband pulse propagation in PCF [28] and will be used in this study. The scalar equation is valid if fiber birefringence can be neglected or if one assumes that the electric field is polarized along one of the principal axes of the fiber. Unless special care is taken, fibers are birefringent in practice both because of the material used and because of random variations in the fiber core shape. However, the fiber used in the study is highly nonlinear such that shorter fiber lengths can be used to observe nonlinear phenomena, and polarization effects can be neglected simply by virtue of the small length of the fiber [56].

4.6.1 Solitons and Other Analytical Solutions of the GNLSE

The GNLSE can only be solved analytically in some restrictive specific cases, such as when it can be reduced to the NLSE [58]. Because the NLSE keeps showing up in various different contexts besides nonlinear optics, such as Bose-Einstein condensates and water waves, a great deal of effort has been put into developing methods to obtain analytical solutions of the equation. The inverse scattering transform is likely the most well known method [90], but exact solutions can also be obtained for example by using Hirota's method [91], the truncated Painlevé expansion method [92], the tanh-method [93], and the more recent generally projective Riccati equation method, which is capable of constructing a multitude of families of solutions [94]. Although the NLSE does not always accurately describe broadband pulse propagation, its analytical solutions do exist in nature.

Solitons are arguably the most important class of exact solutions of the NLSE. Although the word "soliton" appears in the names of many analytical solutions of the NLSE, it is customary that "soliton" refers to a solution in the anomalous dispersion regime that corresponds to a temporal intensity profile of the form $N^2\text{sech}^2(T/T_0)$ at some point during propagation, and in purely mathematical treatments this point is usually set to be the beginning of the fiber ($z = 0$). T_0 is the duration of the soliton, and the integer N is called the order of the soliton, and it is related to the duration and the peak power of the soliton and to the fiber parameters as

$$N = \sqrt{\frac{\gamma P_0 T_0^2}{|\beta_2|}}. \tag{4.18}$$

First-order solitons (also called fundamental solitons) are highly important in nonlinear fiber optics for several reasons. They do not change their shape upon propagation and are robust to noise and variations in fiber parameters, and they can survive collisions and interactions with other waves and solitons. They are robust to the extent that any pulse with a reasonable form will actually evolve into a fundamental soliton. They are also stable in the presence of losses though they will, by definition, lose some of their energy upon propagation. The peak power of the fundamental soliton is inversely proportional to the square of the duration of the soliton, so if a fundamental soliton experiences losses, its duration must increase. Nevertheless, solitons tend to remain solitons, which is what explains their great importance in fiber-optic communication systems [4]. The fact that the first documented experimental observation [95] of a fundamental soliton was for a water wave in a Scottish canal in 1834 makes it fascinating that the same phenomenon is exploited in cutting-edge optical communication systems of the 21$^{\text{st}}$ century.

The importance of solitons from the perspective of SC generation arises mainly from two reasons: Raman-induced SSFS and dispersive wave (DW) emission. Dispersive wave emission is also called dispersive radiation, soliton radiation, and optical Cherenkov radiation, and it means the process in which a pulse emits a blue-shifted dispersive wave in the normal dispersion regime while adjusting itself to become a soliton. The emission of dispersive waves then contributes to the spectral broadening to the blue side, while SSFS cause spectral broadening to the red side.

Whereas the fundamental soliton does not change its spectrum or temporal intensity profile upon propagation, higher-order solitons do so in a periodic manner. However, higher-order solitons are highly unstable in the presence of Raman-scattering and optical shock effects, and even the inclusion of third-order dispersion can, depending on its magnitude, cause an N^{th} order soliton to break into N fundamental solitons [56]. This is called *soliton fission*. Thus, no periodic evolution is observed unless the propagation is described by the NLSE with only second-order dispersion and Kerr-effect taken into account. Even in that case, solitons of sufficiently high orders tend to undergo soliton fission and break down to their constituents due to noisy input conditions. Solitons of lower orders are relatively noise-insensitive, and no soliton fission is observed for short propagation distances. Figure 4.5 shows the evolution of a second-order soliton in the GNLSE and NLSE cases. The NLSE would predict incorrect behavior of the system and the respective figure shows periodic evolution.

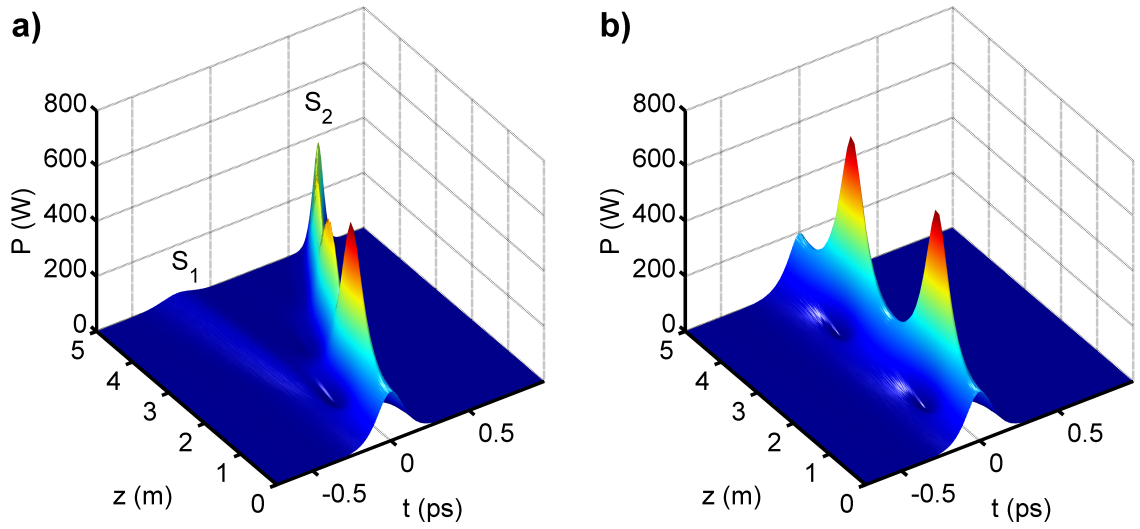

Figure 4.5: *The evolution of a second-order soliton with slight input noise simulated using a) the GNSLE and b) the NLSE. The NLSE predicts incorrect, seemingly periodic behavior. In reality the pulse would break into two solitons as shown in a). The solitons are labeled S_1 and S_2.*

In certain cases (i.e. for long pulses that are not too intense) the GNLSE can be reduced to the simpler NLSE equation while retaining the ability to accurately model the physics of pulse propagation [56]. Indeed, solitons of second and third orders were observed in the same experiment that was at the same time the first demonstration of the fundamental soliton [25]. Thus, even higher-order solitons are not mere mathematical curiosities but real phenomena that can occur in optical fibers. Other types of more exotic analytical solutions of the NLSE have also been observed experimentally, with recent examples given by Akhmediev breathers [96], the Peregrine soliton [97], and the Kuznetsov-Ma soliton [98].

4.6.2 Solving the GNLSE Numerically

The GNLSE admits no general analytical solutions, and numerical methods to solve the equation have to be used instead. Equation 4.15 can be solved numerically by various finite difference and Runge-Kutta methods, but to this day the *split-step Fourier method* (SSFM) remains as one of the most sophisticated ones [56]. The Runge-Kutta procedure can also be implemented in this method for improved accuracy, but usually reducing the step size does the same in terms of increased accuracy and computational time.

The starting point for the SSFS is to write the GNLSE in the following operator form:

$$\frac{\partial A}{\partial z} = \left(\hat{D} + \hat{N}\right) A, \tag{4.19}$$

where

$$\hat{D} = -\frac{\alpha}{2} + \sum_{k\geq 2} \frac{i^{k+1}}{k!} \beta_k \frac{\partial^k}{\partial T^k} \tag{4.20}$$

is a differential operator accounting for losses and dispersion, and $\hat{N}$ is a nonlinear operator accounting for fiber nonlinearities and the effect of which on A is defined by [56, 28]

$$\hat{N}A = i\gamma \left(1 + i\tau_{\text{shock}} \frac{\partial}{\partial T}\right) \left(A \int_{-\infty}^{\infty} R(T')|A(z, T-T')|^2 dT' + i\Gamma_{\text{R}}(z,T)\right). \tag{4.21}$$

Note that the operator $\hat{N}$ is z- and A-dependent while $\hat{D}$ is not, and one could write $\hat{N} = \hat{N}(z)$ for clarity.

The SSFM is practically a finite difference method with respect to the spatial variable z, and one is eventually interested in calculating the value $A(z+h, T)$ when $A(z, T)$ is known. The formal exact solution of equation 4.19 for $A(z+h, T)$ is given

by

$$A(z+h,T) = \exp\left(\int_{z}^{z+h}\left(\hat{D}+\hat{N}(z')\right)dz'\right)A(z,T). \tag{4.22}$$

The integral of $\hat{D}$ is trivially $h\hat{D}$, but the integral of $\hat{N}$ is more tricky because of its dependence on z and unknown values of A between the interval $[z, z+h]$. The obvious way to deal with this is to make the step size h small enough such that A is approximately constant in the interval $[z, z+h]$ and the integral can thus be approximated by the known value $h\hat{N}(z)$. A more sophisticated approach first exploits this approximation to calculate $A(z+h,T)$ and then uses this approximate value and the trapezoidal rule to approximate the value of the integral. The iteration can then be continued to obtain better approximations for $A(z+h,T)$. Using the iterative trapezoidal procedure can reduce the computational time, but for simplicity it is not used in this treatment, and we simply approximate

$$A(z+h,T) \approx \exp\left(h\left(\hat{D}+\hat{N}\right)\right)A(z,T). \tag{4.23}$$

For computational purposes, a further approximation of the exponential $\exp\left(h\left(\hat{D}+\hat{N}\right)\right)$ is needed. It relies on the Baker-Hausdorff formula for two non-commutating operators $\hat{a}$ and $\hat{b}$ [99]:

$$\exp(\hat{a})\exp(\hat{b}) = \exp\left(\hat{a}+\hat{b}+\frac{1}{2}[\hat{a},\hat{b}]+\frac{1}{12}[\hat{a}-\hat{b},[\hat{a},\hat{b}]]+\ldots\right), \tag{4.24}$$

where $[\hat{a},\hat{b}] = \hat{a}\hat{b}-\hat{b}\hat{a}$ is the commutator. Now using $\hat{a} = h\hat{D}$ and $\hat{b} = h\hat{N}$ we see that the dominating error term in the approximation

$$\exp\left(h\left(\hat{D}+\hat{N}\right)\right) \approx \exp\left(h\hat{D}\right)\exp\left(h\hat{N}\right) \tag{4.25}$$

arises from the commutator $[h\hat{D}, h\hat{N}]$ and is thus proportional to h^2. By applying the B-H formula twice one can verify (after some algebra) that an even better approximation is given by

$$\exp\left(h\left(\hat{D}+\hat{N}\right)\right) \approx \exp\left(\frac{h}{2}\hat{D}\right)\exp\left(h\hat{N}\right)\exp\left(\frac{h}{2}\hat{D}\right), \tag{4.26}$$

because then the dominant error term is proportional to h^3. The SSFM using equation 4.26 is sometimes called the symmetrized SSFM due to the symmetrical nature of the right hand side of the equation. The difference between the ordinary SSFM and the symmetrized one is that in the ordinary version nonlinear effects are taken into account between fiber segments of length h and in the symmetrized version the

same is done in the middle of each segment. [56]

Equation 4.21 gives $\hat{N}A$, but for computational purposes $\hat{N}$ can be solved easily by reorganizing the terms in equation 4.21 and using basic algebra. The convolution and the time-derivative in the resulting expression are easiest to calculate in the frequency domain and everything else is suitably done in the time domain. The operator $\exp\left(\frac{h}{2}\hat{D}\right)$ is also trivial to calculate in the frequency domain where it is a mere complex number. The Matlab implementation of the symmetrized SSFM is then relatively fast due to Matlab's excellent suitability for matrix and vector operations and its highly optimized fast Fourier transform (FFT) algorithm[2].

[2]see www.fftw.org for more information on the algorithm developed by Matteo Frigo and Steven G. Johnson.

5. SUPERCONTINUUM

The GNLSE-governed evolution of pulses allows for extreme spectral broadening because new frequency components are generated through different nonlinear processes. Although spectral broadening of Raman emission lines in liquids was discovered as early as 1964 by Jones and Stoicheff [100], the discovery of supercontinuum is usually credited to Alfano and Shapiro as they were the first ones to report supercontinuum generation in bulk glass in 1970 [5, 6]. The spectrum obtained in their experiments was ten times wider than anything previously reported, but in their studies they neither focused on the broad spectrum nor called it a supercontinuum [28].

Since the 1970's, SC generation has been studied extensively and it has found numerous applications in spectroscopy, pulse compression, optical communications, frequency metrology, and tunable ultrafast laser sources, to name a few [28]. In the early days supercontinuum was used to study vision, photosynthesis and dynamics of chemical reactions [9]. Supercontinuum generation benefited greatly from the invention of PCFs, and this was reflected by the numerous new applications made possible by PCFs.

5.1 Supercontinuum Dynamics

Supercontinuum generation in fibers can be roughly divided in two regimes: the long pulse regime and the short pulse regime, where the long pulse regime is understood to cover CW SC generation [83]. In the anomalous dispersion regime the corresponding evolution dynamics are initially dominated by soliton fission for short pulses and MI for longer pulses. Soliton fission refers to the breakup of an N^{th} order soliton into N (or sometimes less) fundamental solitons and the effect of MI is to break a longer pulse into a train of pulses that evolve into solitons. Therefore, soliton dynamics play an important role in both regimes because the generated fundamental solitons experience subsequent rich dynamics and contribute significantly to the spectral broadening, envelope, and coherence properties in both temporal and spectral domains.

5.1.1 Short-Pulse Regime

The short-pulse regime covers the situations where the input pulse duration is of the order of tens to hundreds of femtoseconds [28]. The actual distinction between the short- and long-pulse regimes depends also on fiber and laser parameters. When the input pulse spectrum lies mostly in the normal dispersion regime, the initial spectral broadening in the short-pulse regime is caused by SPM. In the anomalous dispersion regime the initial pulse corresponds to a higher-order soliton, and were it only for GVD and SPM, the pulse would evolve in a periodic manner. However, the perturbations in the form of shock effects, higher-order dispersion, and Raman scattering will cause the N^{th} order soliton to undergo soliton fission and break into fundamental solitons, the amount of which is less than or equal to N (see figure 5.1). In general, the amount of fundamental solitons created will only be equal to N if N is sufficiently small. Otherwise some of the energy of the initial pulse will be transferred to dispersive waves, and the more energy the dispersive waves get, the less there is left for solitons, and consequently fewer fundamental solitons will be formed. Figure 5.1 shows the temporal and spectral evolution of a 200 fs sech-pulse

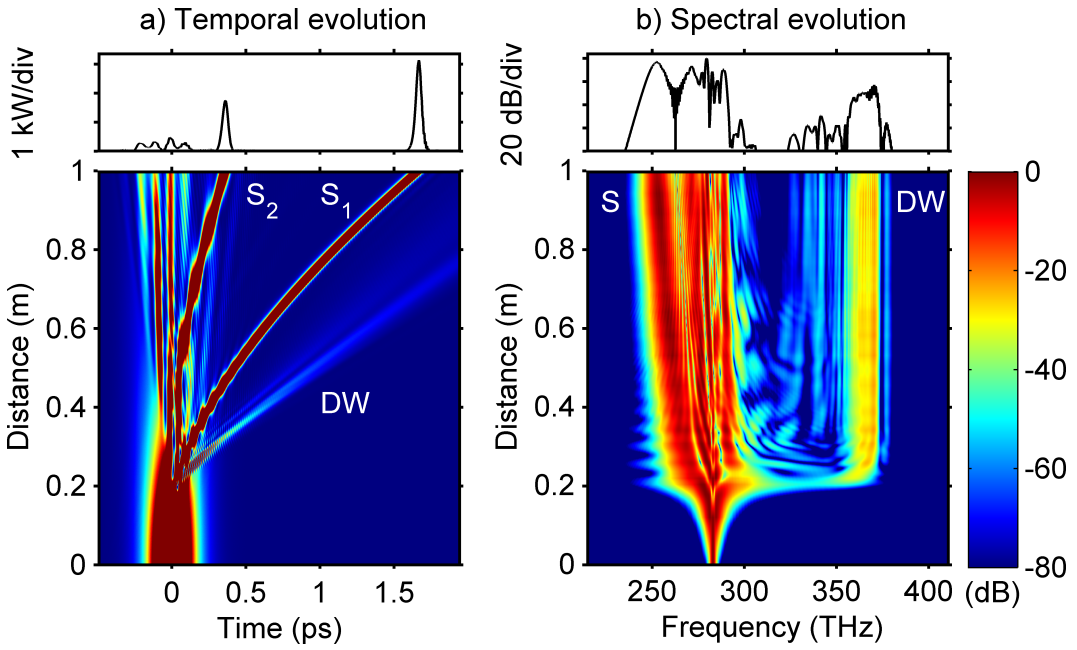

Figure 5.1: *Temporal and spectral evolution of a 200 fs, 1.6 kW sech-pulse in the fiber used in this study ($\gamma = 0.015\ (m \cdot W)^{-1}$ and the dispersion coefficients are listed in table 6.1). The left figures are on linear scale and the color axis has been cut at 500 W for clarity. The spectral evolution is plotted using a logarithmic color scale. The two brightest solitons have been labeled S_1 and S_2 in the temporal trace. The soliton and DW parts of the spectral trace have been labeled by S and DW, respectively.*

of 1.6 kW peak power. The soliton order is approximately 6.0077. Note that most of the energy has been transferred to the two brightest solitons S_1 and S_2 after 70

centimeters of propagation. Four smaller peaks are clearly visible, but their solitonic nature is not as obvious. Besides soliton fission, also other relevant phenomena can be seen in figure 5.1.

One of the most notable features is that the two most powerful solitons, especially the most intense one labeled S_1, have curved trajectories in the time domain. This means that upon propagation, the solitons start decelerating lagging more and more behind. It is caused by the combined effects of anomalous dispersion mentioned in section 3.4.1 and intrapulse Raman scattering in the form of SSFS mentioned in section 4.5. The brighter solitons have longer wavelengths than other remains of the initial pulse, which is why anomalous dispersion causes them to lag behind in the first place. SSFS causes the solitons to red-shift more, which in turn causes the solitons to decelerate. Hence the curved trajectory. Because solitons of higher peak power must have shorter durations and the rate of the SSFS is inversely proportional to the fourth power of the duration, higher peak power means more red-shift and more lag. The red-shift of the highest soliton can also be seen in the spectral trace of figure 5.1.

Another feature that can be seen in both spectral and temporal traces is the emission of dispersive waves. The DW generated right after 20 cm of propagation is clearly visible, and the spectral trace shows it around 365 THz. It can be seen that the DW lags behind the most intense soliton although it should, according to the chromatic dispersion profile, move faster than the soliton. This is known as *soliton trapping*, and it can also occur for pairs of solitons, as was the case in the first experimental observation of the phenomenon [101]. The explanation is that the intense soliton causes the DW to experience a higher refractive index due to XPM (see section 4.3), and it cannot move past the soliton. Because the DW and the soliton overlap temporally and propagate at similar velocities, they can interact and exchange energy with each other. Indeed, it has been shown [102, 103] that XPM and FWM can cause the DW to blue-shift and that the soliton experiences red-shift that is greater than what can be explained by the SSFS alone [104]. This cross-talk between a soliton and a DW can contribute significantly to the spectral broadening, and the usage of tapered fibers can enhance it even further [105].

5.1.2 Long-Pulse Regime

The long-pulse regime refers to SC generation using pico- and nanosecond input pulses and CW lasers. Both in the anomalous and the normal dispersion regimes the initially dominating nonlinear process is FWM (see section 4.4). The pump beam provides amplification for those sidebands that satisfy the phase-matching condition to a certain degree.

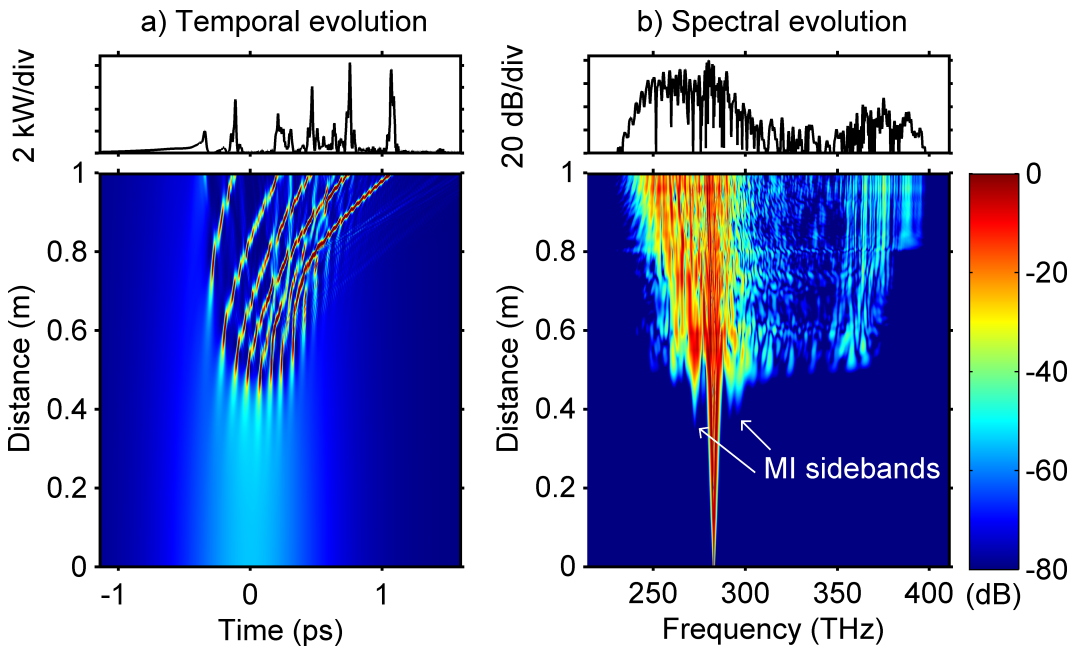

Figure 5.2: *Temporal and spectral evolution of a 1 ps, 1.6 kW pulse. The left figures are on linear scale and the color axis has been cut at 5 kW for clarity. The spectral evolution is plotted using a logarithmic scale.*

Figure 5.2 shows the evolution of a SC generated using a picosecond input pulse, the central frequency of which lies in the anomalous GVD regime. The peak power is similar to the short pulse case shown in figure 5.1, so the picosecond pulse has five times more energy than the 200 fs pulse. Yet the spectral broadening starts at a later stage (around 45 cm) and builds up slower than in the short pulse case, and the spectrum at the fiber output is also flatter and broader.

The effect of MI can be clearly seen in both the temporal and spectral traces of figure 5.2. The first-order sidebands become visible after 40 cm of propagation and the higher-order sidebands after 50 centimeters. The time domain manifestation of these sidebands can be seen as the sinusoidal modulation of the pulse. The modulation deepends with the formation of additional sidebands and a train of pulses is formed. The pulses then start experiencing intrapulse Raman scattering and can form solitons, the curved trajectories of which can be seen in the temporal trace. After 60 centimeters of propagation, soliton dynamics start to play an increasingly important role in the evolution.

Because the initially dominating process for long-pulse regime SC generation is MI and the sidebands grow from noise, long-pulse regime SC could be expected to be highly sensitive to the initial noise. If the simulation shown in figure 5.2 were to be done using a different seed for the randomly generated input noise, the temporal

and spectral traces could look very different. It is very difficult to tell the exact effect of noise on the spectrum and the temporal intensity profile based on a single simulation, and the effect of initial noise is not at all obvious in the short pulse case either. In order to characterize the fluctuations from one realization to another, multiple shots have to be simulated and studied. The actual comparison of these fluctuations, on the other hand, requires mathematics, and we have to "measure what we are speaking about, and express it in numbers"[1].

5.2 Supercontinuum Coherence

Although supercontinuum initially attracted attention because of the broad spectrum, the coherence properties of supercontinuum light are of utmost importance in terms of its applications [28, 33]. The broadness of the spectrum is more important for some applications, such as white-light interferometry or optical coherence tomography, but high coherence is required for frequency metrology and coherent spectroscopy [106].

The shot-to-shot fluctuations in supercontinua generated by seemingly identical initial pulses have their origin in the initial noise. Modern lasers are capable of producing high-quality pulses with only slight variations from pulse to pulse, which can be verified using several accurate measurement techniques such as frequency-resolved optical gating (FROG) [107]. Even the highest-quality pulses are noisy simply because they consist of a discrete number of photons at certain frequencies, and the frequency spectrum of a laser pulse is discrete, although the frequencies are closely spaced. The discrete spectrum is due to the fact that the laser pulse can only contain frequency components corresponding to the longitudinal standing wave modes of the laser cavity. The ultimate noise limit is given by *quantum shot noise*, which is due to spontaneously emitted photons at the laser mode frequencies. As the name indicates, the derivation of a mathematical model for quantum shot noise requires a quantum mechanical treatment, but it turns out that the noise can be modeled by introducing a single photon with a random phase for each laser mode. This fundamental noise limit must be incorporated in the numerical model. Quantum shot noise is what ultimately determines the random noise for each pulse and what makes coherence and correlation studies meaningful.

In order to assign a numerical measure to the spectral degree of shot-to-shot co-

[1] William Thomson, First Baron Kelvin, 1824-1907.

herence, Dudley and Coen defined the complex spectral coherence function

$$g_{12}^{(1)}(\omega) = \frac{\left\langle \tilde{E}_i^*(\omega)\tilde{E}_j(\omega)\right\rangle_{i\neq j}}{\left\langle \left|\tilde{E}(\omega)\right|^2\right\rangle}, \tag{5.1}$$

where the angle brackets denote averaging over an ensemble of realizations [29]. $g_{12}^{(1)}(\omega)$ describes the degree of correlation at a single frequency between multiple SC pulses. Dudley and Coen also define the overall degree of spectral coherence as

$$|g_{12}^{(1)}| = \frac{\int_0^\infty |g_{12}^{(1)}(\omega)|S(\omega)d\omega}{\int_0^\infty S(\omega)d\omega}, \tag{5.2}$$

and the extreme values 0 and 1 then mean complete incoherence and complete coherence, respectively. Similar functions can be defined for temporal coherence by replacing every ω by t.

Genty et al. [33, 106] wanted to draw a more direct analogy between standard correlations of nonstationary light and supercontinuum coherence and used the typical normalized second-order correlation functions [108, 109]. In the temporal domain, the function is known as the *mutual coherence function* (MCF) and is defined as

$$\Gamma_{\mathrm{E}}(t_1, t_2) = \langle E^*(t_1)E(t_2)\rangle\,. \tag{5.3}$$

The normalized form is

$$\gamma_{\mathrm{E}}(t_1, t_2) = \frac{\Gamma_{\mathrm{E}}(t_1, t_2)}{\sqrt{\langle I(t_1)\rangle\langle I(t_2)\rangle}}. \tag{5.4}$$

In the frequency domain, the function corresponding to $\Gamma_{\mathrm{E}}(t_1, t_2)$ is known as the *cross-spectral density* (CSD), it is denoted by $W_{\mathrm{E}}(f_1, f_2)$, and it is similar to the CSD used in control theory [110]. The normalized form of the CSD is denoted by $\mu_{\mathrm{E}}(f_1, f_2)$. The study showed that in the long- and short-pulse regimes the correlations in both temporal and frequency domains consist of what they termed a *quasi-coherent square* and a *quasi-stationary line* [106]. In a subsequent study Genty et al. [33] are able to show that the Dudley-Coen coherence function is actually directly related to the coherent part of the CSD but not at all to the quasi-stationary part.

All these measures of coherence deal with correlations of the electric field, but a

straightforward generalization of the normalized MCF to intensities is given by [109]

$$\gamma_{\mathrm{I}}(t_1, t_2) = \frac{\langle I(t_1) I(t_2) \rangle}{\langle I(t_1) \rangle \langle I(t_2) \rangle}. \tag{5.5}$$

The CSD for intensities W_{I} and its normalized form μ_{I} are defined in a similar way but in the frequency domain. Note that the values of the normalized intensity MCF and CSD are not bounded above by unity unlike for the field MCF and CSD.

5.3 Intensity Correlations

In the analysis of coherence and correlations, another weapon of choice will be the ordinary Pearson correlation coefficient, which varies between -1 and 1 and gives direct insight into the statistics of intensity fluctuations in supercontinuum generation. The correlation functions will be denoted by $\rho_{\mathrm{f}}(f_1, f_2)$ and $\rho_{\mathrm{t}}(t_1, t_2)$ and they are defined by

$$\rho_{\mathrm{f}}(f_1, f_2) = \frac{\langle I(f_1) I(f_2) \rangle - \langle I(f_1) \rangle \langle I(f_2) \rangle}{\sqrt{\left(\langle I^2(f_1) \rangle - \langle I(f_1) \rangle^2 \right) \left(\langle I^2(f_2) \rangle - \langle I(f_2) \rangle^2 \right)}} \tag{5.6}$$

and similarly in the time domain with t_1 and t_2 instead of f_1 and f_2. The value -1 means perfect anticorrelation, 1 perfect correlation, and 0 no correlation at all.

6. NUMERICAL SIMULATIONS

The correlation and coherence properties of supercontinua are studied by simulating ensembles of supercontinua with varying input conditions. An ensemble consists of a thousand simulations each with different initial noise so that reliable conclusions can be drawn about the statistical behavior of the system for varying input pulse characteristics. The short-pulse regime is studied by using 200 fs input pulses and the long-pulse regime by using 1 ps pulses. The input pulses are assumed to be transform-limited and sech-shaped, which is a typical pulse shape for mode-locked lasers capable of producing pulses of femtosecond duration [111]. The central wavelength of the pulses is 1.06 μm, so the pulses correspond to realistic pulses produced by passively mode-locked Ti:sapphire or Nd:glass lasers.

The fiber used in this study is similar to the one used in reference [33] in terms of the dispersion coefficients β_i but has a nonlinear coefficient of $\gamma = 0.015\ (\mathrm{m} \cdot \mathrm{W})^{-1}$ as opposed to $0.01\ (\mathrm{m} \cdot \mathrm{W})^{-1}$. Unless specified otherwise, dispersion up to the tenth order is taken into account. The dispersion coefficients are listed in table 6.1. The

Table 6.1: *Dispersion coefficients of the fiber up to tenth order.*

Dispersion coefficients	
β_2	$-8.56\ \mathrm{ps}^2/\mathrm{km}$
β_3	$6.87 \cdot 10^{-2}\ \mathrm{ps}^3/\mathrm{km}$
β_4	$-9.29 \cdot 10^{-5}\ \mathrm{ps}^4/\mathrm{km}$
β_5	$2.45 \cdot 10^{-7}\ \mathrm{ps}^5/\mathrm{km}$
β_6	$-9.79 \cdot 10^{-10}\ \mathrm{ps}^6/\mathrm{km}$
β_7	$-3.95 \cdot 10^{-12}\ \mathrm{ps}^7/\mathrm{km}$
β_8	$-1.12 \cdot 10^{-14}\ \mathrm{ps}^8/\mathrm{km}$
β_9	$1.06 \cdot 10^{-15}\ \mathrm{ps}^9/\mathrm{km}$
β_{10}	$-1.51 \cdot 10^{-20}\ \mathrm{ps}^{10}/\mathrm{km}$

fiber supports only the fundamental mode for the broad frequency range of the generated supercontinua, so the single-mode operation assumption is justified.

6.1 Correlations in the Short-Pulse Regime

The evolution of short pulses depends on the input peak power because it determines the magnitude and length scale of the nonlinear effects and the input soliton order. Therefore various different peak powers ranging from 1 kW to 30 kW were used in this study. The evolution of a more intense pulse over shorter length scales bears remarkable similarities to the evolution of a weaker pulse over longer propagation distances. It is therefore insightful to analyze an ensemble of simulations with a sufficiently high input peak power in more detail. The 20 kW ensemble has been chosen here because it allows for both a detailed analysis of initial pulse evolution and rich output characteristics.

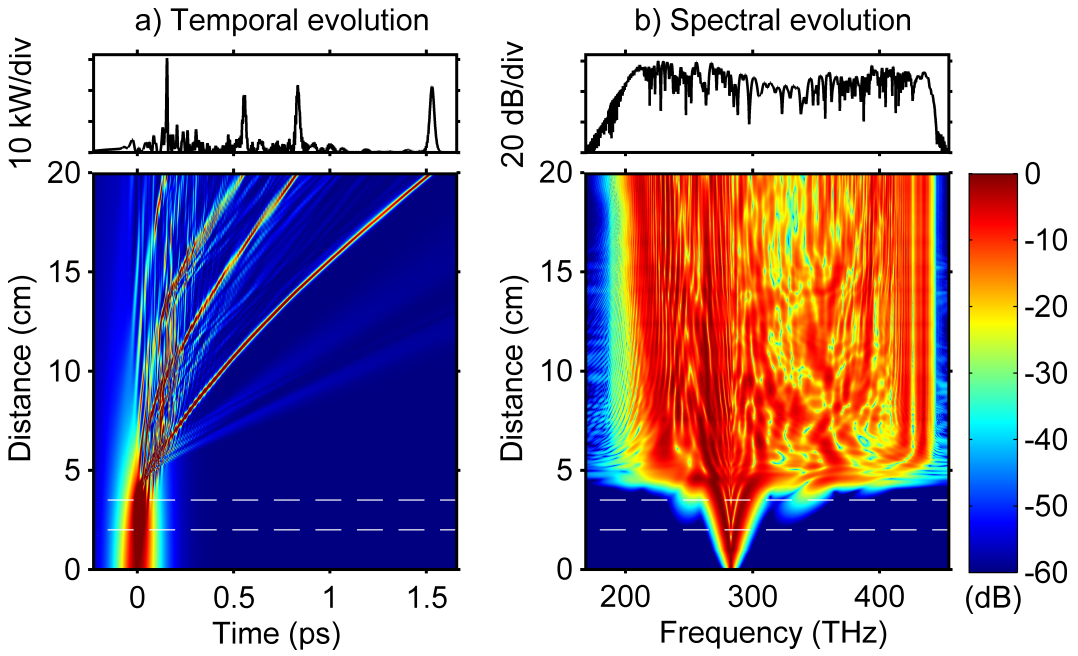

Figure 6.1: *The temporal and spectral evolution of a 200 fs, 20 kW pulse. The color axis for the temporal trace has been cut at 20 kW to improve visibility. The normalized spectral trace is plotted using a logarithmic scale from –60 dB to 0 dB. The horizontal white dashed lines have been added to indicate propagation distances of interest. The upper line at 3.5 cm is at the approximate location of maximum pulse compression.*

The temporal and spectral evolution of a single 200 fs, 20 kW pulse is shown in figure 6.1. The corresponding soliton order is $N = 21.24$. Note how the normalized spectrum remains seemingly unchanged after 6 cm of propagation except for some SSFS, but the temporal intensity profile starts to change drastically around 6 cm. This is due to formation of robust solitons that remain virtually unchanged if they do not collide with other solitons of approximately same central frequency. At least four solitons can be clearly seen in the output temporal intensity profile. The highest output peak power is more than 30 kW because of interference between a

soliton and dispersive waves and smaller pulses. The initial spectral broadening is evidently dominated by SPM because the spectrum develops the typical multipeak structure, as shown by the bright red V-shaped patterns in the spectral trace from 0 cm to 4 cm.

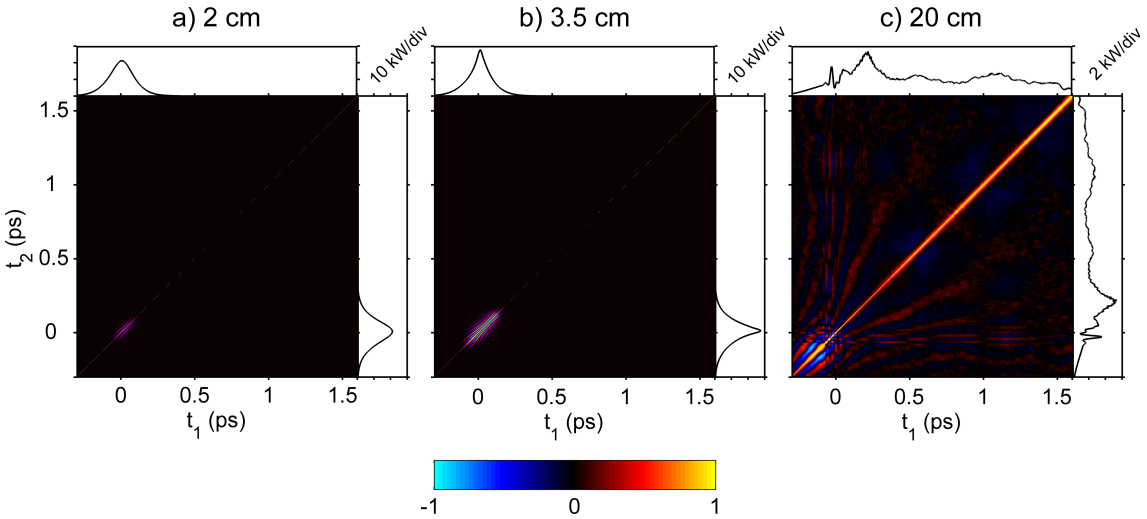

Figure 6.2: *The temporal correlation function $\rho_t(t_1, t_2)$ and intensity profiles of 200 fs 20 kW input pulses after specified propagation distances. The temporal axes show the retarded times (i.e. the time differences from the pulse center).*

The initial evolution of the 200 fs, 20 kW pulse seems to be deterministic and independent of the initial noise, although no reliable conclusions can be drawn without correlation calculations. Figure 6.2 shows the temporal correlations for the 200 fs, 20 kW ensemble at the propagation distances specified in the figure. Initial pulse compression and signs of a sinusoidal pattern can be seen. Besides the diagonal lines of unity correlation, the pattern of sinusoidally alternating regions of correlation and anticorrelation in subfigures a) and b), and the correlation-anticorrelation pattern of the leading edge of the input pulse at the lower left corner of subfigure c), practically no structure can be seen. The output correlations shown in c) do display a few faint orange lines, but the correlations are very weak.

The spectral correlation functions shown in figure 6.3 display more structure and details than the temporal correlations. The correlations at 2 cm show a thick and strong correlated diagonal line with alternating curved regions of anticorrelation and correlation besides it. The mean spectrum has a clear dip at the pulse central frequency. At 3.5 cm the mean spectrum has developed asymmetric sidelobes and has more dips near the center. The correlation pattern shows a blue cross with red lines at the deepest dips of the mean spectrum. The sidelobes are fully correlated with themselves and with each other and form bright red regions close to the corners. At the fiber output the mean spectrum is very flat and everything is uncorrelated

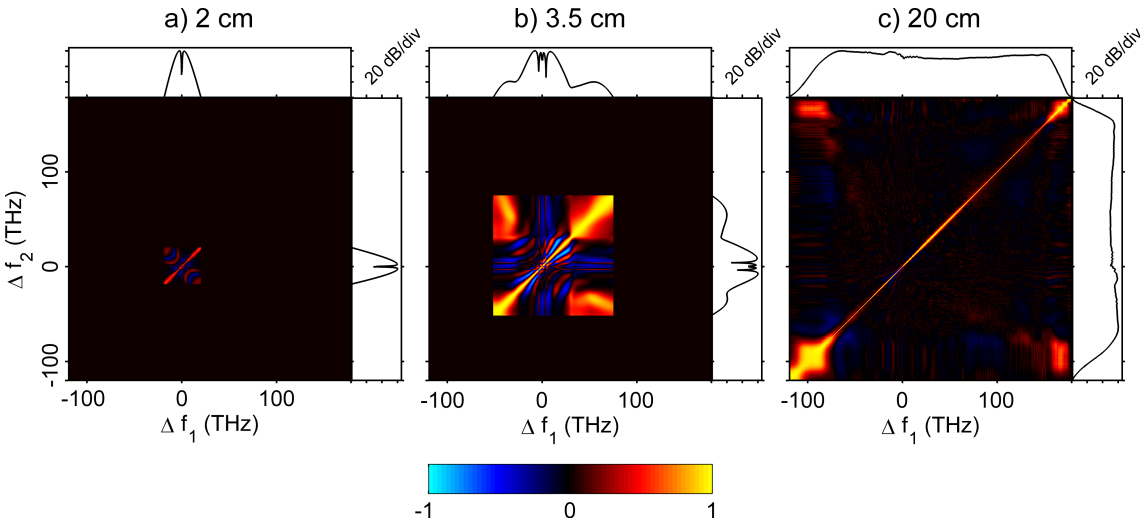

Figure 6.3: *The spectral correlation functions $\rho_f(f_1, f_2)$ and normalized spectra of 200 fs, 20 kW input pulses after specified propagation distances. The normalized spectra have been cut at –60 dB and the correlation trace has been set to zero for those frequencies that have less than –60 dB normalized power. The frequency axis show the frequency difference from the central frequency of the initial pulse, which is approximately 283 THz.*

except for the diagonal and the edges of the spectrum.

The initial spectral evolution displays a clear multipeak structure, which can be seen in figure 6.1 b) and figures 6.3 a) and b). This is due to SPM, which is the dominating process in the initial spectral broadening [28]. The blue crosses of anticorrelation in figures 6.3 a) and b) correspond to the narrow dips of the mean spectrum and are a manifestation of the fact that when new frequency components are generated, the energy comes from existing frequency components. Energy has been trasferred to other frequencies from the frequencies corresponding to the dips of the mean spectrum, and therefore these frequencies are anticorrelated with almost every other frequency and correlated with each other. The losses are negligible and energy has to be conserved, so the more energy is lost at certain frequencies, the more energy is gained by others.

Although SPM is the dominating process in the initial evolution, not every feature of the correlation patterns can be explained in terms of it. The sinusoidal patterns seen in figures 6.2 a) and b) seem to be indicators of MI, and it is actually true that weak MI occurs even for such short pulses. This can be verified by looking at the spectra after 2 cm of propagation, and figure 6.1 b) shows that weak sidebands start to form around 2 cm. The sidebands cannot be seen in the mean spectrum of figure 6.3 a) because they are more than 60 dB weaker than the central part of

the spectrum, but they have been amplified to approximately -40 dB after a further 1.5 cm of propagation and can be seen in figure 6.3 b). The correlations give no insight to the actual strength of the modulation and they are not a measure of the magnitude of the MI. The high correlations and anticorrelations in the sinusoidal patterns simply reveal that the frequency of the modulation is always very close to the same value, but the weak amplitude of the modulations keeps changing from simulation to simulation.

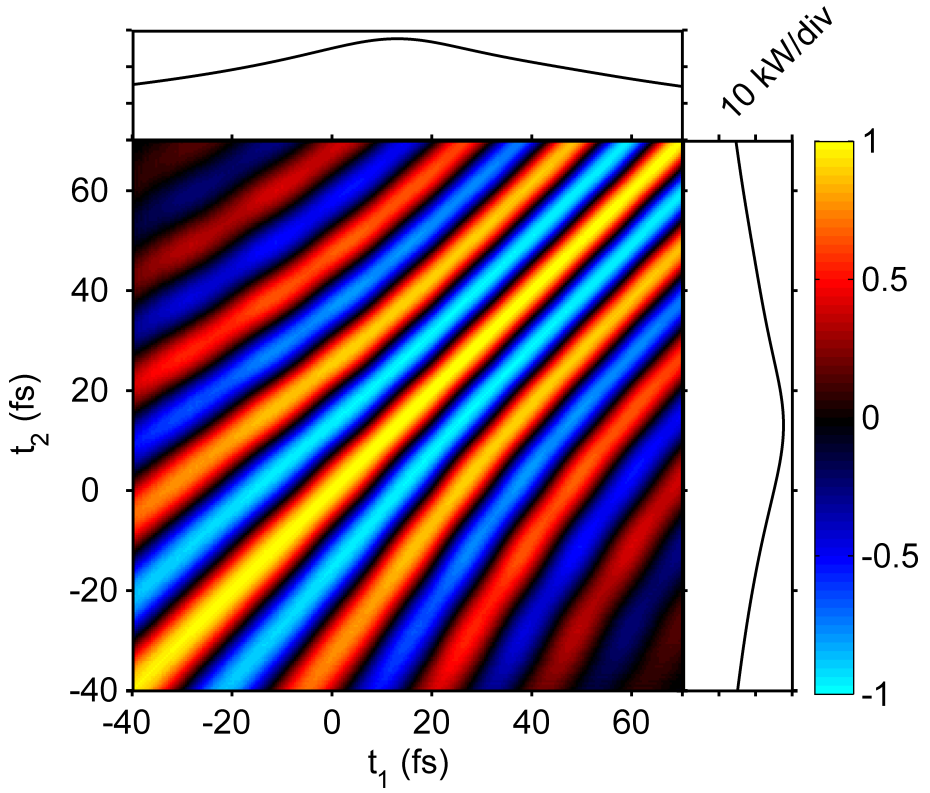

Figure 6.4: *The temporal correlation pattern of the 200 fs, 20 kW ensemble after 3.5 cm of propagation. This is zoomed version of figure 6.2 b).*

Figure 6.4 shows the sinusoidal pattern of figure 6.2 b) in more detail. The horizontal (or equivalently vertical) period of the pattern is between 20 fs and 25 fs, which corresponds to frequency shifts of 1/20 fs = 50 THz and 1/25 fs = 40 THz and thus matches exactly to the location of the sidelobes in the mean spectrum shown in figure 6.3 b). This is a verification that the sinusoidal pattern in the pseudocolor graph of the temporal correlation function is due to noise-seeded MI. MI theory would predict sidelobes peaking at $\sqrt{2\gamma P_0/|\beta_2|}/(2\pi) \approx 42$ THz (see the blue 20 kW case of figure 4.2), so the simulations are in perfect agreement with the theory. Note that MI theory is accurate for undepleted CW pumps only, but it works here because we are looking at the initial weak modulations forming close to the center of the pulse, where the peak power is approximately constant. Figure 6.2 also shows how the pattern period increases and how the pattern gets dimmer further away from

the temporal pulse center, which are both due to the lower optical intensity away from the pulse center and the assosicated decreases in MI gain and the modulation frequency.

When the MI sidebands grow larger, they can generate additional sidebands through cascaded FWM. For an undepleted pump pulse this would create a correlation pattern with reddish squares. Such a pattern is obviously missing in figure 6.3 c), and the lack of correlations has its origins in pump depletion and soliton fission followed by subsequent soliton dynamics. Soliton fission and soliton dynamics are affected by the input noise and the initial evolution. The fact that the mean spectrum in figure 6.3 c) is flat and the single shot spectrum of figure 6.1 b) has lots of dips shows that there is no way to predict the output power at a single frequency. The lack of correlations is simply a reflection of this. The spectra of solitons and dispersive waves are affected by Raman scattering and other nonlinear interactions, and the interaction of two waves requires that the waves overlap temporally. Therefore, temporal effects also have a role in the spectral correlations.

The temporal intensity of a single simulation shown in figure 6.1 a) should be compared to the mean intensity profile shown in figure 6.2 c). The mean intensity is quite flat whereas the intensity profile of the single simulation has solitons and other peaks with regions of low intensity between them. The peaks and low intensity regions of intensity profiles of single simulations average out when calculating the mean intensity because the locations of the solitons and other peaks keep changing from simulation to simulation. The eventual spectral evolution is characterized by the interaction of solitons and dispersive waves, and because the locations and central frequencies of the solitons vary from shot to shot, the interactions are unpredictable. Although the temporal locations and central frequencies of solitons are somewhat random, they do obey certain rules, the most obvious rules being that bright solitons can only exist in the anomalous GVD regime and they cannot be formed temporally far away from the input pulse. The phases of solitons obviously follow a higher degree of randomness, and because the interactions of solitons can be highly phase-dependent [112], even slight variations in the initial noise can cause large fluctuations in the output spectra and temporal intensity profiles. The output correlations are thus small in both domains.

For lower peak powers fewer solitons are formed, and this raises a natural question about the influence of the input soliton order. The order is larger for higher input peak powers, so using a lower input peak power gives insight to the corresponding evolution dynamics. Figure 6.5 shows the temporal correlation function at

the fiber output for an input of 200 fs duration and 8 kW peak power. The mean in-

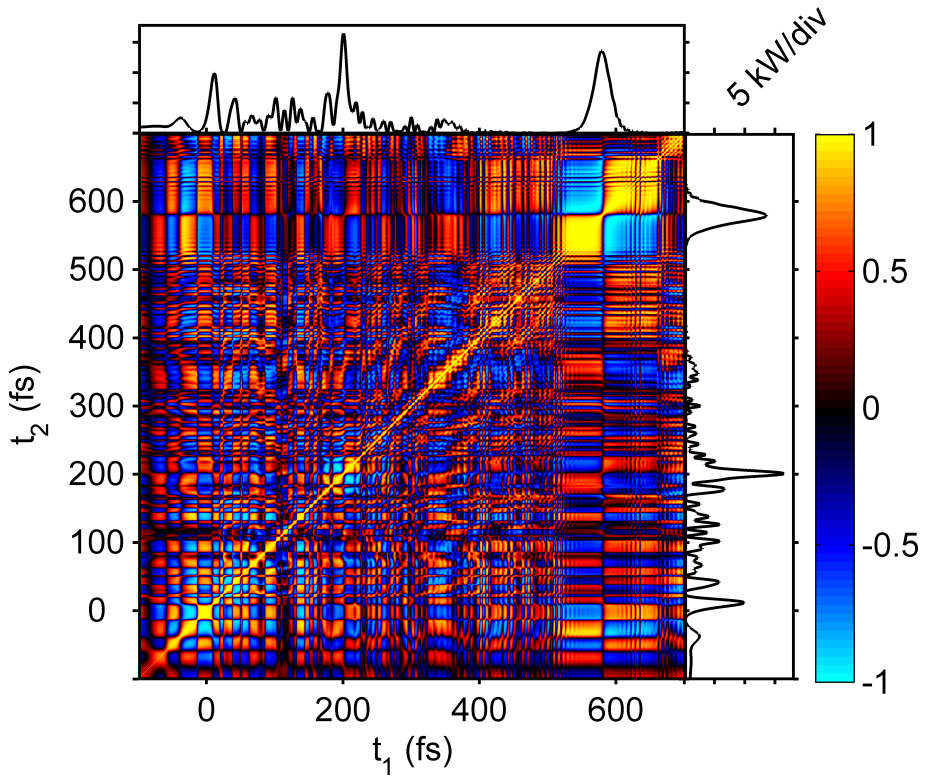

Figure 6.5: *The mean intensity and the temporal correlation pattern $\rho_t(t_1, t_2)$ of the 200 fs, 8 kW ensemble after 20 cm of propagation (at the fiber output).*

tensity displays clear structure and is not flat like that in figure 6.2 c). The intensity pattern even shows an obvious soliton around 600 fs. The fact that the soliton is visible in the mean intensity means that it forms in almost the exact same location and has almost the same central frequency in every realization independent of the initial noise. Also other possible solitons are visible in the mean spectrum: there is one around 0 fs and one around 200 fs, and the latter seems to be interacting with other solitons and/or dispersive waves. The solitons are always accompanied by a certain two-by-two checkerboard structure in the graph of the correlation function. The structure has four square regions highly correlated with themselves and highly anticorrelated with the two adjacent squares. This is most visible for the soliton at 600 fs, but it also exists for the other two possible solitons, though their checkerboard patterns are somewhat distorted by the presence of dispersive waves.

Such a two-by-two checkerboard pattern can be created by generating an ensemble of identical or nearly identical pulses, the locations of which vary only slightly from shot to shot, and calculating the correlation within that ensemble. The explanation is simple. Consider such an ensemble of pulses where the temporal location of the pulse varies around a certain value from shot to shot but the shape of the pulse

stays more or less the same (as would arguably be in the case of solitons). If the pulse lags behind the mean temporal location, intensities at the trailing edge will be larger than on average, whereas the leading edge experiences lower intensities. When the pulse leads the mean temporal location, the opposite is true. The trailing and leading edges thus never experience high or low intensities simultaneously, and they will therefore be correlated with themselves and anticorrelated with each other.

The fact that the solitons are associated with the checkerboard correlation patterns is evidence of *soliton timing jitter*. The location of the forming solitons keep varying slightly from simulation to simulation. Also the checkerboards are not quite -1's and 1's, so the correlation and anticorrelation is not exactly perfect. This can be explained by assuming that also the durations of the solitons vary slightly from shot to shot. Broader solitons have simultaneously more energy for smaller and larger values of t because their edges are more intense at the expense of the peak power. Thus smaller intensities for smaller values of t do not always mean larger intensities for larger values of t, and vice versa. The clarity of the checkerboard pattern of the most obvious soliton at 600 fs is still striking, so variations in the soliton duration and peak power are small.

Because the velocity of a soliton depends on its central frequency, the observed soliton timing jitter might be due to variations in the central frequency, as is usually the case in soliton communication systems [4]. Another explanation for the variation in the temporal location of the soliton might be that the soliton starts to form at a different part of the pulse in different simulations. In order to determine whether the central frequency of the soliton plays any role in the timing jitter, a *cross-domain correlation* function defined as

$$\rho_{\mathrm{c}}(t,f) = \frac{\langle I(t)I(f)\rangle - \langle I(t)\rangle \langle I(f)\rangle}{\sqrt{\left(\langle I^2(t)\rangle - \langle I(t)\rangle^2\right)\left(\langle I^2(f)\rangle - \langle I(f)\rangle^2\right)}} \tag{6.1}$$

is introduced. The function lacks a clear physical meaning, and to the author's best knowledge this is the first time such a function is used. The mathematical meaning, however, is very intuitive: the function describes whether the temporal intensity $I(t)$ is correlated with the spectral intensity $I(f)$. In the context of solitons such a function could prove useful because solitons of lower frequencies propagate at lower speeds and therefore one might hope to observe correlations between the temporal and spectral intensities.

Figure 6.6 shows the cross-domain correlation function for the ensemble in the vicinity of the soliton at 600 fs. Because also other solitons formed in the realizations

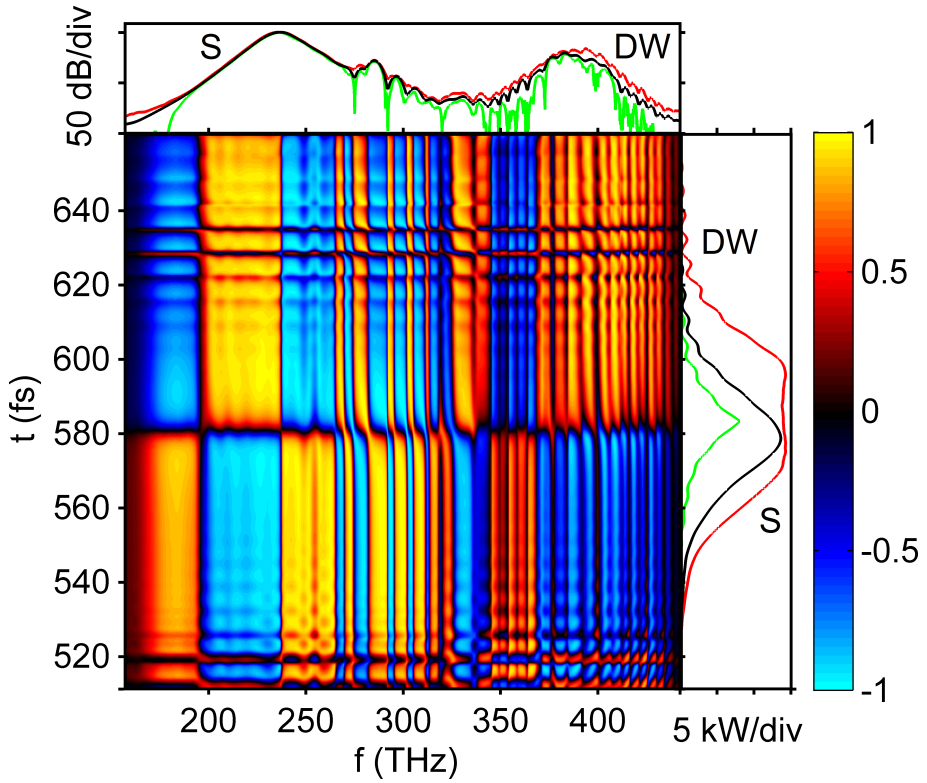

Figure 6.6: *The cross-domain correlations of the filtered 200 fs, 8 kW ensemble around the solitary soliton. The upper plot shows the normalized mean spectrum in black and the range for the normalized spectra in red and green in the sense that the normalized spectrum of every simulation in the ensemble is between the red and green curves. The rightmost plot next to the colorbar shows the mean intensity in the time domain in black and the respective range of intensities in the ensemble in red and green.*

have similar spectral components as the soliton at 600 fs, the simulations were temporally filtered using a super-Gaussian window such that only the soliton and the adjacent dispersive wave remained. The spectrum of each realization was then calculated from the filtered realization so that the spectrum represents the combined spectra of the soliton and the DW only. The low-frequency part of the spectrum ($f < 190$ THz) shows considerable intensity fluctuations as the red, green, and black curves do not merge, and that part of the spectrum cannot be reliably considered to belong to the soliton only. The shape of the red and green curves in that region indicates that there is something else at those frequencies besides the soliton. The normalized intensity is very small (< -50 dB) in that region, so even minuscle variations in the filtered electric field are able to cause the fluctuations. Therefore, the correlation function is unreliable for $f < 190$ THz. However, the frequency range from 190 THz to 270 THz belongs to the soliton. Such high spectral intensities at low frequencies can only be due to the soliton because of the filtering.

Taking the aforementioned fluctuation issues into account, figure 6.6 shows clear evidence that the soliton central frequency is indeed involved in the timing jitter. There is a clear two-by-two checkerboard pattern ranging from 190 THz to 270 THz in the frequency domain and throughout the temporal scale, and its structure is exactly what could be expected. In that soliton frequency range from 190 THz to 270 THz higher frequencies are highly correlated with the leading edge of the soliton and anticorrelated with the trailing edge, whereas lower frequencies are correlated with the trailing edge an anticorrelated with the leading edge. This means that whenever the soliton has lagged behind its mean temporal location, its central frequency is lower, and when the temporal location of the soliton is smaller, its frequency is higher. The correlations are surprisingly close to 1 and -1, so that one can conclude that the timing jitter is solely due to shot-to-shot variations in the central frequency of the soliton and not because the soliton would form at different parts of the input pulse in different simulations.

The cross-domain correlation pattern also shows how the DW region ($f > 370$ THz) is mostly correlated with the trailing edge of the soliton, but the value of the correlation function varies sinusoidally between 0 and 1 in that region. This can be due to the presence of multiple dispersive waves of similar frequencies, and it might be that there is one dispersive wave at the leading edge of the soliton and one at the trailing edge. The trailing edge DW can then be trapped by the soliton and they can exchange energy, which would explain the correlation: larger soliton red-shift means a larger DW blue-shift and causes the soliton to lag more, which leads to larger intensities at higher values of t.

6.2 Coherence in the Short-Pulse Regime

The coherence (absolute values of the normalized MCFs and CSDs) at the fiber output for the 200 fs, 20 kW ensemble is shown in figure 6.7. Each of the graphs display a coherent diagonal, but there are distinctive features between the graphs. a) shows how the leading edge of the input pulse is highly coherent and experiences little shot-to-shot fluctuations. Everything else is incoherent except for the diagonal. The intensity MCF shown in b) displays a clear blue region of low coherence at the trailing edge. The CSD for the electric field is shown in c), and it has the feature of a coherent square centered at the input frequency. This square is missing in d), and the coherent line is actually very narrow in the vicinity of the input frequency.

The notable lack of overall coherence in the the MCFs is a manifestation of soliton dynamics that are sensitive to initial noise if the peak power is high enough. The supercontinua generated by input pulses of smaller peak powers are highly co-

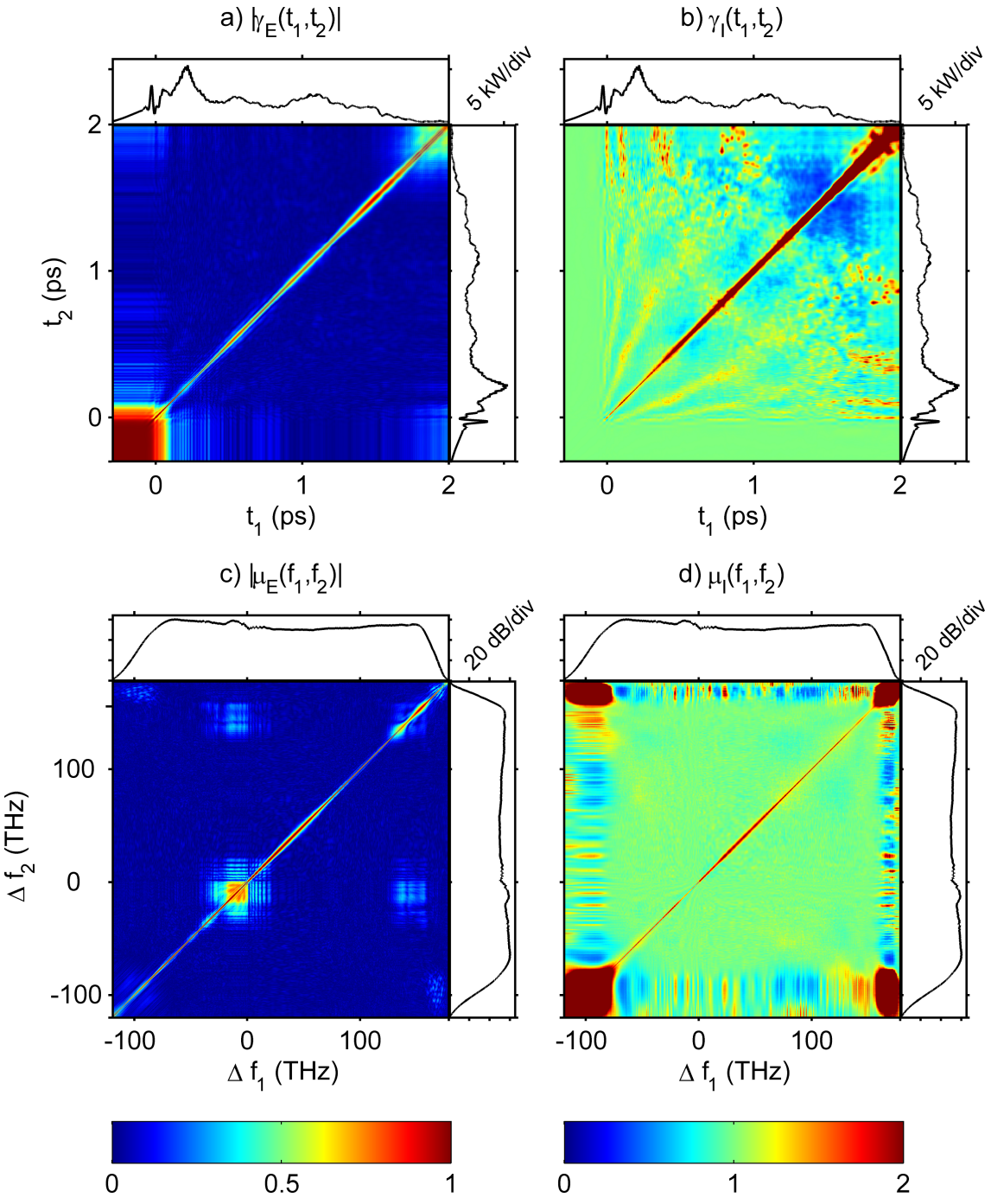

Figure 6.7: *Absolute values of the normalized MCFs (a) and b)) and CSDs (c) and d)) for electric fields and intensities at the fiber output for the 200 fs, 20 kW ensemble. The color scale is from 0 to 1 in a) and c) and from 0 to 2 in b) and d). Mean intensities and normalized spectra are shown on top of and next to each pseudocolor graph of the MCFs and CSDs, respectively.*

herent because the dominating spectral broadening mechanism is noise-insensitive SPM, whereas significant overall coherence degradation was observed for peak powers larger than 10 kW, which is consistent with earlier studies [33]. The explanation for the blue incoherent region for the intensity MCF requires a more detailed anal-

ysis. It was rare to observe multiple solitons for $t >$ 1 ps, and that region usually had a single soliton of high intensity and a trapped DW. Except for the soliton and the possible DW, the intensity was very low (see the temporal intensity profile of figure 5.1 a), for example). Therefore, $I(t_2)I(t_1)$ always tends to be close to zero for $|t_2 - t_1| > T_{\mathrm{sol}}$, where T_{sol} is the soliton duration, because at least one of the factors is very small. The intensities of the red-shifted solitons are high enough to make the mean intensities $\langle I(t_1)\rangle$ and $\langle I(t_1)\rangle$ large compared to $\langle I(t_2)I(t_1)\rangle$, and the MCF, which is the ratio of $\langle I(t_2)I(t_1)\rangle$ and $\langle I(t_1)\rangle\langle I(t_1)\rangle$, is consequently small. This could indicate sub-Poissonian statistics.

The coherent square in the electric field CSD shown in c) is due to the pump remains. Lasers produce highly coherent pulses, and the coherence of the input spectrum is not lost in the fiber except for the spectrum edges, where a significant portion of the output power has been generated in the fiber through nonlinear processes. The intensity CSD does not have a similar coherent square, and the value of the intensity CSD is also close to unity. The output intensities at frequencies close to the input pulse central frequency seem to follow an exponential distribution, but in reality it is closer to the Boltzmann-distribution. The field CSD would be closer to zero and the intensity CSD would show a higher degree of coherence if the distribution was an exponential one. The observed high coherence in the electric field CSD tells that the phase fluctuations at the vicinity of the input pulse central frequency do not follow a uniform random distribution but that certain phases are more probable than others and the distribution resembles a Gaussian distribution. This can be seen in figure 6.8. The other frequency components in the vicinity of the pump frequency follow

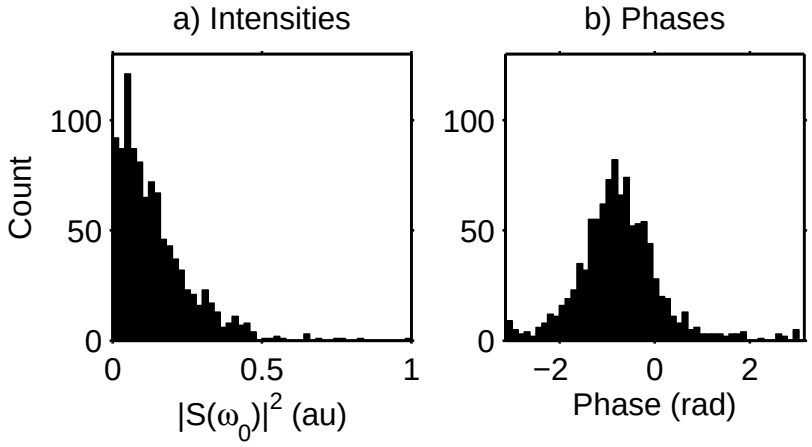

Figure 6.8: *Histograms of the intensities and phases of the pump frequency at the fiber output for the 200 fs, 20 kW ensemble.*

similar distributions with different mean phases, and outside the coherent square the distribution of phases gets broader and eventually uniform, which causes the

field CSD to vanish.

6.3 Correlations in the Long-Pulse Regime

The long-pulse regime correlations are studied using 1 ps, 10 kW input pulses. Other parameters are similar to the short-pulse case. Figure 6.9 shows the temporal and spectral evolution of a single 1 ps, 10 kW pulse.

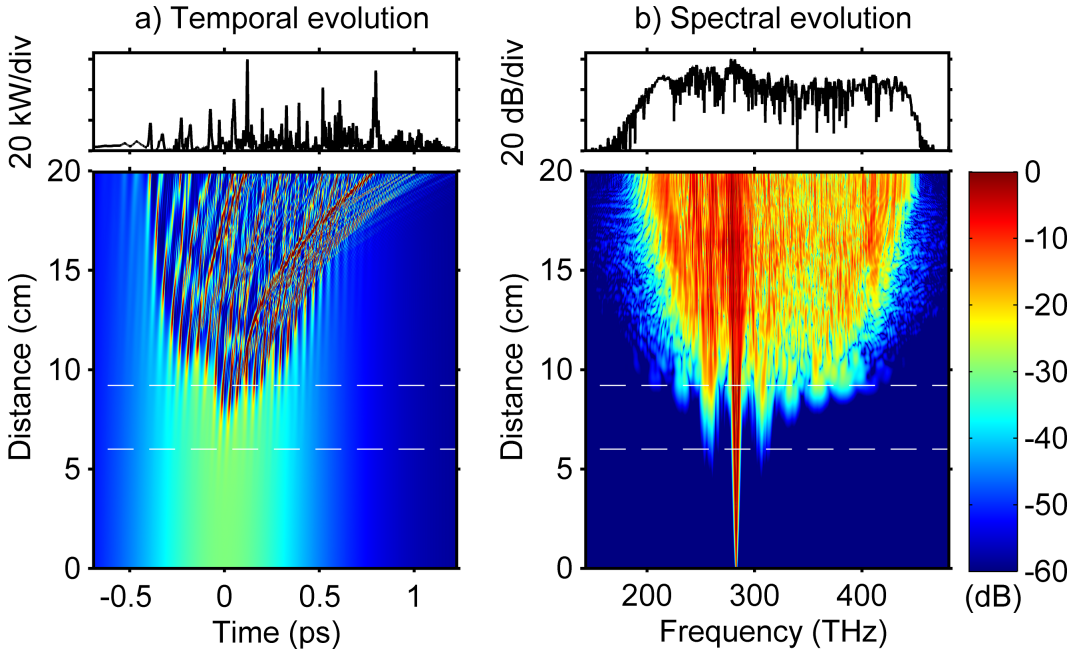

Figure 6.9: *The temporal and spectral evolution of a 1 ps, 10 kW pulse. The color axis has been cut at 20 kW for the temporal trace and ranges from –60 dB to 0 dB for the normalized logarithmic spectral trace. The white horizontal dashed lines are at 6 cm and 9.2 cm and denote propagation distances of relevance in terms of correlations.*

In both domains the evolution follows a clear pattern up to about 10 cm. Sidelobes corresponding to spontaneous MI start to develop around 5 cm and they are visible in the spectral trace and cause modulation in the temporal trace. As the modulation deepens, the pulse becomes a train of narrower pulses which then adjust themselves to become solitons and start red-shifting and decelerating. Lots of closely spaced solitons are formed, and soliton dynamics can be expected to have a significant role in the subsequent evolution. The output spectrum shows a peak at low frequencies, which corresponds to the frequencies of the solitons that have experienced the largest red-shift.

Figure 6.10 shows the temporal intensity correlation function for the 1 ps, 10 kW ensemble at the propagation distances specified by the white lines of figure 6.9. The mean intensity is very similar in the first two subfigures but different from the mean

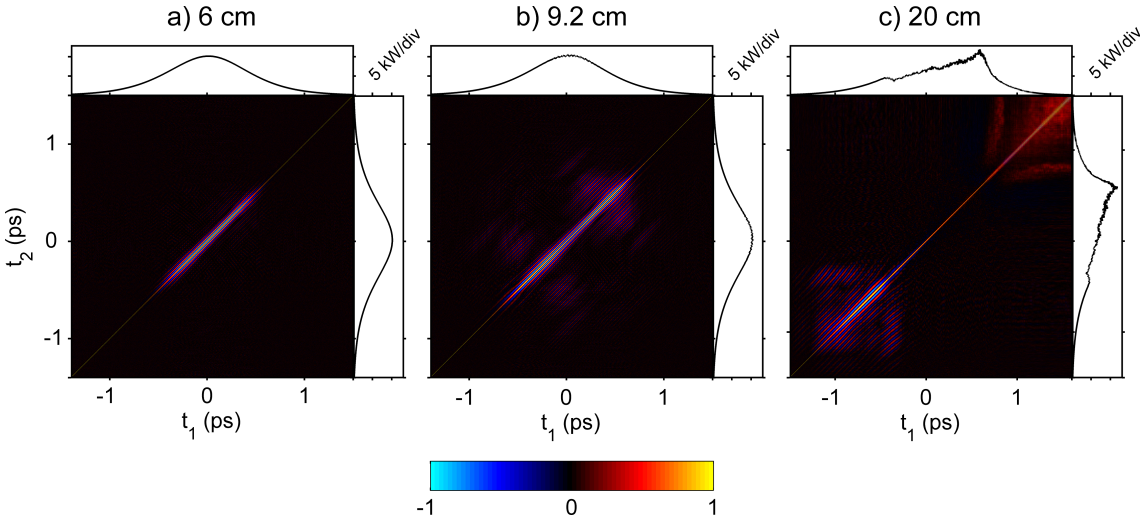

Figure 6.10: *The temporal correlation functions $\rho_t(t_1, t_2)$ and normalized spectra of the 1 ps, 10 kW input pulse ensemble after specified propagation distances.*

output intensity which peaks at a later time around 6 picoseconds. The correlation plot of a) shows a sinusoidal pattern along the diagonal line. Plot b) shows two square-like regions displaying a similar sinusoidal pattern in addition to the pattern along the diagonal line. In c) the sinusoidal pattern is only visible for correlations at the leading edge of the pulse ($t_1, t_2 < 0$), and besides the diagonal line of unity correlation, the only feature is the weakly correlated trailing edge. The sinusoidal pattern in the temporal correlations also manifests itself in the spectral correlations. Figure 6.11 shows the corresponding spectral intensity correlation functions. The

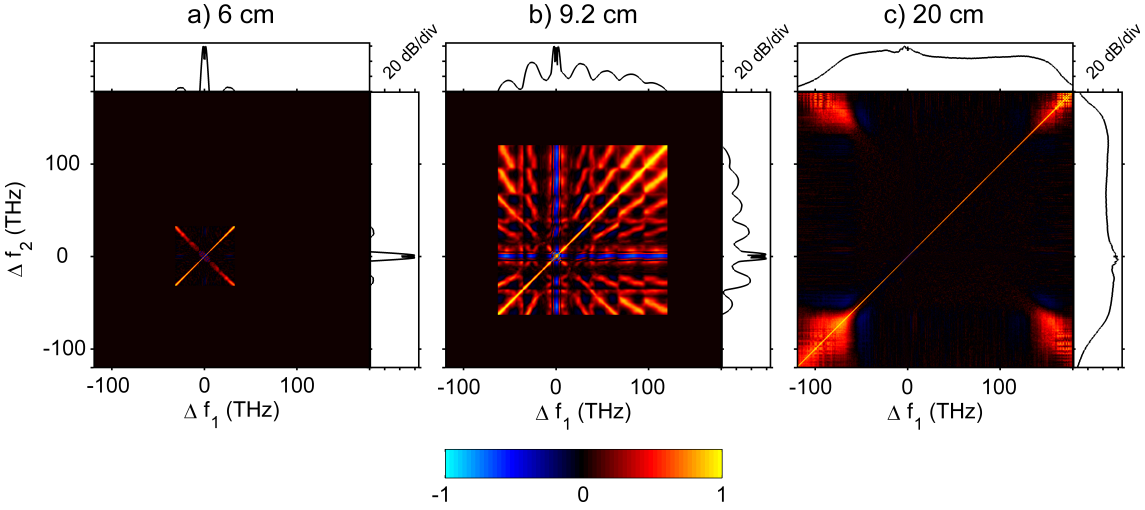

Figure 6.11: *The spectral correlation functions $\rho_f(f_1, f_2)$ and normalized spectra of 1 ps, 10 kW input pulses after specified propagation distances. The normalized spectra have been cut at –60 dB and the correlation trace has been set to zero for those frequencies that have less than –60 dB normalized power.*

emerging sidelobes are barely visible in subfigure a), which means that their nor-

malized intensity is only slightly over -60 dB. The corresponding correlation pattern is shaped like an X with tiny curved regions of anticorrelation at the center. The pulse central frequency is also anticorrelated with the sidelobes. As the propagation distance is increased, more sidelobes emerge through cascaded FWM and a dip at the central frequency forms in the mean spectrum. The correlation pattern has a similar highly correlated X, but it also has other features such as the blue cross of anticorrelation. The pattern also appears to be tile-like, with each tile having a diagonal line of high correlation. The mean output spectrum shown in subfigure c) is very flat except for the small peak at the pump frequency. $\rho_{\mathrm{f}}(f_1, f_2)$ is close to zero everywhere except for the narrow $f_1 = f_2$ diagonal and the spectrum edges, which are correlated with themselves and with each other.

The features observed in the correlation patterns can be explained by MI, SPM, and subsequent soliton dynamics. MI leads to the sinusoidal pattern in figure 6.10 and the spectral sidelobes of figures 6.11 a) and b). Theory predicts that the first-order sidelobes should be separated from the pump frequency by 30 THz (see the 10 kW case in figure 4.2), so the results are in agreement with the MI theory. Whereas the sidelobes are explained by MI, the multipeak structure of the central part of the spectrum is due to SPM. The effect of SPM on the correlation pattern is to form the blue cross of anticorrelation, but now the cross is also partially due to MI. MI transfers energy from the pump frequency to other frequencies, so the pump frequency should be anticorrelated with all the other frequencies. The red tiles seen in figure 6.11 b) are not observed in c) because of the effect of soliton dynamics on the spectrum. Soliton dynamics have a drastic effect of the output spectrum mostly because of SRS an SPM but also FWM and soliton trapping. The edges of the output spectrum are due to solitons and dispersive waves, which is what explains the high correlations. Although the solitons can make the output spectrum unpredictable, they cannot disturb the sinusoidal pattern seen in the leading edge of the pulse in figure 6.10 c). This is due to the fact that solitons lag behind the initial pulse and thus do not interact with the leading edge of the pulse.

6.4 Coherence in the Long-Pulse Regime

Although the use of 10 kW input peak power leads to coherent or quasi-coherent supercontinua when fed to the fiber used in this study, the same peak power is large enough to cause vast coherence degradation in the long-pulse case. Figure 6.12 shows the normalized MCFs and CSDs for the 1 ps, 10 kW ensemble. Figure 6.12 can be seen to remind figure 6.7 in may respects. Notable differences include the higher value of $\gamma_{\mathrm{E}}(t_1, t_2)$ near the pulse edges and an even more complete lack of temporal coherence in the central part of the pulse. The intensity MCF $\gamma_{\mathrm{I}}(t_1, t_2)$

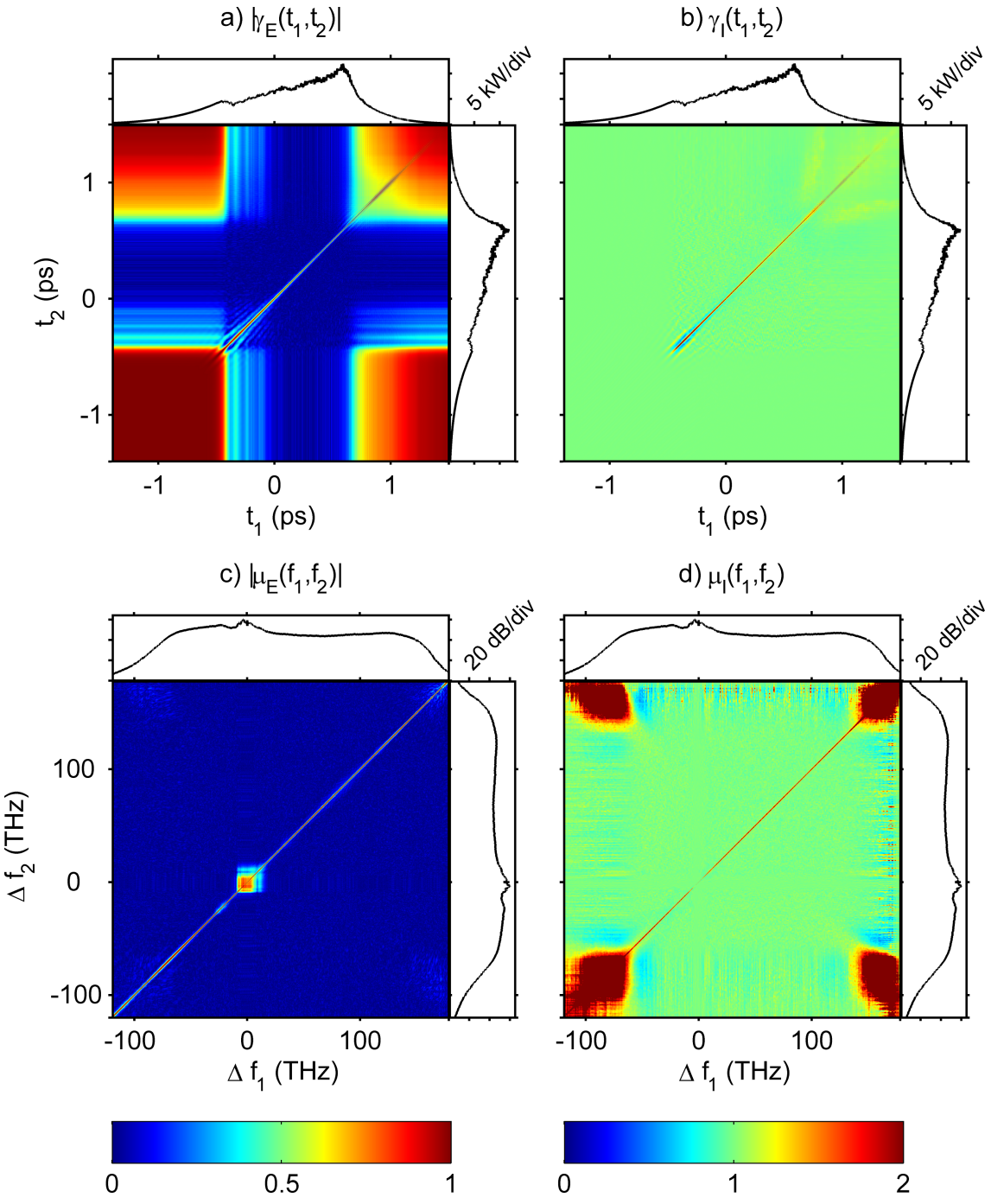

Figure 6.12: *Absolute values of the normalized MCFs (a) and b)) and CSDs (c) and d)) for electric fields and intensities at the fiber output for the 1 ps, 10 kW ensemble. The color scale is from 0 to 1 in a) and c) and from 0 to 2 in b) and d). Mean intensities and normalized spectra are shown on top of and next to each pseudocolor graph of the MCFs and CSDs, respectively.*

is very close to unity everywhere except for the diagonal, which is not the case in the short pulse regime. The structures of the mutual coherence functions suggests Gaussian statistics [109]. In c) the coherent square is smaller and the coherent diagonal, which represents the quasi-stationary part as described in reference [33], is

thinner. The coherent diagonal is also thinner in the intensity CSD shown in d) when compared with figure 6.7 d). The intensity CSD attains high values in the spectrum edges.

All of the observed differences can be explained by the contribution of MI, its sensitivity to input noise, SPM, and soliton dynamics that start to play a role after the pulse center has become a train of solitons. The pulse edges are temporally coherent because optical power at the pulse edges is not sufficiently large for MI to occur in the 20 cm fiber. The MI gain is too small for the edges to become deeply modulated. The trailing edge is more incoherent than the leading edge because the solitons formed at the pulse center can sometimes have sufficiently high peak powers so that they are significantly red-shifted and consequently slow down and end up overlapping with the trailing edge pulse remains. Interactions of solitons and the resulting Raman-induced energy exchange leads to even more evident coherence degradation in the spectral domain.

The coherent square in the field CSD seems smaller but somewhat more coherent than in the short-pulse regime. Indeed, figure 6.13 shows that the corresponding spectral intensity and phase distributions for the pump frequency at the output are different from their respective short-pulse counterparts. The intensity distribution looks more like a Boltzmannian or a slightly Gaussian distribution, and the phases are evidently normally distributed with a smaller standard deviation than in the short-pulse regime.

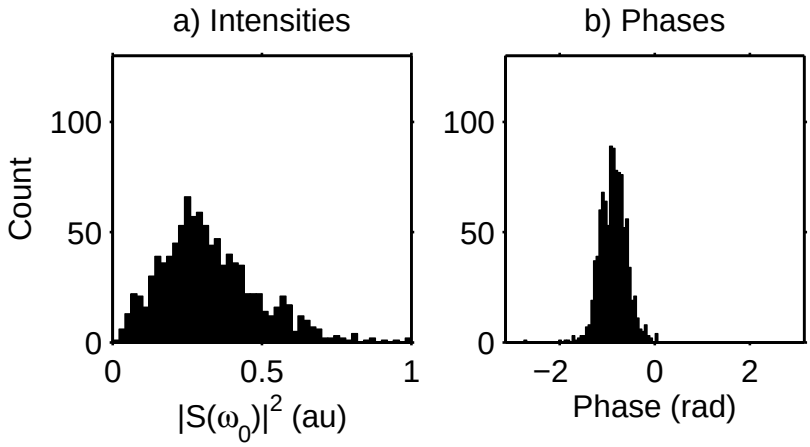

Figure 6.13: *Histograms of the intensities and phases of the pump frequency at the fiber output for the 1 ps, 10 kW ensemble.*

The explanation for the smaller coherent square is simply that the initial spectrum is narrower, so the frequency band that can stay coherent due to SPM throughout the fiber is smaller. The higher coherence in the square can be attributed to the facts

that the effect of MI on the input frequency components is predictable and similar from simulation to simulation and that the fiber is too short for MI to deplete the pump completely.

In the case of stationary light, which corresponds to a multivariate Gaussian random process, the MCFs would fulfill the moment theorem and satisfy $\gamma_{\mathrm{I}}(t_1, t_2) \approx 1 + |\gamma_{\mathrm{E}}(t_1, t_2)|^2$ [108, 109]. The validity of the moment theorem shows whether the process obeys Gaussian statistics, and this can be visualized by plotting $\gamma_{\mathrm{I}}(t_1, t_2)$ and $1 + |\gamma_{\mathrm{E}}(t_1, t_2)|^2$ for a constant $t_1 + t_2$ as a function of $t_2 - t_1$. This corresponds to taking diagonal cuts from top left to bottom right in figures 6.12 a) and b). Figure 6.14 shows $\gamma_{\mathrm{I}}(t_1, t_2)$ and $1 + |\gamma_{\mathrm{E}}(t_1, t_2)|^2$ and thus the validity of the moment theorem for two different values of $t_1 + t_2$.

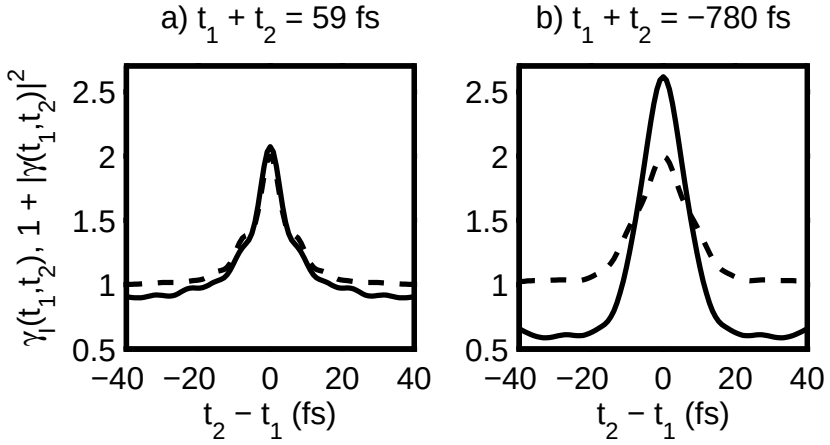

Figure 6.14: *The intensity MCF $\gamma_I(t_1, t_2)$ (solid line) and $1 + |\gamma_E(t_1, t_2)|^2$ (dashed line) for the 1 ps, 10 kW ensemble at two different values of $t_1 + t_2$.*

It can be seen that the moment theorem holds for some values of $t_1 + t_2$ but is not fulfilled for others. The agreement between $\gamma_{\mathrm{I}}(t_1, t_2)$ and $1 + |\gamma_{\mathrm{E}}(t_1, t_2)|^2$ is decent for positive values of $t_1 + t_2$, which shows that the long-pulse regime SC generation obeys approximately Gaussian statistics in the trailing edge of the pulse.

7. CONCLUSIONS AND OUTLOOK

The intensity correlations of supercontinua were studied in both short- and long-pulse regimes. It was shown that the features of the correlation functions can be explained in terms of nonlinear optical processes and that the correlation functions contain information about the occuring and dominating phenomena. The coherence properties were also studied, interpreted, and explained. The moment theorem was shown to hold approximately in the long-pulse regime.

The first chapters presented the basics of light propagation and classical electromagnetic theory. The following chapters focused on fiber optics. Nonlinear optical phenomena were introduced in a chapter devoted to them, and different nonlinear optical phenomena were discussed in detail with references to the original studies that led to their discoveries. A nonlinear propagation equation was presented and its analytical and numerical solutions were discussed. When the theoretical foundation of nonlinear light propagation in optical fibers had been laid, SC generation was discussed. Several measures for coherence and correlations were defined. The correlation properties of supercontinua were then analyzed by performing a massive amount of numerical simulations for various input parameters. The pulse evolution and correlation functions were analyzed in detail with specific examples of the two propagation regimes presented.

Several nonlinear optical phenomena were identified as being mainly responsible for the correlation and properties. The initial spectral broadening was observed to be due to SPM in the short-pulse regime and due to MI in the long-pulse regime. SPM-induced spectral broadening was seen to lead to coherent supercontinua whereas the MI-generated long-pulse and CW supercontinua were shown to lead to incoherent supercontinua. MI was shown to play a major role in the evolution dynamics, and correlation degradation was explained in terms of the noise-sensitivity of MI and eventual soliton dynamics. Solitons created either through soliton fission or MI were shown to be responsible for the observed correlation degradation upon propagation in both the short- and long-pulse regimes. Soliton timing jitter was identified as the reason behind the checkerboard patterns in the temporal correlation function graphs. The cross-domain correlation function was introduced to determine the ori-

gin of soliton timing jitter. The cross-domain correlation function was successfully used to argue that the observed soliton timing jitter is due to small shot-to-shot changes in the central frequency of the soliton.

It was also observed that the correlation patterns can be misleading because the value of the correlations state nothing about the value of the spectral or temporal intensity, and even pulse edges or dispersive waves of negligible intensities can yield strong correlations. Care must be taken in the interpretation of the correlation functions.

This work is the first step towards understanding the intensity correlations of supercontinua, and the results, their interpretation, and the new tool of cross-domain correlations presented in this work are expected to be of remarkable importance in future studies. Because of limited compotational power the study covers a relatively minor region of the vast parameter space, and a broader range of parameters may be used in the future. It would be useful to determine which input conditions lead to Gaussian statistics and whether even longer or more powerful pulses lead to a better fulfillment of the moment theorem. Also shorter pulses than those used in this study could be analyzed more thoroughly to get a better understanding of the underlying phenomena of highly coherent SC generation for various applications. Ultimately one might be interested in being able to generate both highly coherent and highly incoherent supercontinua with the same setup such that the degree of coherence can be altered by changing a single or only a few easily tunable parameters.

This study, along with the vast majority of studies of similar nature, neglected polarization effects. Higher-order coherence and correlation studies could be extended to take polarization effects into account because they are important in some situations both from the theoretical and practical point of view. The inclusion of polarization effects could mean higher-order correlation studies in birefringent fibers or at least a better model for randomly-varying birefringence. Polarization effects might offer a convenient way to tune the coherence and correlation properties of supercontinua if it is possible to generate a coherent SC polarized along one axis while simultaneously generating a more incoherent SC polarized along another axis. A simple polarizer could then be used to switch between coherent and incoherent supercontinua.

On a more fundamental level, the effect of pulse shape was also left for future studies, and this thesis focused solely the typical sech-shape. The use of Gaussian pulses might not tremendously alter the results presented here, but more exotic pulse

shapes could be explored. Besides pulse shape, there were also other limitations on the pulses considered, namely transform-limitations. All the pulses were assumed to be unchirped and transform-limited, and the effect of input chirp on coherence and correlations could be examined. Moreover, the effect of input pulse coherence was also not studied here. One might intuitively say that incoherent input pulses are not capable of producing coherent supercontinua, but the actual dependence of the output coherence on input coherence could be counterintuitive. A strong nonlinear dependence of output coherence on input coherence might offer yet another means to choose between coherent and incoherent supercontinua, if the introduction of slight input incoherence is able to turn coherent supercontinua into vastly incoherent. It might ultimately be possible to design a novel feedback control system for precise control of SC coherence over a broad range.

There are also numerous other possibilities for future studies. This thesis assumed anomalous pumping, and as SC generation in the normal dispersion regime differs considerably from the anomalous pumping case, the coherence and correlation properties would most likely be different, too. Besides anomalous pumping, the study also assumed single-mode operation throughout. Multimode SC generation might have advantages over single-mode SC generation in terms of the tunability of coherence and correlation properties, and if it does, one would naturally like to know.

The work presented here used a classical model with incorporated quantum phenomena. A more thorough quantum mechanical approach could offer more insight into the processes at the fundamental quantum level and also allow for a better understanding of quantum correlations. Nevertheless, for now the most obvious direction for future research would be to move from doing the experiments *in silico* to conducting them *in silica*.

BIBLIOGRAPHY

[1] Richard C. Dorf and Robert H. Bishop. *Modern Control Systems, 11th edition.* Pearson, 2008.

[2] Eugene Hecht. *Optics, Third Edition.* Addison Wesley Longman, 1998.

[3] Robert W. Boyd. *Nonlinear Optics, Third Edition.* Academic Press, 2008.

[4] Govind P. Agrawal. *Fiber-Optic Communication Systems, fourth edition.* Wiley, 2010.

[5] R. R. Alfano and S. L. Shapiro. Emission in the region 4000 to 7000 Å via four-photon coupling in glass. *Phys. Rev. Lett.*, 24:584–587, 1970.

[6] R. R. Alfano and S. L. Shapiro. Observation of self-phase modulation and small-scale filaments in crystals and glasses. *Phys. Rev. Lett.*, 24:592–594, 1970.

[7] R. R. Alfano and S. L. Shapiro. Direct distortion of electronic clouds of rare-gas atoms in intense electric fields. *Phys. Rev. Lett.*, 24:1217–1220, 1970.

[8] Chinlon Lin and R. H. Stolen. New nanosecond continuum for excited-state spectroscopy. *Appl. Phys. Lett.*, 28:216–218, 1976.

[9] Robert R. Alfano. *The Supercontinuum Laser Source, 2nd edition.* Springer, 2006.

[10] T. Morioka, K. Mori, and M. Saruwatari. More than 100-wavelength-channel picosecond optical pulse generation from single laser source using supercontinuum in optical fibres. *Electron. Lett.*, 29:862–864, 1993.

[11] T. Morioka, H. Takara, S. Kawanishi, O. Kamatani, K. Takigushi, K. Uchiyama, M. Sarawatari, H. Takahashi, M. Yamada, T. Kanamori, and H. Ono. 1 tbit/s (100gbit/s x 10 channel) otdm/wdm transmission using a single supercontinuum wdm source. *Electron. Lett.*, 32:906 –907, 1996.

[12] J. C. Knight, T. A. Birks, P. St. J. Russell, and D. M. Atkin. All-silica single-mode optical fiber with photonic crystal cladding. *Optics Letters*, 21:1547–1549, 1996.

[13] Jinendra K. Ranka, Robert S. Windeler, and Andrew J. Stentz. Visible continuum generation in air-silica microstructure optical fibers with anomalous dispersion at 800 nm. *Optics Letters*, 25:25–27, 2000.

[14] R. Holzwarth, Th. Udem, T. W. Hänsch, J. C. Knight, W. J. Wadsworth, and P. St. J. Russell. Optical frequency synthesizer for precision spectroscopy. *Phys. Rev. Lett.*, 85:2264–2267, 2000.

[15] I. Hartl, X. D. Li, C. Chudoba, R. K. Ghanta, T. H. Ko, J. G. Fujimoto, J. K. Ranka, and R. S. Windeler. Ultrahigh-resolution optical coherence tomography using continuum generation in an air-silica microstructure optical fiber. *Optics Letters*, 26:608–610, 2001.

[16] E. P. Ippen, C. V. Shank, and T. K. Gustafson. Self-phase modulation of picosecond pulses in optical fibers. *Appl. Phys. Lett.*, 24:190–192, 1974.

[17] R. H. Stolen and Chinlon Lin. Self-phase-modulation in silica optical fibers. *Phys. Rev. A*, 17:1448–1453, 1978.

[18] R. H. Stolen, J. E. Bjorkholm, and A. Ashkin. Phase-matched three-wave mixing in silica fiber optical waveguides. *Appl. Phys. Lett.*, 24:308–310, 1974.

[19] R. H. Stolen. Phase-matched-stimulated four-photon mixing in silica-fiber waveguides. *IEEE Journal of Quantum Electronics*, 11:100–103, 1975.

[20] V. V. Grigoryants, B. L. Davydov, M. E. Zhabotinski, V. F. Zolin, G. A. Ivanov, V. I. Smirnov, and Yu. K. Chamorovski. Spectra of stimulated raman scattering in silica-fibre waveguides. *Optical and Quantum Electronics*, 9:351–352, 1977.

[21] John AuYeung and A. Yariv. Spontaneous and stimulated raman scattering in long low loss fibers. *IEEE Journal of Quantum Electronics*, 14:347–352, 1978.

[22] Y. R. Shen and N. Bloembergen. Theory of stimulated brillouin and raman scattering. *Phys. Rev.*, 137:1787–1805, 1964.

[23] V. V. Grigoryants, V. I. Smirnov, and Yu K. Chamorovskii. Generation of wide-band optical continuum in fiber waveguides. *Sov. J. Quant. Elect.*, 12:841–847, 1982.

[24] Akira Hasegawa and Frederick Tappert. Transmission of stationary nonlinear optical pulses in dispersive dielectric fibers. i. anomalous dispersion. *Appl. Phys. Lett.*, 23:142–144, 1973.

[25] L. F. Mollenauer, R. H. Stolen, and J. P. Gordon. Experimental observation of picosecond pulse narrowing and solitons in optical fibers. *Phys. Rev. Lett.*, 45:1095–1098, 1980.

[26] F. M. Mitschke and L. F. Mollenauer. Discovery of the soliton self-frequency shift. *Optics Letters*, 11:659–661, 1986.

[27] Barry Gross and Jamal T. Manassah. Supercontinuum in the anomalous group-velocity dispersion region. *JOSA B*, 9:1813–1818, 1992.

[28] J. M. Dudley, G. Genty, and S. Coen. Supercontinuum generation in photonic crystal fiber. *Reviews of Modern Physics*, 78:1135–1176, 2006.

[29] John M. Dudley and Stéphane Coen. Numerical simulations and coherence properties of supercontinuum generation in photonic crystal and tapered optical fibers. *IEEE Journal of Selected Topics in Quantum Electronics*, 8:651–659, 2002.

[30] J. M. Dudley and S. Coen. Coherence properties of supercontinuum spectra generated in photonic crystal and tapered optical fibers. *Optics Letters*, 27:1180–1182, 2002.

[31] Xun Gu, Mark Kimmel, Aparna Shreenath, Rick Trebino, John Dudley, Stéphane Coen, and Robert Windeler. Experimental studies of the coherence of microstructure-fiber supercontinuum. *Optics Express*, 11:2697–2703, 2003.

[32] Ju Han Lee, Young-Geun Han, and Sang Lee. Experimental study on seed light source coherence dependence of continuous-wave supercontinuum performance. *Optics Express*, 14:3443–3452, 2006.

[33] G. Genty, M. Surakka, J. Turunen, and A. T. Friberg. Complete characterization of supercontinuum coherence. *J. Opt. Soc. Am. B*, 28:2301–2309, 2011.

[34] Minna Korhonen, Ari T. Friberg, Jari Turunen, and Goëry Genty. Elementary field representation of supercontinuum. *JOSA*, 30:21–26, 2013.

[35] Sir Isaac Newton. *Opticks*. 1704.

[36] René Descartes. *La Dioptrique*. 1637.

[37] Robert Hooke. *Micrographia*. 1665.

[38] Christiaan Huygens. *Traité de la lumière*. 1690.

[39] Thomas Young. Experimental demonstration of the general law of the interference of light. In *Philosophical Transactions of the Royal Society of London*, volume 94, 1804.

[40] Andrzej Wróblewski. de mora luminis: A spectacle in two acts with a prologue and an epilogue. *Am. J. Phys.*, 53 (7):620–630, 1985.

[41] W. Heisenberg and H. Euler. Folgerungen aus der diracschen theorie des positrons. *Zeitschrift für Physik A: Hadrons and Nuclei*, 98:714–732, 1936.

[42] Michael Mansfield and Colm O'Sullivan. *Understanding Physics*. Wiley, 1999.

[43] John A. Wheeler Charles W. Misner, Kip S. Thorne. *Gravitation*. Freeman, 1973.

[44] Keijo Ruohonen. Vektorikentät, 2011.

[45] Chris Doran and Anthony Lasenby. *Geometric Algebra for Physicists*. Cambridge University Press, 2003.

[46] Stephen Gasiorowicz. *Quantum Physics, 3rd edition*. Wi, 2003.

[47] A. Sommerfeld and G. Wentzel. Über reguläre und irreguläre dubletts. *Zeitschrift für Physik A: Hadrons and Nuclei*, 7:86–92, 1921.

[48] W. Heisenberg. Zur quantentheorie der linienstruktur und der anomalen zeemaneflekte. *Zeitschrift für*, 8:273–297, 1922.

[49] N. Bohr. Über die anwendung der quantentheorie auf den atombau i. die grundpostulate der quantentheorie. *Zeitschrift für Physik A: Hadrons and Nuclei*, 13:117–165, 1923.

[50] L. de Broglie. *Recherches sur la théorie des quanta*. PhD thesis, Sorbonne University, 1924.

[51] M. Born and P. Jordan. Zur quantenmechanik. *Zeitschrift für Physik A: Hadrons and Nuclei*, 34:858–888, 1925.

[52] P. A. M. Dirac. The fundamental equations of quantum mechanics. *Proc. R. Soc. Lond. A*, 109:642–653, 1925.

[53] E. Schrödinger. Quantisierung als eigenwertproblem. *Annalen der Physik*, 385:437–490, 1926.

[54] Wolfgang Pauli. Über das wasserstoffspektrum vom standpunkt der neuen quantenmechanik. *Zeitschrift für Physik A: Hadrons and Nuclei*, 36:336–363, 1926.

[55] John A. Buck. *Fundamentals of Optical Fibers*. Wiley, 2004.

[56] Govind P. Agrawal. *Nonlinear Fiber Optics, third edition.* Academic Press, 2001.

[57] Luther Pfahler Eisenhart. Separable systems of stäckel. *Annals of Mathematics*, 35:284–305, 1934.

[58] Nail N. Akhmediev and Adrian Ankiewicz. *Solitons, Nonlinear Pulses and Beams.* Chapman & Hall, 1997.

[59] Lin Zhang, Qiang Lin, Yang Yue, Yan Yan, Raymond G. Beausoleil, and Alan E. Willner. Silicon waveguide with four zero-dispersion wavelengths and its application in on-chip octave-spanning supercontinuum generation. *Optics Express*, 20:1685–1690, 2012.

[60] L. G. Cohen, C. Lin, and W. G. French. Tailoring zero chromatic dispersion into the 1.5 - 1.6 μm low-loss spectral region of single-mode fibers. *Elecron. Lett.*, 15:334–335, 1979.

[61] C. T. Chang. Minimum dispersion at 1.55 μm for single-mode step-index fibres. *Elecron. Lett.*, 15:765–767, 1979.

[62] C. T. Chang. Minimum dispersion in a single-mode step-index optical fiber. *Applied Optics*, 18:2516–1522, 1979.

[63] Bahaa E. A. Saleh and Malvin C. Teich. *Fundamentals of Photonics.* Wiley, 2007.

[64] I. P. Kaminow. Polarization in optical fibers. *IEEE J. Quantum Electron.*, QE-17:15–22, 1981.

[65] G. J. Foschini and C. D. Poole. Statistical theory of polarization dispersion in single mode fibers. *Journal of Lightwave Technology*, 9:1439–1456, 1991.

[66] C. R. Menyuk. Application of multiple length-scale methods to the study of optical fiber transmission. *Journal of Engineering Mathematics*, 36:113–136, 1999.

[67] N. Kalyanasundaram and P. Muthuchidambaranathan. Nonlinear pulse propagation in a weakly birefringent optical fiberber part 1: Derivation of coupled nonlinear schrodinger equations (cnlse). *Progress In Electromagnetics Research B*, 19:205–231, 2010.

[68] E. Lichtman. Performance limitations imposed on all-optical ultralong lightwave systems at the zero-dispersion wavelength. *Journal of Lightwave Technology*, 13:898–905, 1995.

[69] M. González-Herráez, S. Martín-López, P. Corredera, M.L. Hernanz, and P.R. Horche. Supercontinuum generation using a continuous-wave raman fiber laser. *Opt. Commun.*, 226:323–328, 2003.

[70] V. Ramaswamy and W. G. French. Influence of noncircular core on the polarisation performance of single mode fibres. *Electron. Lett.*, 14:143–144, 1978.

[71] S. C. Rashleigh. Origins and control of polarization effects in single-mode fibers. *Journal of Li*, 1:312–331, 1983.

[72] M. Lehtonen, G. Genty, H. Ludvigsen, and M. Kaivola. Supercontinuum generation in a highly birefringent microstructured fiber. *Appl. Phys. Lett.*, 82:2197–2199, 2003.

[73] Antoine Proulx, Jean-Michel Ménard, Nicolas Hô, Jacques M. Laniel, and Réal Vallée. Intensity and polarization dependences of the supercontinuum generation in birefringent and highly nonlinear microstructured fibers. *Optics Express*, 11:3338–3345, 2003.

[74] Joel A. Greenberg and Daniel J. Gauthier. High-order optical nonlinearity at low light levels. *Europhysics Letters*, 98, 2012.

[75] R. W. Terhune, P. D. Maker, and C. M. Savage. Optical harmonic generation in calcite. *Physical Review Letters*, 8:404–406, 1962.

[76] Anatoly Efimov, Antoinette Taylor, Fiorenzo Omenetto, Jonathan Knight, William Wadsworth, and Philip Russell. Phase-matched third harmonic generation in microstructured fibers. *Optics Express*, 11:2567–2576, 2003.

[77] K. J. Blow and D. Wood. Theoretical description of transient stimulated raman scattering in optical fibers. *IEEE J. Quantum Electron.*, 25:2665–2673, 1989.

[78] David Milam. Review and assessment of measured values of the nonlinear refractive-index coefficient of fused silica. *Applied Optics*, 37:546–550, 1998.

[79] C. V. Shank, R. L. Fork, R. Yen, R. H. Stolen, and W. J. Tomlinson. Compression of femtosecond optical pulses. *Appl. Phys. Lett.*, 40:761–763, 1982.

[80] W. H. Knox, R. L. Fork, M. C. Downer, R. H. Stolen, C. V. Shank, , and J. A. Valdmanis. Optical pulse compression to 8 fs at a 5-khz repetition rate. *Appl. Phys. Lett.*, 46:1120–1121, 1985.

[81] Akheelesh K. Abeeluck and Clifford Headley. Continuous-wave pumping in the anomalous- and normal-dispersion regimes of nonlinear fibers for supercontinuum generation. *Optics Letters*, 30:61–63, 2005.

[82] Ben Howard Chapman, Sergei V. Popov, and Roy Taylor. Continuous wave supercontinuum generation through pumping in the normal dispersion region for spectral flatness. *IEEE Photonics Technology Letters*, 24:1325–1327, 2012.

[83] J. M. Dudley and J. R. Taylor. *Supercontinuum Generation in Optical Fibers.* Cambridge University Press, 2010.

[84] J. Hansryd, P.A. Andrekson, M. Westlund, L. Jie, and P. Hedekvist. Fiber-based optical parametric amplifiers and their applications. *IEEE Sel. Topics Quantum Electron.*, 8:506–520, 2002.

[85] F. Forghieri, R. W. Tkach, and A. R. Chraplyvy. *Optical Fiber Telecommunications, Vol 3A.* Academic Press, 1997.

[86] C. V. Raman. A new radiation. *Indian J. Phys.*, 2:387–398, 1928.

[87] Fredrik Jonsson. *Lecture Notes on Nonlinear Optics.* Royal Institute of Technology, 2003.

[88] R. W. Hellwarth. Theory of stimulated raman scattering. *Phys. Rev. Lett.*, 130:1850–1852, 1963.

[89] R. H. Stolen, J. P. Gordon, W. J. Tomlinson, and H. A. Haus. Raman response function of silica-core fibers. *JOSA B*, 6:1159–1166, 1989.

[90] V. E. Zakharov and A. B. Shabat. Exact theory of two-dimensional self-focusing and one-dimensional self-modulation of waves in nonlinear media. *Soviet Physics JETP*, 34:62–69, 1972.

[91] Ryogo Hirota and Junkichi Satsuma. A variety of nonlinear network equations generated from the bäcklund transformation for the toda lattice. *Progress of Theoretical Physics Supplements*, 59:64–100, 1976.

[92] John Weiss, M. Tabor, and George Carnevale. The painlevé property for partial differential equations. *J. Math. Phys.*, 24:522–526, 1983.

[93] W. Malfliet. Solitary wave solutions of nonlinear wave equations. *American Journal of Physics*, 60:650–654, 1992.

[94] Zhenya Yan. Generalized method and its application in the higher-order nonlinear schrodinger equation in nonlinear optical fibres. *Chaos, Solitons & Fractals*, 16:759–766, 2003.

[95] John Scott Russell. Report on waves. Report of the 14th Meeting of the British Association for Advancement of Science, York, September, 1844.

[96] J. M. Dudley, G. Genty, F. Dias, B. Kibler, and N. Akhmediev. Modulation instability, akhmediev breathers and continuous wave supercontinuum generation. *Optics Express*, 17:21497–21508, 2009.

[97] B. Kibler, J. Fatome, C. Finot, G. Millot, F. Dias, G. Genty, N. Akhmediev, and J. M. Dudley. The peregrine soliton in nonlinear fibre optics. *Nature Physics*, 6:790–795, 2010.

[98] B. Kibler, J. Fatome, C. Finot, G. Millot, G. Genty, B. Wetzel, N. Akhmediev, F. Dias, and J. M. Dudley. Observation of kuznetsov-ma soliton dynamics in optical fibre. *Scientific Reports*, 2:463, 2012.

[99] G. H. Weiss and A. A. Maradudin. The baker-hausdorff formula and a problem in crystal physics. *J. Math. Phys.*, 3:771–777, 1962.

[100] W. J. Jones and B. P. Stoicheff. Inverse raman spectra: Induced absorption at optical frequencies. *Physical Review Letters*, 13:657–659, 1964.

[101] M. N. Islam, C. D. Poole, and J. P. Gordon. Soliton trapping in birefringent optical fibers. *Optics Letters*, 14:1011–1013, 1989.

[102] D. V. Skryabin and A. V. Yulin. Theory of generation of new frequencies by mixing of solitons and dispersive waves in optical fibers. *Phys. Rev. E*, 72:016619, 2005.

[103] A.V. Gorbach, D.V. Skryabin, J.M. Stone, and J.C. Knight. Four-wave mixing of solitons with radiation and quasi-nondispersive wave packets at the short-wavelength edge of a supercontinuum. *Optics Express*, 14:9854–9863, 2006.

[104] Andrey V. Gorbach and Dmitry V. Skryabin. Theory of radiation trapping by the accelerating solitons in optical fibers. *Phys. Rev. A*, 76:053803, 2007.

[105] J. C. Travers and J. R. Taylor. Soliton trapping of dispersive waves in tapered optical fibers. *Optics Letters*, 34:115–117, 2009.

[106] Goëry Genty, Minna Surakka, and Ari T. Friberg. Second-order coherence of supercontinuum light. *Optics Letters*, 35:3057–3059, 2010.

[107] Rick Trebino, Kenneth W. DeLong, David N. Fittinghoff, John N. Sweetser, Marco A. Krumbügel, and Bruce A. Richman. Measuring ultrashort laser pulses in the time-frequency domain using frequency-resolved optical gating. *Rev. Sci. Instrum.*, 68:3277–3295, 1997.

[108] Emil Wolf. *Introduction to the Theory of Coherence and Polarization of Light.* Cambridge University Press, 2007.

[109] Leonard Mandel and Emil Wolf. *Optical Coherence and Quantum Optics.* Cambridge University Press, 1995.

[110] Jeffrey B. Burl. *Linear Optimal Control.* Pearson, 1999.

[111] Orazio Svelto. *Principles of Lasers, fourth edition.* Springer, 1998.

[112] A. Antikainen, M. Erkintalo, G. Genty, and J. M. Dudley. On the phase-dependent manifestation of optical rogue waves. *Nonlinearity*, 25:R73–R83, 2012.